ABSTRACT

A Measurement of Charged Particle Ratios at High Transverse Momentum in an Ultra-Relativistic Heavy Ion Collision

Matthew Allen Horsley
Yale University
December 2002

Ultra-relativistic heavy ion collisions taking place at RHIC are thought to create conditions favorable for the creation of a quark gluon plasma (QGP). It is the main goal of the Relativistic Heavy Ion Collider (RHIC) to create and provide a definitive characterization of the quark-gluon plasma believed to be created in high energy heavy ion collisions. A determination of the initial conditions leading to the formation of a QGP is an important part of understanding its properties. Information about the evolution of the system formed during a heavy ion collision can be obtained by investigating charged particle ratios. The charged pion and kaon particle ratios as well as the anti-proton-to-proton ratio have been measured at high transverse momentum using a RICH detector. Comparisons have been made to previous measurements made with smaller collision systems and are found to be consistent with expectations derived from these smaller systems. The transverse momentum dependence of the charged particle ratios is consistent with being constant over the range measured, $0.75 < p_{\perp}[\mathrm{GeV/c}] < 2.5$ and can be described within a thermodynamical model of the collision and is an indication that chemical equilibrium was achieved over the course of the collision.

A Measurement of Charged Particle Ratios at High Transverse Momentum in an Ultra-Relativistic Heavy Ion Collision

A Dissertation
Presented to the Faculty of the Graduate School
of
Yale University
in Candidacy for the Degree of
Doctor of Philosophy

By
Matthew Allen Horsley

Dissertation Directors: John Harris, Gerd Kunde

December 2002

Acknowledgements

I would like to thank my wife, Gabel, for her support and encouragement over the course of my research, for without her this work would not have been possible. Likewise I owe a debt of gratitude to my family, as their support has been constant and unflagging for the time spent here at Yale. My advisor John Harris and co-advisor Gerd Kunde have played principle roles in my growth and development during my research at Yale and I would like to express my deep felt gratitude to both of them. A number of people have contributed to the RICH detector and without their efforts none of this would have been possible. Along with Gerd, I would like to recognize and thank Nikolai Smirnov, Brian Lasiuk and Jamie Dunlop. Lastly, I would like to thank Betty, Manuel, Helen, Jon, Christina, Mike, and Sevil. The time spent with them here at Yale was great!

Contents

List of Figures

Chapter 1

Introduction

The goal of particle physics, and by extension nuclear physics, is to understand the nature of matter. Historically, this has been pursued using particle accelerators of ever higher energies. To study matter at the smallest size scales requires machines capable of accelerating particles to exceptionally high energies. This has led to great advances in particle physics and thus to our current understanding of hadronic matter and its theoretical description using Quantum Chromodynamics (QCD). However, these past experiments have explored QCD at smaller and smaller distance scales which were typically much smaller than the dimensions of a proton. As pointed out in reference [11], to study the properties of strongly interacting matter over large distance scales it is necessary to move in the opposite direction by distributing large amounts of energy over a much larger volume than had been done previously. It was speculated in [11] that this could lead to the creation of a highly excited state of the QCD vacuum, where the symmetry properties of QCD may be altered and thus studied. Since then, the theoretical understanding of QCD matter under extreme conditions (density and/or temperature) has progressed to a point where definite predictions can be made, due in large part to statistical QCD calculations performed numerically on a computer (see [12] and references cited therein). These calculations, (Lattice QCD), indicate QCD matter, when placed under extreme conditions, is expected to undergo a phase transition from a state where the quarks and gluons are confined, into a state where they are de-confined. This new state of matter is called the Quark-Gluon Plasma

(QGP) and has been the subject of intense theoretical and experimental efforts for many years (and will remain so for many more). Nuclear matter is expected to undergo this change in phase under a range of different temperatures and densities as depicted in Figure 1.1. The vertical axis is a measure of the temperature and the horizontal axis is labelled as baryochemical potential, which is a measure of the net-baryon density of the system. The early universe is thought to have gone through just such a phase transition at high temperatures and low densities. A QGP is likewise expected to form in relatively cool matter having a sufficient density, such as that thought to exist in the interior of some neutron stars (see [13] for a recent treatment of this).

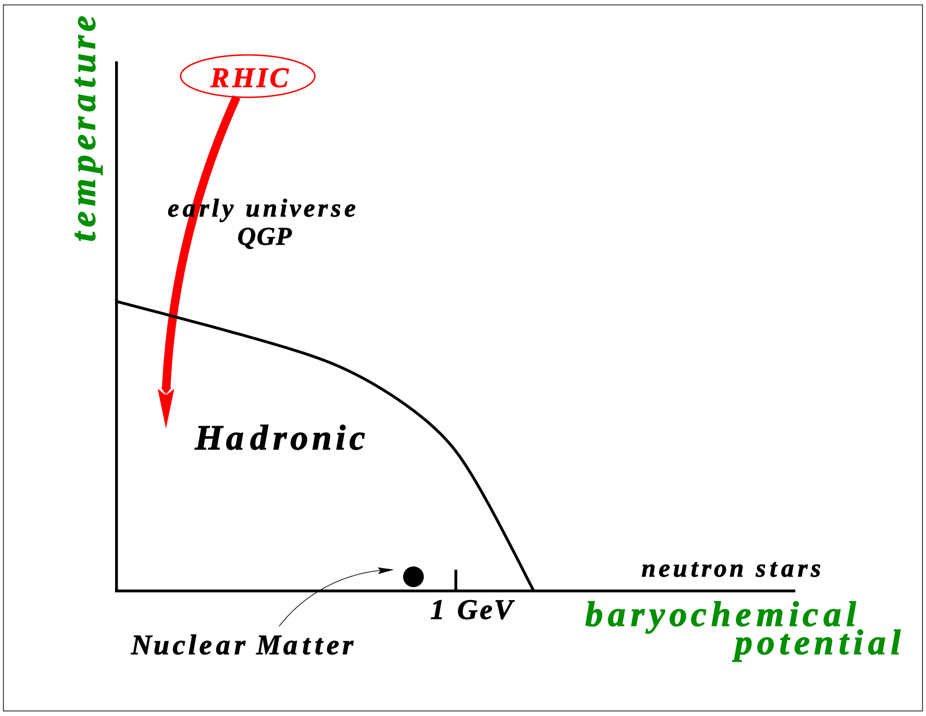

Figure 1.1: QCD Phase diagram. Boundary separating hadronic matter from deconfined matter is indicated by curved line in diagram.

To map out and study the QCD phase transition, an experimental program needs to be established to create the conditions favorable for such a phase transition. Achieving these conditions in the laboratory was suggested in [11] by arranging for heavy ions to collide at relativistic energies. Experimental efforts to map out the QCD phase boundary using this strategy have been attempted in the past at the Alternating Gradient Synchrotron (AGS) at Brookhaven National Laboratory (BNL) and at the Super Proton Synchrotron (SPS) located at CERN. To facilitate comparisons of experimental results conducted with different nuclear species colliding with varying amounts of energy, it is customary to report results at center of mass energies calculated per nucleon pair, $\sqrt{s_{NN}}$. The AGS (max. $\sqrt{s_{NN}} = 5$ GeV) and SPS (max. $\sqrt{s_{NN}} = 17.2$ GeV) physics programs generated a prolific amount of data and greatly added to what is known about nuclear collisions at relatively high energies. However, definitive statements about the QGP remain elusive. The center of mass energies achieved in the AGS and SPS fixed-target experiments remain in the regime where particle production is predominately non-perturbative, necessitating the use of phenomenological models to describe the nuclear collisions. By colliding heavy ions at even higher energies, $\sqrt{s_{NN}} \gtrsim 100$ GeV, particle production describable using (semi)-perturbative calculations becomes important[14, 15, 16, 17], leading to a more reliable calculation of the energy deposited in the center of mass region. The Relativistic Heavy Ion Collider (RHIC [18]) is the first heavy ion collider and is capable of accelerating different combinations of nuclear ion species from protons to gold over a continuous range of energies up to a maximum $\sqrt{s_{NN}} = 200$ GeV for gold on gold collisions. In the summer of 2000, RHIC achieved the first ever heavy ion collisions at $\sqrt{s_{NN}} = 130$ GeV, a milestone for heavy ion physics.

Many experimental signatures (see [19] and references cited therein) for the QGP have been proposed in the past, and many excellent reviews[20] of the field at various stages of its development exist in the literature and do not bear repeating here. The work presented in this thesis will cover the charged particle ratios $(\frac{\pi^-}{\pi^+}, \frac{K^-}{K^+}, \text{and} \frac{\bar{\text{P}}}{\text{P}})$ identified using a Ring Imaging Cherenkov (RICH) detector and measured at high transverse momentum, $0.75 < p_{\perp}[\text{GeV/c}] < 2.5$. Physics motivations for studying charged particle ratio's cover a number of pertinent topics in the field of heavy ion physics. The yields of charged particles relative to one another can provide valuable insight to the initial environment for particle production. In past experiments, theoretical descriptions of the particle production in terms of QCD thermodynamics was shown to be possible using only a few parameters, i.e.temperature, mass, and chemical potential. The charged Kaon and Antiproton-to-Proton ratios are sensitive to the net baryon density produced in a heavy ion collision and help determine, in part, the baryon chemical potential which influences the evolution of the system formed in the heavy ion collision. The creation of (anti-)baryons in the center of mass system of a heavy ion collision is not a well understood process, and is generally described in terms of pair production processes together with mechanisms responsible for transporting the baryon number from the beam rapidity to the center of mass rapidity. A particle's rapidity, $y = \tanh^{-1}(v_L) = \frac{1}{2}\ln\frac{E+P_L}{E-P_L}$, is a kinematic variable commonly used in particle physics relating the fraction of the particle's momentum parallel to the incident momentum vector, P_L, to it's energy, E, and in the non-relativistic limit is an approximation of the particle's longitudinal velocity, v_L. The beam particles are typically travelling with very large longitudinal velocities (and hence large rapidities), and the processes responsible for transporting protons from the beam rapidity to the center of mass rapidity are only poorly understood at present. The Antiproton-to-Proton ratio is sensitive to the combination of pair production processes and baryon number transport and is an aid in distinguishing between the various theoretical models describing baryon production at mid-rapidity.

Investigations into the transverse momentum ($p_\perp$) dependence of the charged particle ratios provide insight into the underlying mechanisms responsible for the particle production in the highly relativistic nuclear collisions at RHIC. Expectations from thermodynamic QCD for the charged particle ratios predict no dependence on the transverse momentum. This behavior can be compared to what is expected from perturbative QCD, where a deviation from this constant value is expected for sufficiently high values of $p_\perp \gtrsim 4 - 5\text{GeV/c}$. Perturbative QCD provides an accurate description of the high $p_\perp$ particle production in hadron collisions at the $\sqrt{s_{NN}}$ achievable at RHIC and is expected to apply to the particle production in heavy ion collisions at the same center of mass energy. Particle production at low $p_\perp$ is not well understood, and thus the interplay between perturbative and non-perturbative effects becomes an important question for study. For instance, the $p_\perp$ at which particle production can be said to be predominately perturbative is not clearly known and remains an open question. In addition, nuclear effects like partonic energy loss are expected to affect the perturbative spectra and play a major role in the search for the QGP. The $p_\perp$ dependence of the charged particle ratios contain information as to what happens subsequent to the initial particle production. It remains an open question whether scattering amongst the created hadrons plays a role in the evolution of the system formed in a heavy ion collision.

In the following chapters, details necessary to the analysis will be presented. Chapter 2 will introduce the experimental facilities used to produce and record the data created in the nuclear collisions. Techniques used to evaluate the data, including event reconstruction and analysis, will be given in chapters 3 and 4. Analysis results will be presented and discussed in chapter 5. Finally, conclusions will be drawn in chapter 6.

Chapter 2

Experimental Facilities

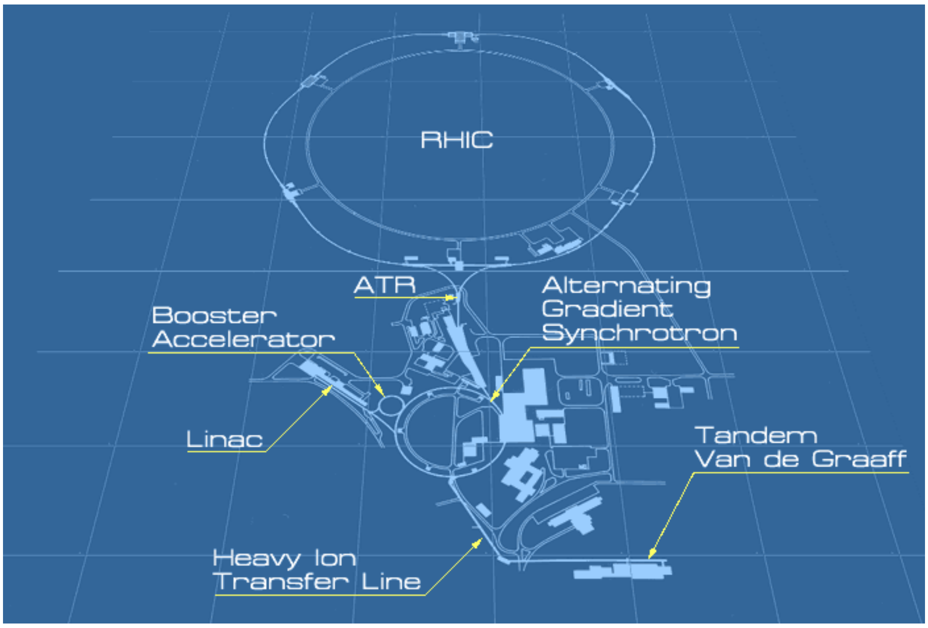

Figure 2.1: View of the RHIC collider complex. Facilities used in the formation and transportation of ions to the RHIC collider are shown as well.

The Relativistic Heavy Ion Collider[18] (RHIC) is the first heavy ion collider to be built and is located at Brookhaven National Laboratory. The collider is designed to accommodate a vigorous relativistic heavy ion scientific program. The capability of accelerating a wide range of nuclear species from hydrogen to gold up to center of mass energies greater than those achieved at any previous existing facility make RHIC ideal for studying heavy ion collisions over a wide range of conditions never before possible. The top attainable energies are $\sqrt{s} = 500\ GeV$ while operating in $p+p$ mode and $\sqrt{s_{NN}} = 200\ GeV$ for $Au + Au$ operations. Processes occurring with small cross sections σ_i are expected to play a significant role in the RHIC scientific program, and hence a large number of collisions $\mathrm{N_i}$ will be required for these types of measurements. To accommodate this need for a large event sample, the collider is designed to have a large luminosity L, which is a measure of the collider's ability to deliver a large interaction rate R, i.e. $R_i = L\sigma_i$. The luminosity L for a collider is defined as $L = fn\frac{N_1 N_2}{A}$ where N_1 and N_2 are the numbers of particles contained in a bunch, n is the number of bunches, A is the cross-sectional area of the overlap between the two colliding beams of particles, and f is the revolution frequency. The design luminosity operating in $Au + Au$ mode at top energy is, on average, $\sim$ 2 x 10^{26} $cm^{-2}sec^{-1}$ with possible future upgrades increasing this by an order of magnitude. The luminosity increases for lighter ion species and is expected to reach $\sim$ 10^{31} $cm^{-2}sec^{-1}$ for $p + p$ operations.

In the sections to follow, a description of the RHIC collider together with the experimental facilities used in the data taking for this thesis will be presented and discussed. Section 2.1 details the construction and operations of the RHIC collider, section 2.2 describes the trigger detector common to the RHIC experiments, while sections 2.3 and 2.4 describe the STAR experiment.

2.1 RHIC

A large infrastructure is needed to achieve this remarkable feat, including facilities to produce the ions, boosting the ions to suitable energies for insertion into the main RHIC rings, vacuum facilities, and cryogenic cooling. The site chosen for the construction of RHIC is Brookhaven National Laboratory (BNL) on Long Island, NY where much of the infrastructure was already in place prior to the construction of RHIC. For $Au + Au$ operations, Au ions are created using the Pulsed Sputter Ion Source in the Tandem Van de Graaff facility (see Figure 2.2). The Au ions are created with a $Q = -1$ charge, and then accelerated by a +15 MV potential. The Au ions are then sent through a stripping foil producing Au ions with net charge of $Q = +12$ at a kinetic energy of 1 MeV/nucleon. Upon exiting the tandem, the Au ions are further stripped by an additional stripping foil to a net charge of $Q = +32$. Before the ions can be sent to the Alternating Gradient Synchrotron (AGS) for eventual insertion into RHIC, the ion bunches enter a long ($\sim$ 550 m) heavy ion transfer line (HITL) and are delivered to the booster synchrotron. The booster accelerates the Au ions to energies of 95 MeV/nucleon and reduces the number of bunches by half while preserving the total number of ions. In the Booster-to-AGS (BtA) transfer line, the Au ions are sent through another foil, stripping the positively charged ions further to a net charge of +77, whereupon they are delivered to the AGS.

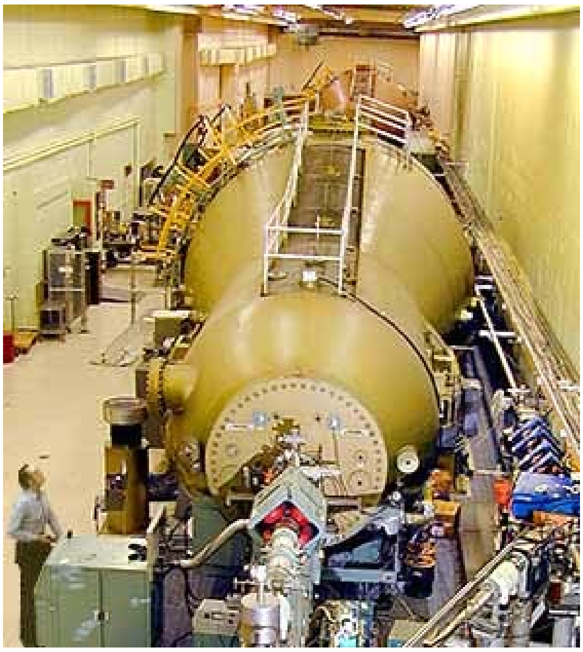

Figure 2.2: Tandem Van de Graaff at Brookhaven National Laboratory.

The insertion into the RHIC ring is accomplished via the AGS To RHIC (ATR) transfer line. The Au ions enter the transfer line and are stripped of their remaining electrons before delivery to RHIC with a final net charge of +79. The ions are injected into RHIC with the Fast Extracted Beam (FEB) system which is capable of performing multiple single-bunch extraction (MSBE) of the heavy ion beam. During the first year, the RHIC collider was operated with 56 bunches in each ring, reaching a peak luminosity of 3.3 10^{25} $cm^{-2}s^{-1}$ and an average luminosity of 1.7 10^{25} $cm^{-2}s^{-1}$[21].

2.2 ZDC

A common triggering scheme was devised for all four experiments at RHIC to facilitate an easy comparison of experimental results. Collisions involving heavy nuclei at RHIC energies typically result in the emission of evaporation neutrons at very small angles ($\sim$ 2 mrad) with respect to the beam. Detecting these neutrons travelling along the two beam directions in coincidence constitutes a minimum bias selection of the heavy ion collisions at RHIC. This is done by detecting their energy using two calorimeters[22], one on each side of the interaction point. The calorimeters are placed far downstream ($\sim$ 18 m) of the interaction point, are centered at 0° and subtend a small angle of 2.5 mrad, thus the name Zero Degree Calorimeter (ZDC).

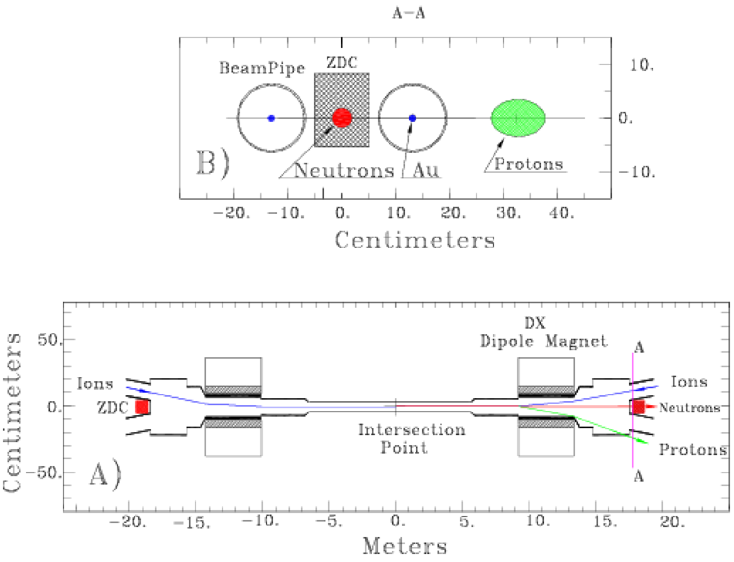

Figure 2.3: Plan view of the collision region and (section A-A) "beam's eye" view of the ZDC location indicating deflection of protons and charged fragments (with Z/A $\sim$ 1) downstream of the 'DX' Dipole magnet.

The ZDCs are seated behind the DX magnets which act to bend away from the ZDCs any charged fragments travelling along the beam direction as in Figure 2.2.

The RHIC ZDCs are hadronic calorimeters employing layers of tungsten absorbers together with Cherenkov fibers for sampling. The light generated in the fibers is sent to a set of three Photo-multiplier tubes (PMT) with the summed analog output of the PMT's used to generate the ZDC signal. The hadronic minimum bias trigger used by STAR requires a coincidence between the two ZDC's, with each ZDC signal having a summed analog PMT output corresponding to $\sim 40\%$ of a single neutron signal. The readout electronics used at each of the experiments are identical in design. The signal from each ZDC is split in two, with one signal being sent to the RHIC control room and the other is used as input for the experiment's trigger.

2.3 STAR

The main physics motivation behind the design of the Solenoidal Tracker At RHIC (STAR) is the search for and definitive characterization of the quark-gluon plasma believed to be created in high energy heavy ion collisions. An emphasis is placed on describing the collisions in the broadest sense possible, addressing both the soft and hard physics accessible in the collisions at RHIC.

In particular, the large track multiplicities in a heavy ion interaction at RHIC make possible measurements of global observables, (such as temperature, reaction plane, centrality) for every event, allowing investigations into correlations between different observables on an event-by-event basis. Also, at the high center of mass energies achieved at the RHIC collider, particle yields in the perturbatively calculable high transverse momentum region are high enough to allow such distributions to be used as probes of the initial state of the collision system through their interactions with the surrounding bulk matter created in the collision. In addition to measuring inclusive and event-by-event observables in heavy ion collisions, studying proton-proton (pp) and proton-nucleus (pA) collisions are a part of STAR's scientific program. These studies complement STAR's heavy ion program by providing measurements of parton distribution functions and will also serve as a reference for the heavy ion program. A polarized pp program was started in 2001 and will eventually provide measurements of the gluon's contribution to the nucleon spin.

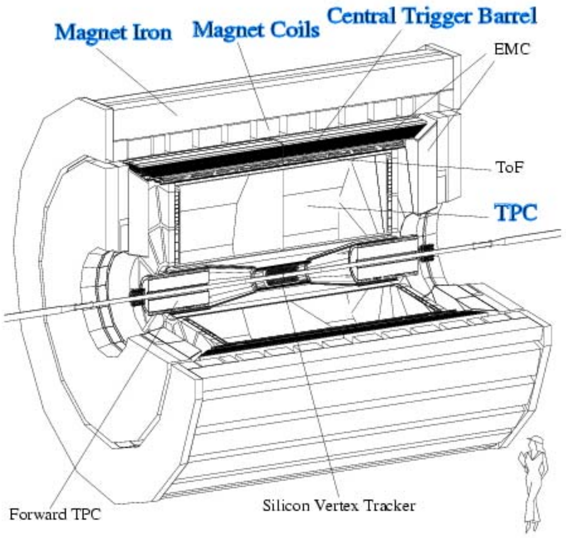

Figure 2.4: Cut-away view of the STAR detector. RICH detector subsystem not shown in this view (see Figure 2.19 for more detail).

To meet it's physics goals, the STAR detector was designed to be flexible enough to provide multiple measurements simultaneously under a number of different operating conditions at the high interaction rates at RHIC (10% of design luminosity $\sim 2 \times 10^{26}$ $\text{cm}^{-2}\text{s}^{-1}$ during the first year)[21]. The large number of charged particles produced at mid-rapidity in a heavy ion collision creates a great amount of data which has to be processed quickly to maximize STAR's data taking rate (~10 MBytes/s for first year). Tracking of these charged particles in such high multiplicity events must be robust and provide sufficient momentum resolution at high momentum.

To achieve these goals, the STAR experiment (Figure 2.4) was built around a Time Projection Chamber (TPC) having a large acceptance to accommodate event-by-event characterizations and maximize yields of hard probes. The TPC is situated inside a solenoidal magnet to provide momentum measurements and is surrounded by a barrel of scintillating slats (CTB). Hadronic calorimeters (ZDC) (see section

2.2) are placed downstream of the detector and are used to provide a minimum bias trigger. A Ring Imaging CHerenkov detector (STAR-RICH) is placed outside the TPC radius at mid-rapidity and is used to provide charged particle identification at high momentum. Additional detectors such as a Time of Flight patch (TOFp), Silicon Vertex Tracker (SVT), Forward TPC (FTPC), Beam-Beam Counter (BBC), and ElectroMagnetic Calorimeters (EMC) are included in the makeup of STAR in the second year of operations.

2.3.1 STAR Magnet

Momentum measurements are performed at STAR by measuring the helical trajectories executed by charged particles in the presence of a magnetic field. The STAR magnet [23] is cylindrical in design with a length of 6.85 m and has inner and outer diameters of 5.27 m and 7.32 m, respectively. The STAR magnet system in the final stages of completion is shown in Figures 2.5 and 2.6. Two pole tips placed on either end complete the design, and along with the rest of the magnet steel act as a return path for the field flux. The magnet generates a field along the length of the cylinder having a maximum of $|B_z| < 0.5\ T$. The field strength is determined by a number of competing concerns, including optimizing acceptance for low $p_\perp$ particles while

Figure 2.5: STAR Magnet.

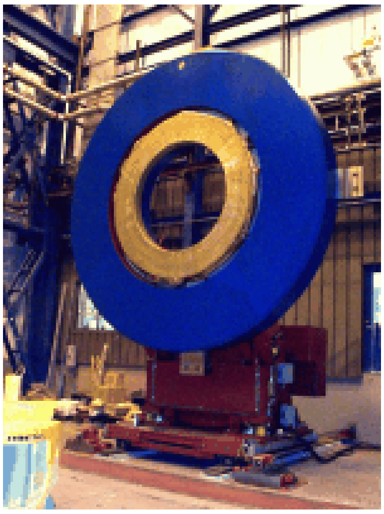

Figure 2.6: STAR Magnet Pole Tip.

maintaining adequate momentum resolution at high $p_\perp$, as well as practical issues such as cost. The measurement of the momentum of charged particles at STAR is accomplished by means of a tracking device (see subsection 2.3.2 for details) allowing the determination of the particle trajectories, (and hence their radius of curvatures or sagittas), in the magnetic field. Momentum resolution at high $p_\perp$ is dominated by the accuracy of the sagitta measurement. Inhomogeneities in the magnetic as well as electric field affect this measurement of the sagitta and thus provide an upper bound on the allowable field distortions [24, 25]. The drift velocity of electrons in STAR's tracking detector's gas volume can be obtained from the Langevin equation

$$\overrightarrow{v_D} = \frac{\mu}{1+(\omega\tau)^2}\left(\overrightarrow{E} + \omega\tau\frac{\overrightarrow{E}\times\overrightarrow{B}}{|\overrightarrow{B}|} + (\omega\tau)^2\frac{\overrightarrow{B}\left(\overrightarrow{E}\cdot\overrightarrow{B}\right)}{\overrightarrow{B}^2}\right), \tag{2.1}$$

where μ is the electron mobility, ω is the cyclotron frequency and τ is the mean drift time between two collisions in the gas. In the case of perfectly aligned $\overrightarrow{E}$ and $\overrightarrow{B}$ fields the drift velocity of electrons in the TPC gas will be simply $v_D = \mu\overrightarrow{E}$. Field imperfections will impart non-zero drift velocities to the electrons in directions not aligned to the main $\overrightarrow{E}$ field component and can lead to errors in the tracking. Measurements of the track curvature for high momentum tracks will be strongly influenced by any field imperfections which produce coordinate shifts in the azimuthal direction. Radial field distortions will result in drift velocities in the azimuthal direction

$$v_\phi = \frac{\mu E_z\omega\tau}{1+(\omega\tau)^2}\left(\frac{B_r}{B_z} - \frac{E_r}{E_z}\right). \tag{2.2}$$

The total azimuthal shift caused by these field distortions can be obtained by integrating over the time it takes the electrons to drift to the electronic readout located at the TPC's endcap,

$$\Delta x_\phi = \int v_\phi dt = \frac{1}{v_z}\int_z v_\phi dz = \frac{\omega\tau}{1+(\omega\tau)^2}\int_z\left(\frac{B_r}{B_z} - \frac{E_r}{E_z}\right)dz \tag{2.3}$$

with a similar expression existing for the radial shift caused by field distortions. The magnetic field homogeneity requirements can now be expressed in terms of the radial and azimuthal components of the magnetic field

$$
\begin{aligned}
|\Im_r| &= |\int_{z\prime=210\ \mathrm{cm}}^{z} \left(\frac{B_r}{B_z}\right) dz\prime| \\
|\Im_\phi| &= |\int_{z\prime=210\ \mathrm{cm}}^{z} \left(\frac{B_\phi}{B_z}\right) dz\prime|.
\end{aligned}
\tag{2.4}
$$

The maximum variation of the field integrals $|\Im_r|$ and $|\Im_\phi|$ within the tracking volume were found to be 0.3 cm and 0.035 cm for the radial and azimuthal components, respectively. These values for the field integrals are better than the design specifications by a factor of 2. The field was mapped and optimized using a field mapper from CERN. Field maps were produced for both polarities at full and half fields. The full field map had a mean $B_z = 4980$ gauss and ranged from 4950 to 5010 gauss.

2.3.2 Time Projection Chamber

In general, particle detectors having a long drift distance perpendicular to a readout plane, with the long dimension being the time of arrival, are called Time Projection Chambers and provide a full three dimensional reconstruction of a charged particle's trajectory. A Time Projection Chamber is the principle detector for the STAR experiment. A schematic diagram of the TPC is shown in Figure 2.7. To maximize the physics potential of the experiment, the TPC was designed to cover a large portion of phase space. The TPC is cylindrical in shape and measures 4.2 meters in length. The radius of the inner field cage is 0.5 meters which effectively introduces a lower cutoff of $p_\perp \sim$ 150 MeV/c for tracks accepted into the TPC's tracking volume ($\sim$ 75 MeV/c for 0.25 T). The outer radius of the TPC is 2 meters, allowing pathlengths ($\sim$ 1.5 m) large enough to achieve the desired momentum accuracy at high $p_\perp$. The phase space coverage offered by the TPC extends over the full azimuth and covers a pseudorapidity interval that ranges from $-2 < \eta < 2$ for the inner radius to $-1 < \eta < 1$ for the outer. Momentum reconstruction requires tracks having appreciable pathlengths which effectively limits the tracking to $-1.5 < \eta < 1.5$. A large diaphragm made of carbon coated Kapton (Central Membrane) having a thickness of 70 μm is stretched between the inner and outer field cages at the center of the TPC (z = 0 cm). The Central Membrane is maintained at a high voltage with respect

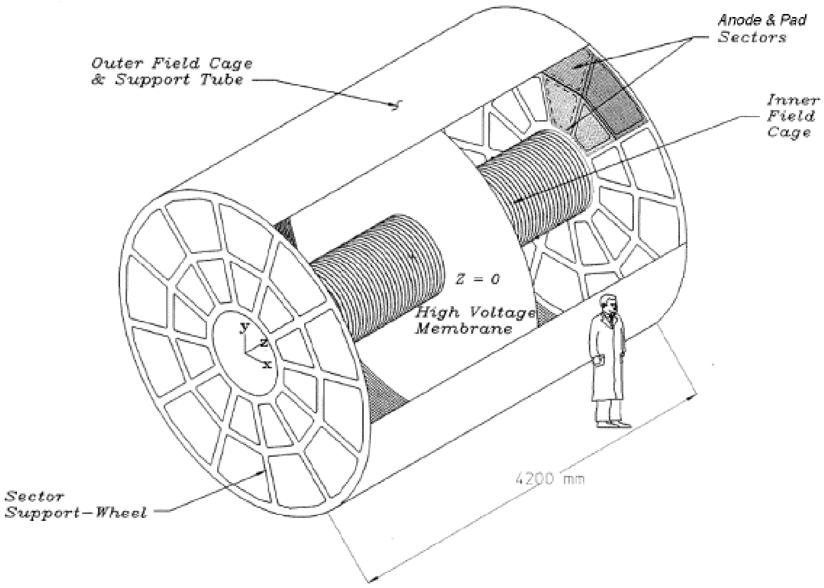

Figure 2.7: STAR TPC.

to a set of detection planes, with one detection plane located at either end of the TPC. Secondary electrons liberated along a charged particle's trajectory drift to the closest end of the TPC where their position in the detection plane is determined as a function of time. The mean drift time constitutes a measurement of the ionizations point of origin along the main axis of the TPC. Coupled with the two dimensional readout of the detection plane, a full three dimensional localization of the particle's trajectory can be obtained.

The STAR TPC volume is filled with P10 gas (Ar, 10% CH_4) at ~ 2 mbar above atmospheric pressure. Charged particle identification is possible over a limited range of momentum by measuring the energy loss (dE/dx) suffered by a particle as it travels through the gas volume of the detector. Particle identification of some short lived particles, such as the Λ particle, are possible via topological reconstruction of the decay products and an invariant mass method. Additional methods of particle identification exist using topological constraints (i.e. kink's) but are limited to particle species having mean lifetime's (τ) which allow a mean pathlength of approximately $c\tau \sim 1-1.5$ m, which limits their effectiveness. The TPC plays a large role in the data analysis of this thesis, which relies on the TPC to provide a set of tracks which point to the RICH detector on a track-by-track and event-by-event basis, as well as extracting various track parameters necessary for the RICH analysis, (momentum, extrapolated positions at the RICH). In what follows, a description of the TPC construction is given, with particular emphasis placed on details which may influence the RICH data analysis.

Field Cage Design

The trajectory of a charged particle is reconstructed by drifting the ionization electrons to a readout plane located at either end of the TPC. To drift the ionization electrons in the TPC gas volume requires that an electrical field be present. The electrical field is created using a set of field cages (see Figure 2.7). The field cage design consists of two concentric cylinders which define the active volume of the TPC. A nearly uniform electric field is created along the axis by a series of equipotential rings placed on the surfaces of the inner and outer field cages. Irregularities in the spacings of the rings or in the rings themselves will result in radial field components and consequently lead to a degradation in the momentum resolution. Field calculations [25] have shown electric field distortions to be well within the allowed limits set by momentum resolution considerations.

The design of the field cage is to be as low mass as possible so as to not impede the progress of the particles, while at the same time to be strong enough to maintain the detector's structural integrity. The field cages were built using two sheets of metal coated Kapton separated by a honeycomb of Nomex. The whole assembly was rolled into a tube and the sheets of Kapton were epoxied to the honeycomb. The Kapton in the outer field cage (OFC) (Figure 2.8) is laminated with a 35 micron layer of copper and the metal layer is etched into stripes which form the equipotential rings used to establish the electric field within the TPC gas volume. The inner field cage (IFC) (Figure 2.9) is similar to the outer field cage but the Kapton is laminated with a thinner layer of Aluminum (9 micron) and the Nomex layer is thicker (1.27 cm). The rings are spaced 1 cm apart and are biased by a chain of 2 $M\Omega$ resistors. The outer field cage (OFC) rests inside an aluminum gas containment vessel (Figure 2.10)

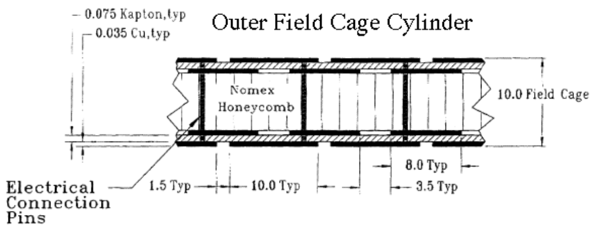

Figure 2.8: Outer field cage structure.

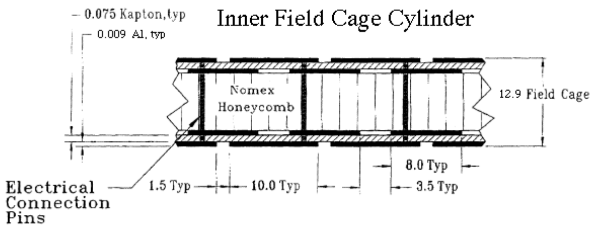

Figure 2.9: Inner field cage Structure.

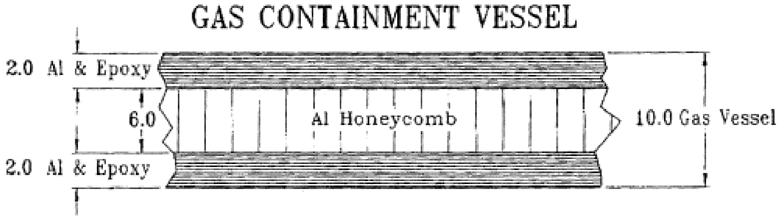

Figure 2.10: Aluminum gas containment vessel cross section. Dimensions in mm.

which is separated from the OFC by 5.7 cm of nitrogen gas.

The amount of material in the path of a charged particle can be expressed in terms of a radiation length. Table 2.1 contains the various materials used in the construction of the TPC. The IFC has a total radiation length of $\sim$ 0.62%. The OFC is constructed with slightly denser material and thus presents a greater amount of material for a particle to travel through, resulting in a total radiation length of approximately 2.43%. The TPC gas represents a radiation length of 1.17% for a particle travelling through the gas volume and is included in the total radiation length for the outer field cage. The amount of material increases dramatically in the gas containment vessel, reaching a radiation length of $\sim$ 12%. The total amount of TPC material in front of the RICH is then $\sim$ 15%. Particles travelling though this material will be deflected by small angle scattering. This will limit the precision with which extrapolations of TPC tracks to points outside of the TPC (e.g. the RICH, TOFp, or EMC) can be performed. The RMS angular deflection suffered by a particle can be expressed in terms of the particle's momentum p, velocity β, and charge number

Table 2.1: Material Used In TPC Construction

Structure	Material	Density ($\frac{g}{cm^3}$)	Rad. Length (%)
Insulating gas	N_2	0.001	0.10
TPC IFC	Al	2.7	0.04
TPC IFC	Kapton	1.420	0.05
TPC IFC	Nomex	0.064	0.20
TPC IFC	Adhesive	1.2	0.23
IFC Total (w/gas)			**0.62**
TPC gas	P10	1.56e-03	1.17
TPC OFC	Copper	8.96	0.91
TPC OFC	Kapton	1.420	0.05
TPC OFC	Nomex	0.064	0.15
TPC OFC	Adhesive	1.2	0.15
OFC Total (w/gas)			**2.43**
Insulating gas	N_2	0.001	0.02
Gas Vessel	Al	2.590	4.31
Gas Vessel	Honeycomb	0.037	0.09
Gas Vessel	Al Brackets	2.590	6.85
Gas Vessel	Adhesive	1.2	0.47
Gas Vessel Total			**11.74**
TPC Total			**14.79**

z as well as the material's radiation length X_0 and is shown in equation 2.5.

$$\theta_0 = \frac{13.6 \text{ MeV}}{\beta cp} z \sqrt{\frac{x}{X_0}} \left[1 + 0.038 \ln \frac{x}{X_0} \right] \tag{2.5}$$

Deviations from the particle's trajectory as it travels through the OFC and the gas containment vessel can be calculated using equation 2.5 and for a 2 GeV/c particle will be approximately $\theta_0 \sim 0.15°$, presenting no serious problem for particle identification in the RICH. Additional sources of material such as the Central Trigger Barrel (CTB) and the RICH itself approximately double the amount of material traversed by the charged particle and will be discussed in the sections describing the CTB and RICH. The uniform electric field established by the field cages lies along the TPC's main axis. The magnitude of the field is greatest at the central membrane which is biased at -31 kV and decreases in a steady manner to 0 V at the ground wires located on either end of the TPC. The secondary electrons produced along a charged particle's trajectory are drifted in the electric field over to the closest end of the TPC. Figure 2.11 shows a set of measurements of the TPC drift velocity conducted over a period of a month showing a small variation of ~ 0.6% in the drift velocity. The mean drift

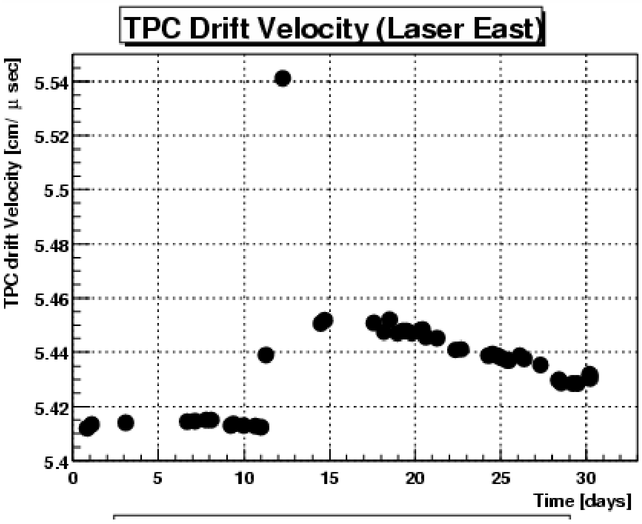

Figure 2.11: Electron drift velocity measured in East TPC for a period of 1 month.

velocity was calculated to be 5.44 ± 0.01 cm/μs. The error of 0.01 cm/μs represents the precision attainable from a technique using lasers which ionized gas atoms in the TPC volume. The drift velocity can be determined since the spacing of the lasers in the volume is known and it is possible to measure the time difference between the arrivals of the different laser layers. The RICH is placed directly outside the central membrane and thus the tracks intersecting the RICH are those having the longest drift times in the TPC and are therefore the most sensitive to any errors in the drift time (or field defects for that matter). The uncertainty in the drift velocity of 0.01 cm/μs represents an uncertainty of 0.38 cm in the position of the track's intersection point with the RICH. The implications of this are discussed in more detail in the analysis section describing the RICH residuals (section 4.2.3).

Multi-Wire Proportional Chamber

Located on either end of the TPC are a set of detection planes to measure the location and arrival times of the drift electrons liberated by a track ionization in the TPC gas. Each detection plane is instrumented with a thin multi-wire proportional chamber (MWPC) together with a pad chamber readout. On each detection plane there are twelve pad plane array's, (or super-sector's), arranged in a pin-wheel like fashion (Figure 2.12). Each super-sector is divided radially into 2 smaller sectors. The inner-most sector contains 1750 rectangular pads measuring 2.85mm by 11.5mm. Pads positioned near the center of a sector have the short dimension aligned in the radial direction and the long dimension perpendicular to this direction (see Figure 2.13). The outer sectors contain 3940 pads which measure 6.2mm by 19.5mm are are oriented in a similar fashion as the inner sector pads. A schematic diagram showing the inner and outer sectors for a single super-sector is shown in Figure 2.13. The outer sector has 32 pad rows occupying the entire outer sector in order to maximize the dE/dx measurements. The inner-most sector experiences the highest track density, and was therefore designed with a smaller pad size to provide a better space point resolution.

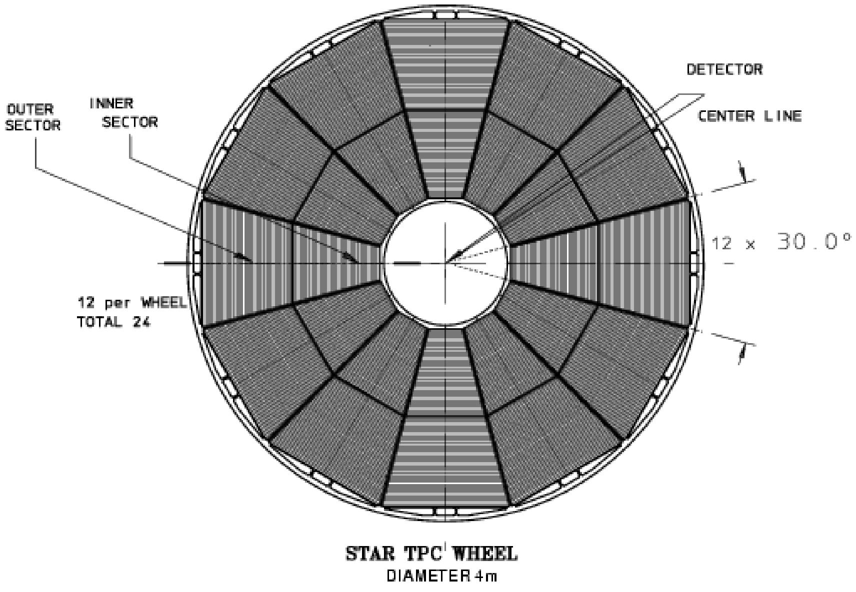

Figure 2.12: TPC sector layout.

To accommodate this smaller pad size, the number of pad rows used in the inner sector had to be reduced to 13 to ensure a reasonable amount of electronics used in the readout. Figure 2.14 shows the configuration of the MWPC defined by a set of wire planes and shows their relative position with respect to the pad plane arrays for the inner and outer sectors. The drifting electrons first have to pass through a gating grid which acts to separate the drift region of the TPC from the amplification region. The drift electrons are collected on the gating grid wires when the gate is closed, and are only allowed to pass through to the amplification region for events meeting the proper triggering conditions. The ground plane acts to define the effective volume of the MWPC. High tension anode wires are placed directly above each pad plane. Drift electrons are multiplied by avalanches near the anode wires. The motion of the ions created in this avalanche process induces a signal on readout pads directly below the anode wires.

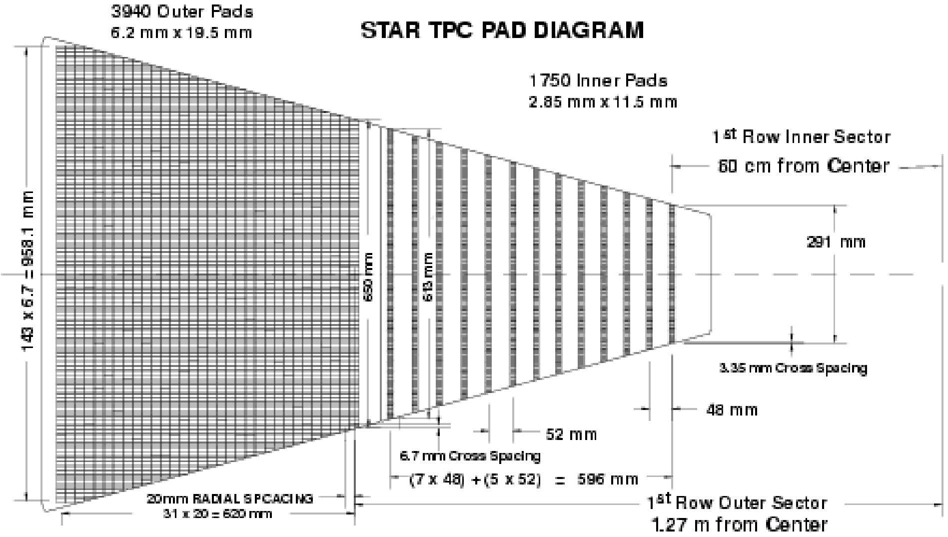

Figure 2.13: Detail of a single super-sector showing inner and outer sectors.

The electron cloud created by an ionizing particle will gradually diffuse in the longitudinal and transverse directions as it drifts towards the MWPC's located on either end of the TPC. The amount of diffusion in the P10 gas at half field was determined to be $\sigma_T \backsimeq 346\frac{\mu m}{\sqrt{cm}}$ in the transverse plane and $\sigma_L \backsimeq 356\frac{\mu m}{\sqrt{cm}}$ in the

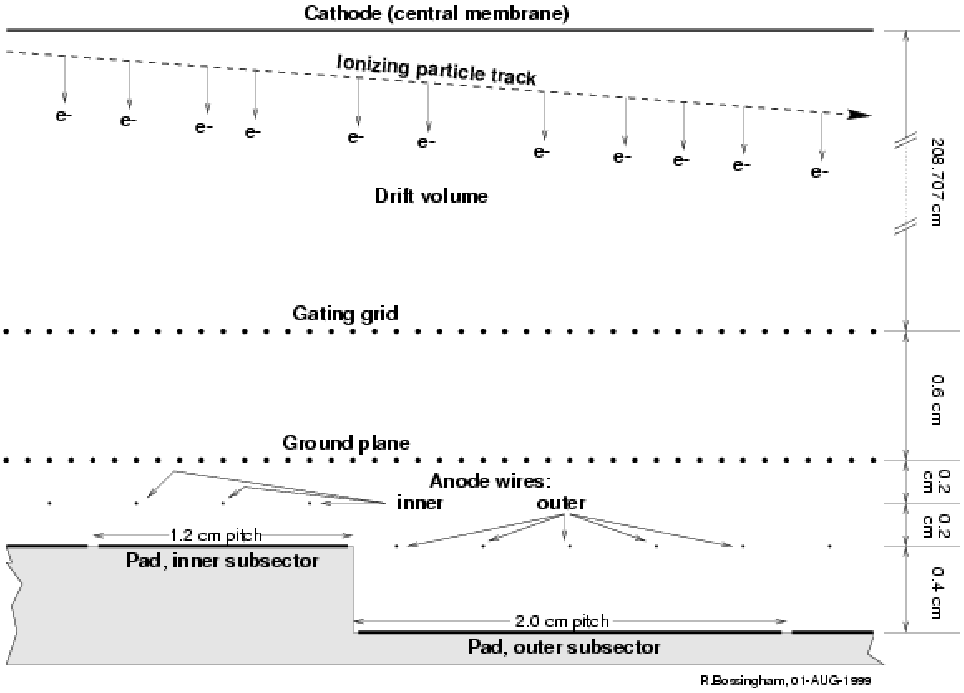

Figure 2.14: Depiction of a charged particle travelling through the TPC, leaving in its wake a trail of ionized gas molecules. The drift direction for the secondary electrons is shown, along with a close-up of the MWPC used to detect them.

longitudinal (time) direction. The track sample selected for the RICH data analysis consists of tracks lying near the center of the TPC and as such have the longest drift times. Drift times of this order, ($\sim$ 38 μs), correspond to widths of $\sim$ 5 mm in the transverse plane. To optimize the position resolution in the transverse plane, the pad size was chosen to maximize the likelihood of 3 pad hits. To achieve the desired accuracy in the longitudinal direction, a high sampling rate is needed to ensure enough measurements are taken to sufficiently describe the temporal extent of the charge cloud. A consideration of the longitudinal diffusion constant $\sigma_L \simeq 356\frac{\mu m}{\sqrt{cm}}$ yields an estimate for the charge cloud's longitudinal width of $\sim$ 0.5 cm, which extends $\sim \frac{0.5\ \mathrm{cm}}{v_{drift}} \simeq 100$ ns in time. This determines the sampling rate of 10 MHz.

The gas gain has to be high enough to ensure an adequate signal-to-noise ratio (20:1) for position resolution, while at the same time be small enough to be in the proportional region in order to maintain a reasonable dE/dx resolution. The gas gain used in the outer sector is $\sim$ 1100. The smaller pad size for the inner sector requires a larger gain ($\sim$ 3000) be used in order to ensure the same signal-to-noise ratio of 20:1. The dynamic range of the signal has to accommodate the amount of charge liberated by a highly ionizing particle travelling through the TPC's gas volume and was set at 10 bits. The signal induced on a pad is amplified and integrated by a circuit containing a pre-amplifier and shaper. The signal is sampled at the rate of 10 MHz as discussed above and is stored using a switched capacitor array (SCA). The event is digitized and transmitted over a set of optical fibers to the STAR Data Acquisition system (DAQ). The rate at which the data from central events was sent to tape was $\sim$ 1 Hz for the first year.

2.3.3 Central Trigger Barrel

The Central Trigger Barrel (CTB) is comprised of 240 slats of plastic scintillators arranged in a cylindrical fashion around the TPC. The CTB has a range of 2π in the azimuthal direction and has a total length of 4 meters. The slats are housed in aluminum trays, two slats per tray. Each slat has one radiator, one light guide, and one photomultiplier (PMT). The drawing (Figure 2.15) shows a segment with 2 slats. The slat closest to the center contains a scintillator that is 112.5cm x 21cm x 1cm. The other slat is 130cm x21cm x1cm. The coverage offered by a single slat is $\pi/30$ radians in the ϕ direction, and 0.5 in η. The signals generated by the slats are sent to digitizer boards, each one having 16 inputs. Within each digitizer, the signals are sent to a integrator and an 8-bit analog-to-digital converter (ADC), and then to a discriminator. The output of the discriminators can then be summed over the barrel and used as trigger. The average occupancy in the CTB for central AuAu interactions was 10 hits per slat. Extrapolating tracks to the CTB indicated a typical minimum ionizing particle striking the center of a slat gave a signal of 5 adc counts after calibration. There exists on each digitizer one external output for use by other detectors. The output from a single digitizer board can be obtained within 260 ns after the event, allowing a pre-trigger for fast detectors (like the RICH). The average radiation length of the CTB in front of the RICH is approximately 20%[26].

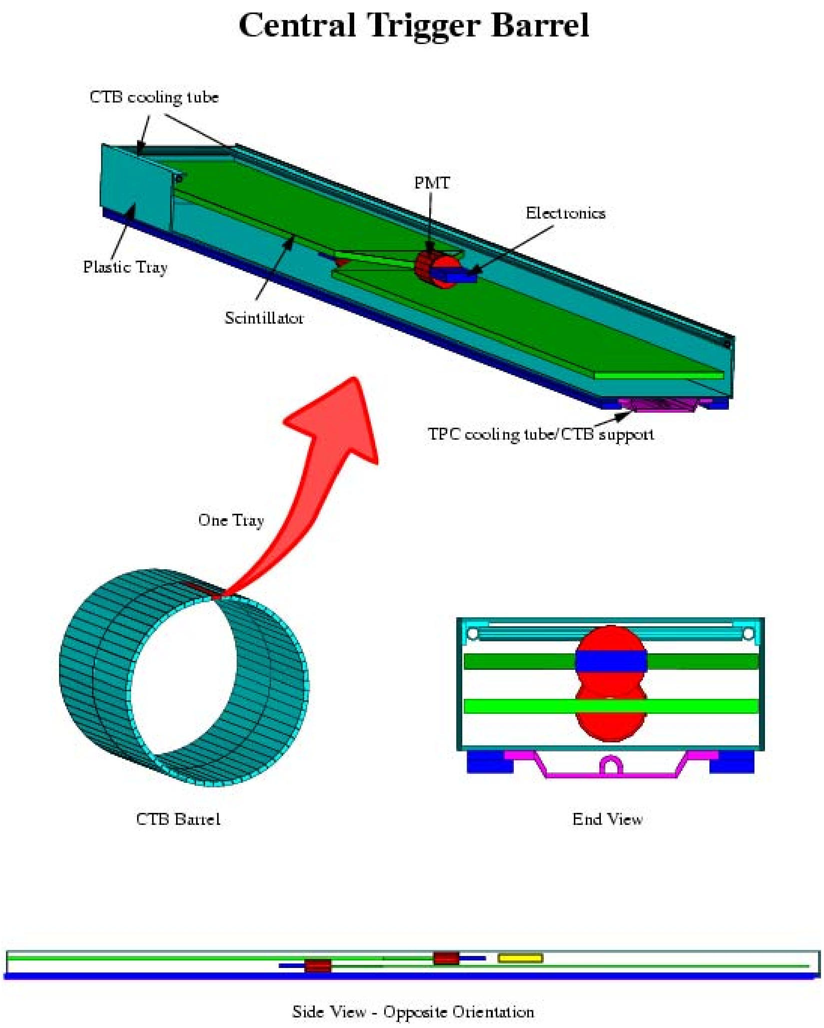

Figure 2.15: Central Trigger Barrel. The middle left figure shows the individual trays arranged in a cylinder. The top figure shows close-up of a single tray housing a pair of plastic scintillating slats. Middle right figure shows the cross section of a single tray seen from the end, while the lower figure shows the cross section from the side.

2.4 RICH

Particle identification (Pid) can be accomplished in a variety of ways, each having its advantages and drawbacks. Examples include calorimetry, time-of-flight, specific ionization, Cherenkov radiation, and others. Time-of-Flight, specific energy loss and Cherenkov radiation are sensitive to the particle's velocity, and when combined with a measurement of the particle momentum establishes the particle mass, and hence the particle species. This section details the construction and operating principles of the **R**ing **I**maging **CH**erenkov (RICH) detector used in the data analysis presented in this work. Originally built as a prototype[2] for the ALICE experiment, it was decided to include the RICH in the STAR experimental set-up (STAR-RICH) [27] for the purpose of providing particle identification at high $p_{\perp}$. There exist numerous and excellent references on RICH detectors in general [28, 29, 30, 31], and in particular for this detector prototype [2, 32, 33, 34, 35, 31, 36, 37, 38]. Therefore, only a brief description of the detector and the physical principles involved in its operation which are necessary for understanding the data analysis in this thesis will be discussed. In subsection 2.4.1 the physics principles involved with the operation of the detector will be introduced and discussed. Subsection 2.4.2 discusses the design of the detector, including the materials used in its construction. Included in this subsection, the detector placement in the STAR experimental setup and the detector performance will be discussed as well.

2.4.1 Operating Principles

When a charged particle is travelling in a medium with a velocity exceeding the speed of light in that medium, the particle will emit Cherenkov radiation. This effect was first discover by P. A. Cherenkov in 1934 while he was studying the effects of gamma rays on liquids and explained in 1937 by I. E. Tamm and I. M. Frank, eventually leading to the Nobel prize in 1958 for the three scientists. Cherenkov radiation is emitted by a charged particle whenever its velocity is greater than the phase velocity of light c/n (where c is the speed of light in vacuum and n is the index of refraction of the medium) in the medium traversed by the particle. The radiation is not emitted isotropically, but rather with a definite polar angle with respect to the particle's trajectory. The radiation is emitted uniformly in azimuth, and thus a cone of light is formed whose major axis lies along the particle's trajectory. Figure 2.16 is a depiction of a charged particle travelling with a velocity $\beta c > c/n$, showing the Cherenkov radiation emitted at an angle θ with respect to the particle's trajectory. From the diagram above, we can see that the opening angle of the Cherenkov light cone has the value

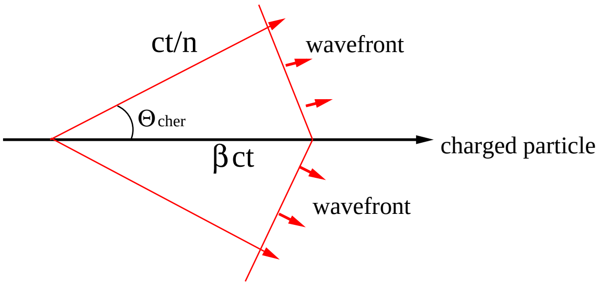

Figure 2.16: Cherenkov light cone.

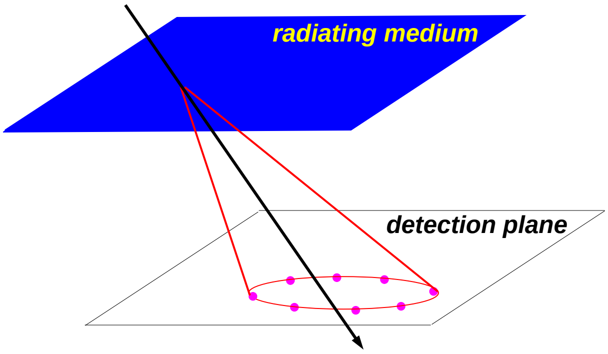

Figure 2.17: Projection of a Cherenkov light cone onto an imaging plane.

$$\cos\theta = ct/n\beta ct = \frac{1}{\beta n} \tag{2.6}$$

The radiation appears as a continuous spectrum. In a dispersive medium the index of refraction will have a dependence on the frequency of the radiation, and thus the Cherenkov emission angle θ will likewise be a function of frequency. The number of photons radiated per unit distance is given by expression 2.7

$$\frac{dN}{dx} = k(\lambda) \int \frac{1}{1 - n^2(\lambda)\beta^2} \frac{d\lambda}{\lambda} \tag{2.7}$$

where x is distance, n is the index of refraction, λ is the wavelength of the light, and k is a normalization factor taking into account various detector characteristics affecting the number of photons measured with the detector. The number of photons emitted per unit distance at a given wavelength is proportional to $\frac{1}{\lambda}$, and therefore the Cherenkov radiation spectrum peaks in the ultraviolet region, at small wavelengths. The importance of the Cherenkov effect as a scientific tool lies in the connection between particle speed and angle between momentum direction and radiation emission.

The projection of the Cherenkov light cone onto a plane (Figure 2.17) will produce a ring whose diameter is directly connected to the opening angle of the Cherenkov light cone. Thus, a measurement of the ring's diameter is equivalent to a measurement of the particle's velocity.

2.4.2 Detector Placement, Design and Construction

The RICH detector measures $146x99x24$ cm^3 (lxwxh). For safety reasons, the RICH detector is housed in a gas tight box having the slightly larger dimensions $180x120x30$ cm^3. The RICH detector together with the safety box has a mass of 200 kg. The detector is positioned in between the magnet coils and the CTB with the long dimension parallel with the beam line at a radial distance of $\sim$ 240 cm, straddling the Central Membrane (see Figure 2.18 for a picture taken of the RICH detector being inserted into the STAR experiment). The RICH detector is stationed at an angle of declination

Figure 2.18: Installation of the RICH detector into the STAR experimental set-up. The detector is shown housed in the aluminum safety box. A large frame is seen attached to the detector for the purposes of installation and is not present during data taking.

60° relative to the horizontal axis, (corresponding to the 5 'o clock position when facing the TPC), and subtends an azimuthal angle of approximately

$$\Delta\phi = \arctan\frac{\text{detector width}}{\text{radial distance}} \sim \arctan\frac{99}{240} \sim 22.4^\circ, \tag{2.8}$$

which is smaller than the angle subtended by a single TPC sector, 30°. Tracking of the charged particles intersecting the RICH detector is accomplished using two (5 and 19) of the TPC's 24 sectors, as shown in Figure 2.19.

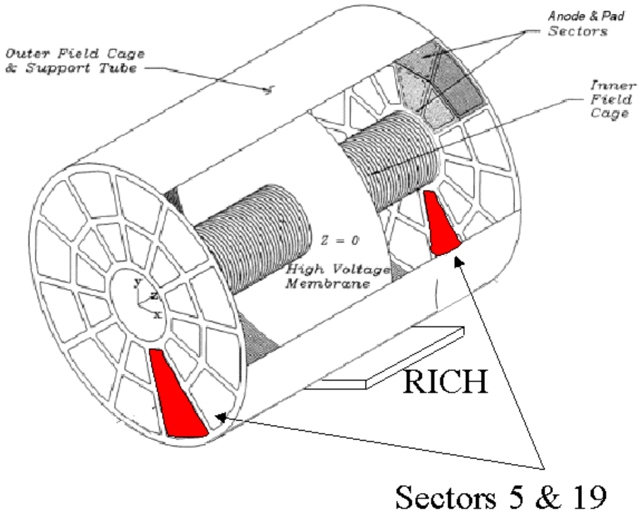

Figure 2.19: Placement of RICH detector relative to the STAR TPC (STAR magnet not shown in this figure). Charged particle tracking for tracks intersecting RICH is accomplished using TPC sectors 5 and 19.

The main components in the design of the RICH detector are shown in Figure 2.20. The RICH detector employs a liquid radiating medium for the generation of the Cherenkov radiation created by the passage of a charged particle above the velocity threshold. The liquid is housed in a 1 cm deep containment vessel. The entrance window is not required to be transparent to the UV Cherenkov light, and thus a strong and relatively inexpensive material such as neoceram can be used to provide structural strength to the containment vessel. The exit window not only has to be strong but UV transparent as well, and thus quartz was chosen for the exit window. The Cherenkov photons are converted into photo-electrons via a thin film photo-converter (CsI), which are then detected using a Multi-wire Proportional Chamber

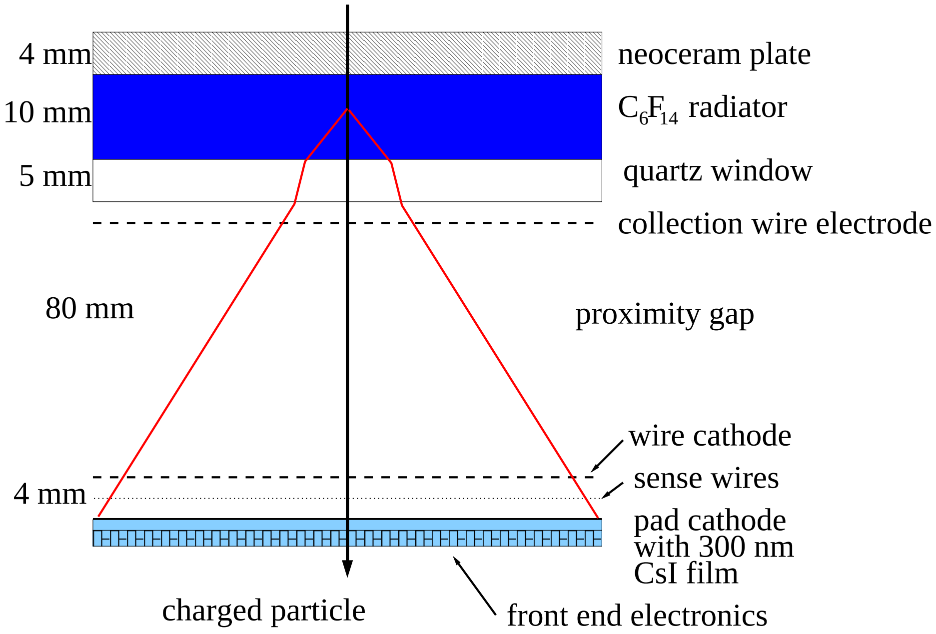

Figure 2.20: Schematic diagram of the RICH detector showing the main components of the RICH design.

(MWPC). To ensure an easily measurable ring diameter, the location points for the generation and localization of the Cherenkov light are separated by a distance of 80 mm to enlarge the ring diameter. This separation distance is referred to as a ”proximity gap”, and is filled with methane gas which is the operational gas used by the MWPC. A wire cathode plane is positioned just above the MWPC anode wires defining the effective volume of the MWPC, and acts to prevent electrons liberated in the proximity gap by ionizing particles from entering the MWPC volume. In the following subsections, the materials used in the construction and their impact on the analysis will be discussed in more detail, along with the operational characteristics of the MWPC and associated electronics.

Liquid Radiator and Quartz Exit Window

The radiating medium is a liquid, C_6F_{14}, and is housed in a 1 cm deep containment vessel. The depth of the radiator determines the amount of light generated as well as the width of the ring imaged onto the detection plane. In addition, the radiator depth has to be optimized to yield the best signal to noise ratio. A large depth will produce numerous photons spread out over a large area on the detection plane, leading to significant overlap between any two Cherenkov rings produced in a given event. A depth of 1 cm represents the optimal configuration for the detector. The quartz exit window is 5 mm thick and represents a compromise between maintaining the structural integrity of the radiator vessel and the desire to minimize the amount of detector material in between the particle and the detection plane. C_6F_{14} has an refractive index of $n = 1.29$ at a wavelength of $\lambda = 180$ nm. Using this mean value for the index of refraction, equation 2.6 then establishes the angle of emission for a charged particle travelling with a velocity $\beta \sim 1$, resulting in an angle $\theta \backsimeq 39°$. The mean index of refraction also determines the threshold velocity required for the emission of Cherenkov radiation, namely

$$\beta_{thres} = \frac{v_{thres}}{c} \geqslant \frac{1}{n} = \frac{1}{1.29} \sim 0.75. \tag{2.9}$$

Using the relationship between β and γ, the minimum particle energy necessary for emission can be calculated

$$E_{thres} = \gamma_{thres} mc^2. \tag{2.10}$$

Using the mean value of the refractive index together with eq. 2.9 gives

$$\gamma_{thres} = \frac{1}{\sqrt{1 - \beta^2_{thres}}} = \frac{n}{\sqrt{n^2 - 1}} \backsimeq 1.6 \tag{2.11}$$

and using the relation between energy and momentum $p = \frac{\beta}{c} E$ yields the momentum threshold for Cherenkov radiation

$$p_{thres} = 1.24mc. \tag{2.12}$$

The momentum thresholds for the various particles are thus

$$p_{thres} \sim \ 0.2, 0.7, 1.2 \text{ GeV/c for the } \pi, \text{K}, \text{and P particles respectively.} \tag{2.13}$$

The angle of emission depends on the particle's velocity and the index of refraction

$$\theta = \arccos \frac{1}{n(\nu)\beta} \tag{2.14}$$

through the relation expressed in equation 2.14, where ν corresponds to the frequency of the emitted light To facilitate the pattern recognition used in the particle identification, the liquid used as the generator of the Cherenkov radiation must have a small variation in the index of refraction for the different wavelengths of light the detector is sensitive to in order to minimize the spread in the angle of emission, (see eq. 2.14). Figure 2.21 shows the variation of the refractive index on wavelength for the liquid radiator, C_6F_{14}. Between 155 nm and 225 nm, the index of refraction varies $\sim$ 3%, which results in a maximum spread of $\sim$ 2% in the angle of emission. To maximize the amount of light reaching the pad plane, the absorption of the light in the radiator must be small. The transmission of light through a 1 cm deep cell was measured[1] with the results shown in Figure 2.22. The transmission is almost $\sim$ 100% for wavelength's $\lambda \gtrsim$ 180 nm.

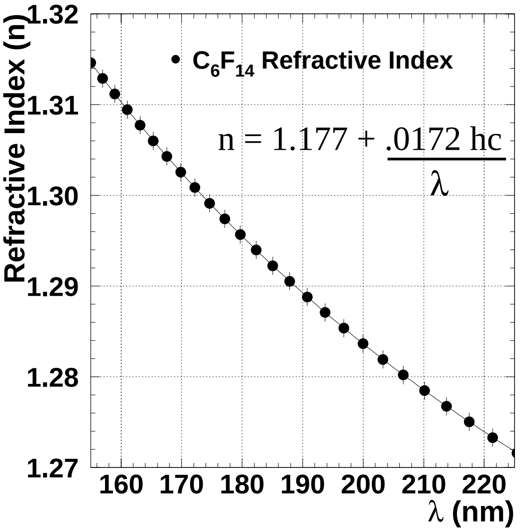

Figure 2.21: C6F14 index of refraction. Figure obtained from ref. [1].

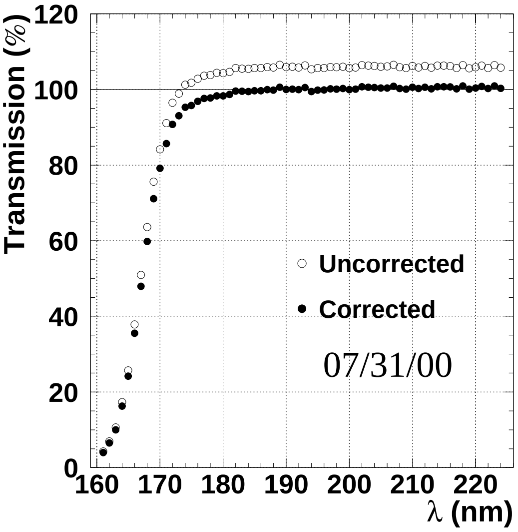

Figure 2.22: C_6F_{14} transmission. Figure obtained from ref. [1].

Figures 2.23 and 2.24 show the refractive index and transmission curves for quartz as a function of wavelength. The large values for the index of refraction has important implications for the propagation of the Cherenkov light cone to the detection plane. The transmission of the UV light through the quartz window is nearly 100% for wavelengths $\lambda \gtrsim 180$ nm. The index of refraction for quartz is larger than for the liquid radiator. This has implications for the propagation of the Cherenkov light cone through the detector materials. This can be shown using the simple example of a normally incident particle striking the RICH. For a particle travelling with a $\beta \sim 1$, the opening angle of the Cherenkov light cone will be determined entirely from the index of refraction of the liquid radiator and will be approximately 39 degrees. The angle made by the light cone in the quartz window can be obtained from a direct application of Snell's law. Because of the larger index of refraction of the quartz as compared to the liquid radiator, the light cone will bend inwards slightly, making a smaller angle of approximately 28 degrees relative to the normal. Upon exiting the quartz window, the Cherenkov light travels through the proximity gap which is filled with methane gas having an index of refraction $n_{meth} = 1.00$ independent of wavelength. Compared to the refractive index of quartz $n_{quartz} = 1.59$ at a wavelength $\lambda = 180$ nm, the methane's refractive index is small and due to Snell's law results in a large change in the angle ($\sim 55°$) made by the Cherenkov light at the quartz-methane boundary. The angles made at the various refractive boundaries by the Cherenkov light cone as it travels through the detector is shown as a function of β in Figure 2.25.

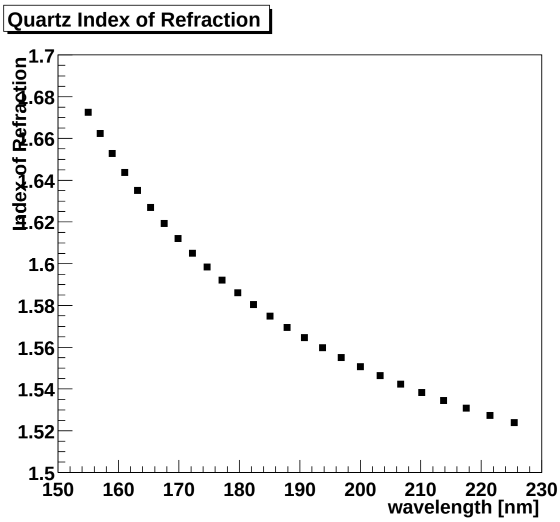

Figure 2.23: Quartz index of refraction.

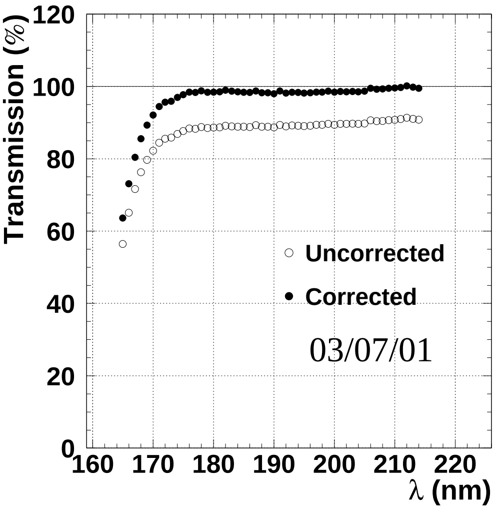

Figure 2.24: Quartz transmission. [1]

The curve marked "radiator" corresponds to the opening angle of the Cherenkov light cone in the radiator. The curve marked "quartz" corresponds to the angle made by a light ray lying on the Cherenkov cone at the boundary between the radiator and the quartz window. The curve marked "methane" corresponds to the angle made at the quartz-methane boundary.

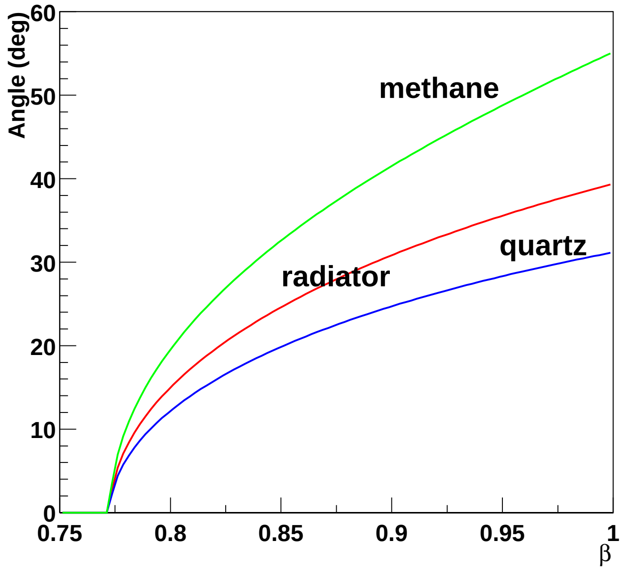

Figure 2.25: Angles made at refractive boundaries by the Cherenkov light cone emitted by a charged particle of normal incidence.

The Photodetector

The Cherenkov light is detected using a combination of a photo-converter coupled with a Multi-Wire Proportional Chamber (MWPC). A thin film (300 nm) of Cesium Iodine (CsI) acts as the photo-converter, converting a fraction of the incident Cherenkov photons into electrons. The efficiency with which the CsI converts photons into electrons is called its quantum efficiency and is shown as a function of wavelength in Figure 2.26. The efficiency is a maximum for the smaller wavelengths and is approximately 17% at λ=180 nm. CsI is a hygroscopic compound and will readily absorb moisture from its surroundings. Under exposure to water vapor in

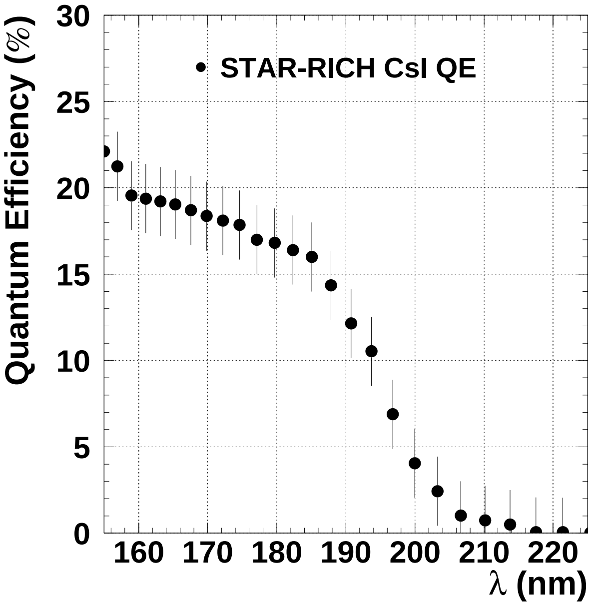

Figure 2.26: CsI quantum efficiency as a function of wavelength. Error bars correspond to an uncertainty of ±2% See Ref. [2] and references cited therein for details on determination of CsI quantum efficiency.

the atmosphere, various compounds form on the surface of the CsI film which act to seriously reduce the effectiveness of the CsI as a photo-converter. To maintain the quantum efficiency of the CsI film over the lifetime of the detector, it is necessary to ensure as little contact with moisture as possible. A gaseous circulation system was constructed to deliver a steady supply of methane gas during the normal operating state of the detector. During the course of the data acquisition for the first year, the water content of the methane gas was continuously monitored and found to be less than 2 ppm. In addition, the oxygen content of the methane gas was monitored and was found to be less than 6 ppm for the same time period. While short term exposure to oxygen was shown to have no serious consequences for the quantum efficiency, oxygen contamination for prolonged periods will result in a degradation of the quantum efficiency and thus lead to a reduction in the number of Cherenkov photons found which will have a negative impact on the data analysis.

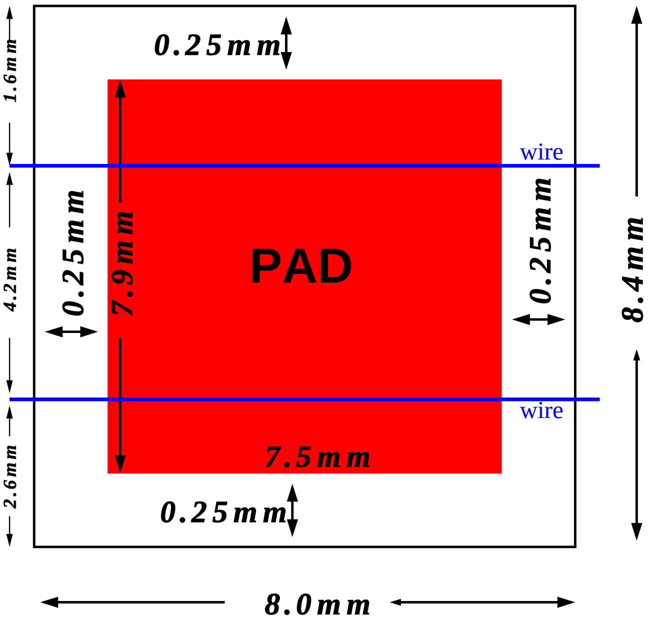

Figure 2.27: Closeup of a RICH pad segment showing dimensions of pad along with the location of the anode wires above the pad. [3]

The detection of the photo-electrons is done using a MWPC (Figure 2.20). The volume of the MWPC is defined by the wire cathode plane along with the pad plane which is coated with the CsI to accomplish the photo-conversion. The pad plane is segmented into 4 separate pad arrays, (or quadrants), each having the dimensions 64.0 x 39.2 cm^2. Figure 2.27 shows the dimensions of a single pad along with the location of the anode wires placed directly above the pad. The anode wires have a diameter of 20 μm and have a pitch of 4 mm. The anode wires are separated from the wire and plane cathodes by 2 mm. Pure methane is used as the operating gas for the MWPC, and is maintained at ambient temperature and pressure. The gas gain achieved under these operating conditions is $\sim 10^5$. The MWPC has to have a high efficiency for detecting and localizing single electrons emitted from the CsI. The efficiency for detecting a single electron with the MWPC was determined to be 95% (see [27] for discussion and references). Figure 2.28 shows the single electron pulse height distribution detected with a MWPC with a CsI coated cathode and having the same geometry as used in the prototype detector. Each pixel in the pad plane is readout individually via an analog readout (discussed in the next section), the analog signal is then digitally converted (adc), with a single adc unit corresponding to 0.17 fC. The anodes were held at a voltage of 2100 V relative to the cathodes and the gas used was pure CH_4. While in general a Polya distribution describes the single electron pulse height distribution, for the gas gain used in the chamber the single electron pulse height distribution is found to be purely exponential, obeying the Furry distribution (see [39] for discussion on single electron detection)

$$P(A) = \frac{1}{A_0} e^{-A/A_0}. \tag{2.15}$$

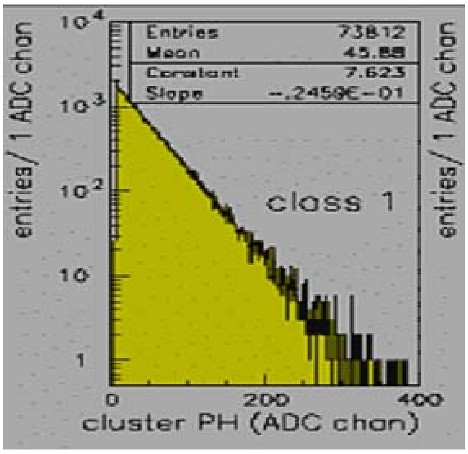

Figure 2.28: Exponential pulse height distribution for single electrons (class 1) detected with MWPC. Chamber gain can be calculated from the inverse slope obtained from fit (~ 40).

[Later, Figures 4.31 will show a similar exponential shape for each RICH quadrant using the data set collected during the first years running at $\sqrt{s_{NN}}$=130 GeV (see section 4.4.2 for details).] Tests conducted at CERN using 350 GeV/c π's impinging on the RICH at normal angles indicated that the number of Cherenkov photons detected using the RICH was on the order of 16 photons for particles in saturation. These tests were done with the anode voltage set to 2100 V. During the first year of operations, the anode wires were maintained at an operating voltage of 2000 V. This reduction in the operating voltage along with the lower air pressure at BNL as compared to CERN resulted in a reduction in the chamber gain, and hence a reduction in the number of photons detected for particles in saturation, ~ 10. This, however, had no serious consequences for particle identification.

Electronics and Data Acquisition

For each event, the RICH data was read out, packed and sent to the STAR data acquisition system. The RICH detector has 4 pad plane arrays each having 3840 pads for a total of 15360 pads read out each event. Due to the large number of channels a cost effective way of performing the analog signal processing was devised. This necessarily entailed a certain level of multiplexing in the analog readout process. While this multiplexing prolongs the time needed to fully read out a single event, STAR's central event trigger rate of ~ 1 Hz during the first year made this acceptable.

The analog readout of the data is based on the CMOS VLSI front-end chip GASSIPLEX[4] which has 16 multiplexed channels. The 16 channel GASSIPLEX chip has, (for each channel separately), a charge sensitive amplifier, filter, shaper, and a Track/Hold stage to store the charge in a capacitor (see figure 2.29 for schematic diagram of GASSIPLEX chip). The amplifier has an integration time of 650 ns. The filter was designed to accept the greatest part of the signal while reducing the sensitivity of the electronics to the long lasting currents caused by the slowly drifting ions in the MWPC ($\sim 10's$ of μs), and is capable of achieving a stable baseline level restoration in 3 μs. Upon receipt of a fast pre-trigger created by the fast outputs of the CTB slats directly in front the RICH, each channel is opened, allowing the detector currents to energize the capacitors associated with the hit electronics. If no STAR detector trigger is received, a fast clear is sent, resetting all the electronics and leaving the detector ready for the next event within 200 ns. If, however, a STAR event trigger is sent, a HOLD stage is used to hold and maintain the individual signals generated by the detector currents for eventual readout. While the event is being processed, a BUSY signal is sent which prevents the electronics from being cleared until the entire event has been processed.

The GASSIPLEX chips are arranged in a group of three, called a modular array (48 channels). Each pad plane quadrant is divided into 8 columns, with 10 modular

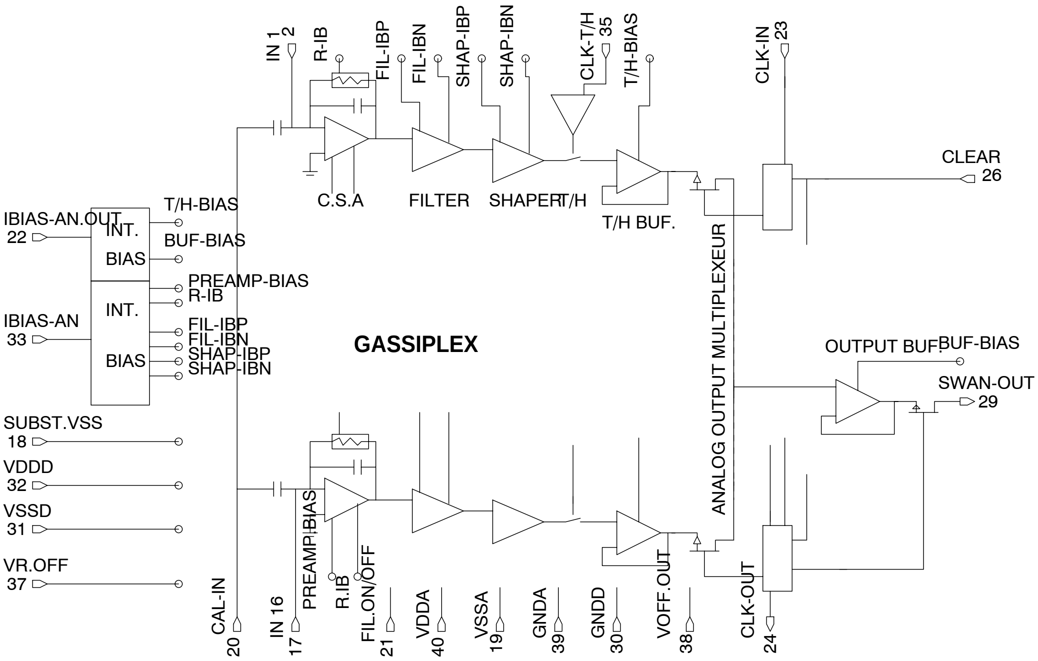

Figure 2.29: Schematics of the functional blocks composing the GASSIPLEX chip used in RICH detector electronics. Picture taken from reference [4].

arrays to a column. Thus each pad plane quadrant has 3840 channels requiring 240 GASSIPLEX chips for readout. The readout chips for all the quadrants are daisy-chained together, allowing the data to be sent over a set of 16 signal cables to a VME readout module. It is at this stage that the digitization and zero suppression of the analog data stream is done. The analog signals received from the detector are transformed into a 10-bit digital signal. The module responsible for this conversion has memories for loading pedestals and threshold tables. A pedestal run was done often during the first year of operation (usually before each new run). These pedestal runs were then used for pedestal subtraction and zero suppression of the data before being sent to the STAR DAQ for packing and eventual storage. Figure 2.30 shows a typical distribution of the pixel ADC values taken during a pedestal run. Each pixel makes a single entry, which corresponds to the pixel's mean ADC value for the events taken during the pedestal run. Figure 2.31 shows the RMS distribution of the pixel ADC values taken during the pedestal run.

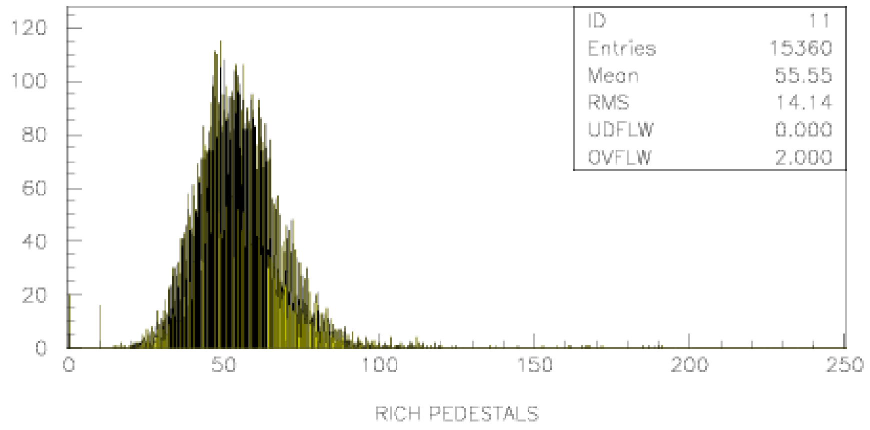

Figure 2.30: Typical distribution of pixel ADC values taken during a pedestal run.

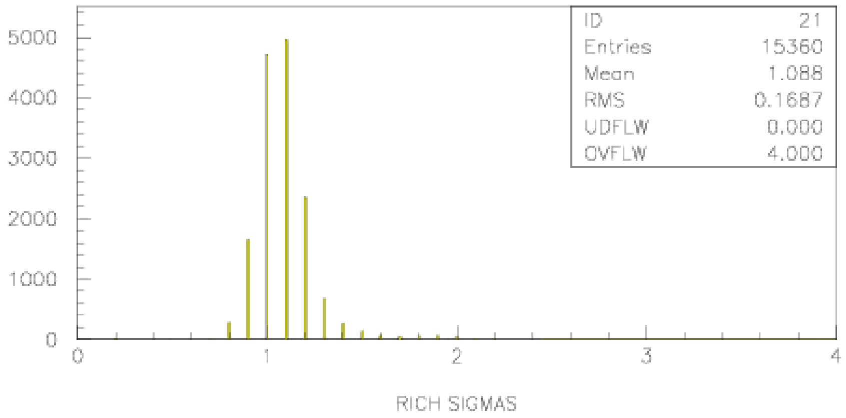

Figure 2.31: Typical RMS distribution of the pixel ADC values taken during a pedestal run.

Table 2.2 lists the materials used in the construction of the RICH detector and their corresponding radiation lengths. The total radiation length of the material travelled through by a typical particle intersecting the RICH is estimated using the radiation lengths of the IFC, OFC, TPC Gas containment vessel, CTB and the RICH, (see Table 2.1 and ref. [26]). It is possible to calculate the average radiation length of the material traversed by a charged particle which intersects the RICH pad plane. The radiation length of the OFC is 2.43%, the gas vessel is 11.74%, the CTB is 20%, and the RICH is 15%, for a total radiation length of approximately 49%. Particles

Table 2.2: RICH detector Mass Composition

Material	Thickness (mm)	Rad. Length (%)
Aluminum Safety Box cover	1	1
Honeycomb front panel	50	2
Neoceram plate	4	3
C_6F_{14}	10	5
Quartz window	5	4
RICH Total		**15**

travelling though this material will be deflected by many small-angle scatters. This will limit the precision with which extrapolations of TPC tracks to the RICH can be performed. The RMS angular deflection suffered by a particle can be estimated using the expression for multiple scattering of particles travelling through matter (equation 2.5 from subsection 2.3.2), giving an RMS deflection $\sim 0.5^\circ$. Compared to the difference in the mean Cherenkov angle between a 2 GeV/c π and P of $39^\circ - 31^\circ = 8^\circ$, this offers no serious impediments to the particle identification process. At a momentum of 5 GeV/c, the angular difference between a π and P becomes $39.365^\circ - 38.158^\circ = 1.2^\circ$ and is comparable to the RMS angular deflection.

Chapter 3

Event Reconstruction

The following sections will describe the event reconstruction in the TPC and STAR-RICH. The tracking models employed for the TPC will be presented with a particular emphasis placed on their effects on the STAR-RICH analysis. Track parameters have to be extracted from the TPC track models in order to proceed with the analysis of the STAR-RICH data and thus play a special role in this analysis.

3.1 TPC Event Reconstruction

The TPC event reconstruction software is given the task of track reconstruction for collisions involving many hundreds of charged particles travelling though its sensitive volume. Besides recording the trajectory of charged particles, the TPC is expected to provide particle identification by measuring the energy loss of the charged particle as it propagates through the gas. This is accomplished by measuring the ionization produced along the charged particle's trajectory in the TPC gas. The reconstruction effort begins by recording the time and position of each charge cluster drifting towards the TPC endcaps. The digitization of the raw information produces $\sim$ 70 million adc values from which the charged particle trajectories have to be found and analyzed.

3.1.1 TPC Space Point Reconstruction

To reconstruct the trajectories of the charged particles travelling through the TPC, the process starts with creating space points from the TPC pixel data, where a pixel is the integer adc value for a pad in a single time bin. The first step is to find groups of pixels which are close together. This is accomplished by starting with an initial pixel above a certain adc threshold, and finding nearby pixels in adjacent padrows and time bins, with each new pixel added being marked as used. This continues until there are no more nearby pixels, whereupon a new unused pixel is used to form a new cluster and the process is repeated. Pixels assigned to a cluster are marked as 'used' and are not considered for new cluster formation. In this way all pixels are used to create a list of clusters for reconstructing TPC space points, or "hits" (see Figure 3.1). Dead, noisy and hot pads (bad pads in general) are taken into account at this stage, along with any relative timing corrections between pads.

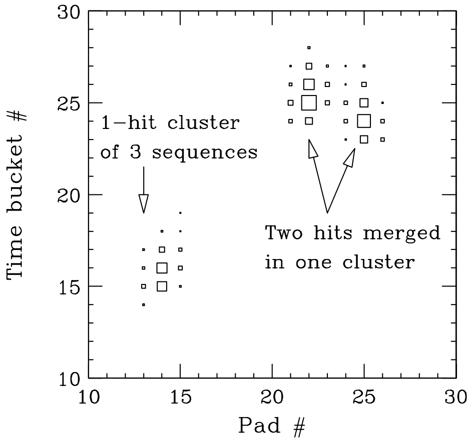

Figure 3.1: Example of 2 clusters found by TPC cluster finder. The cluster on the right has multiple hits, reconstructed using a simple deconvolution algorithm (see Figure 3.2). Figure obtained from ref. [5].

Next, a hit finding algorithm is applied to each cluster. The hit finding algorithm uses the three dimensional information of each cluster pattern to find a local peak or peaks. In order to reduce the amount of computational time spent at this stage of the event reconstruction, a decision is made on a cluster-by-cluster basis how likely the cluster contains two or more hits. This is accomplished by cutting on the width

(RMS) of the cluster pattern in the padrow vs time bins (see figure 3.2). Clusters believed to contain multiple hits are treated separately from the single hit clusters, with particular algorithms applied to find any local maxima. Once the peak, or peaks, belonging to the cluster are found, the position of each is determined in a two step process. The position along the padrow is obtained by a three point Gaussian fit and in the time direction using an offset weighted mean. The uncertainties associated with each space point are estimated based on parameterizations obtained from real data. These parameterizations are based on hit residuals as a function of the track crossing angle relative to the padrow direction. The resolution attained along the longitudinal direction was approximately 500 μm.

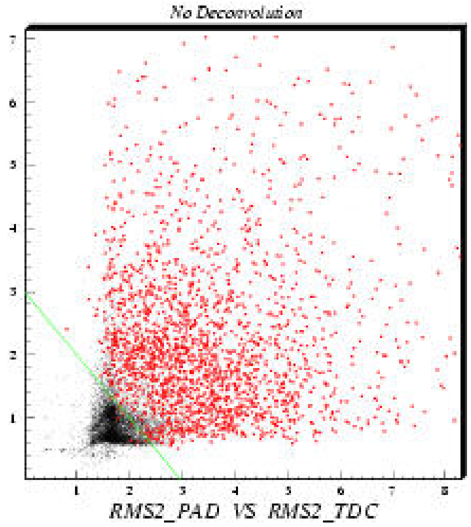

Figure 3.2: TPC cluster RMS, plotted padrow vs time bucket. Black points represent clusters having a single hit, red points are clusters having multiple hits. Figure obtained from ref. [5].

3.1.2 tpt Track Model

The tracking program for the STAR TPC (named tpt) uses a follow-your-nose algorithm first used in earlier experiments like ALEPH and NA35. The first step in constructing a set of tracks is to form a set of track seeds, or roots (see fig. 3.3). This is accomplished by selecting a single hit at the outermost pad row, where the

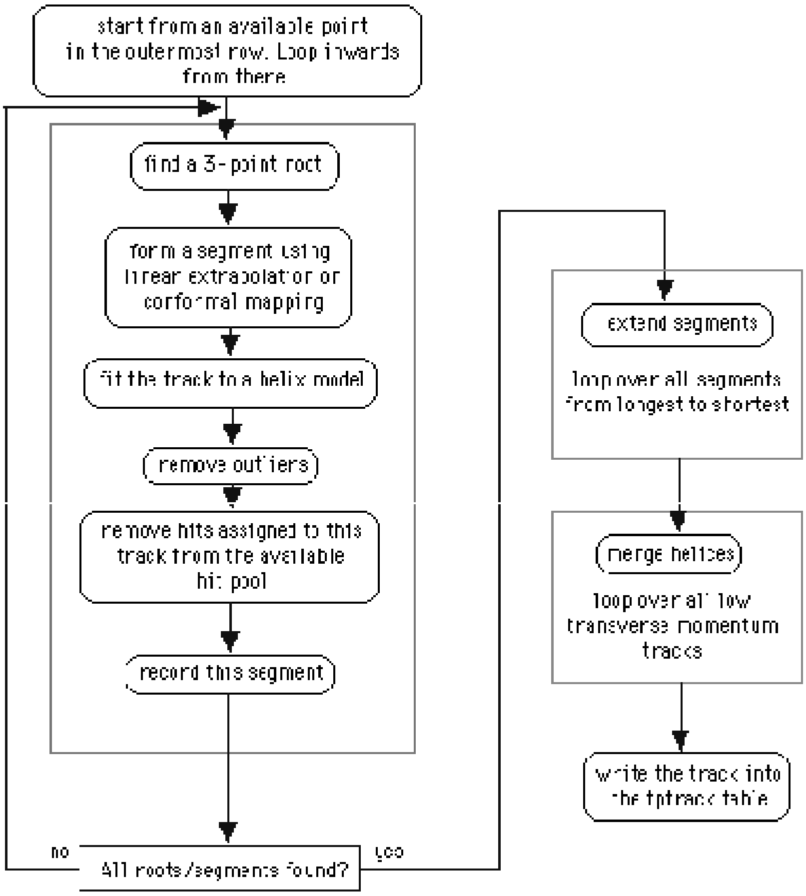

Figure 3.3: STAR TPC tpt flow chart

track multiplicity is smallest, and forming all possible 3-point combinations of points surrounding the initial point. The best candidate from this collection of 3-point combinations, (referred to as a link or root from now on), is then used to form the foundation of a track segment. A straight line parameterization of the track root is then projected inwards. Hits lying along this projection are added to the original collection of points, which now define a track segment (see Figure 3.4 for example).

Once a track segment has been defined, the points making up the segment are removed from the available pool of points and a new root is formed, leading to the creation of another track segment. This continues until all track segments have been formed. Starting with the largest segment, attempts are made to add additional

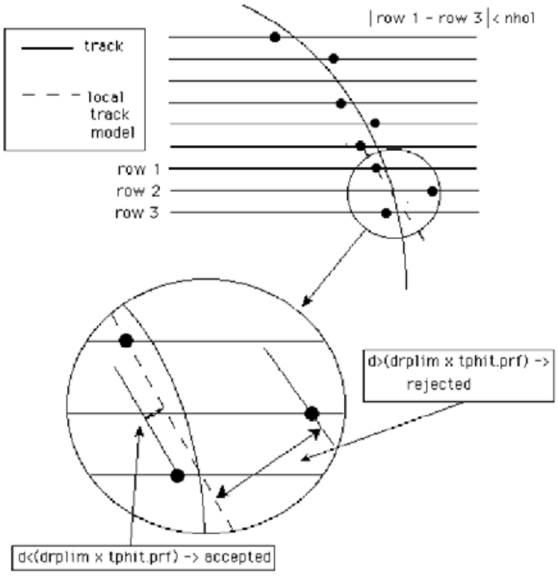

Figure 3.4: Segment formation.

points to each track segment. In contrast to the linear extrapolations used in the initial segment formation, a helical model is used to predict the location of the next hit. All hits considered part of the track segment are used in the helical extrapolation. Hits lying along the helical projection are added to the collection of points defining the track segment and are removed from the pool of points used in forming tracks. This extension of the track segment continues inwards and then outwards until the edge of the TPC is reached, or no points lie close to the tracks extrapolated trajectory. The final step employed in the track finding is to merge any track segments that have become fragmented. This can happen primarily to low transverse momentum tracks having large pathlengths. Track segments having similar helical track parameters are used to form a new track segment.

The trajectory of a charged particle in a uniform magnetic field is best described by a helix. To decrease the computational time needed to determine the physical track parameters associated with each track segment, a circle-line fit is performed in two independent procedures. The transverse momentum of the track can be obtained by fitting a circle to the collection of points projected in the plane perpendicular to the magnetic field vector. The mean squared distance of each point (x_i, y_i) is minimized relative to the circle $(x-a)^2+(y-b)^2=R^2$ by minimizing the functional

$$K(a,b,R) = \frac{M(a,b,R)}{R^2} = \sum_{i=1}^{n} \frac{\left(\frac{x_i^2+y_i^2}{R} - \frac{2ax_i}{R} - \frac{2by_i}{R} + \frac{a^2+b^2-R^2}{R}\right)^2}{w_i}.$$

A simple least squares fit of the track points to a straight line in s-z coordinates then gives the momentum along the beam axis. The track's pathlength is s, and the z coordinate is the point's position along the beam axis. See Figures 3.5 and 3.6 for example. The trajectory of the charged particle can be parameterized in the following form using parameters obtained in the circle-line fits above,

$$x(s) = x_0 + R_H\left[\cos\left(\Phi_0 + \frac{hs\cos\lambda}{R_H}\right) - \cos\Phi_0\right],$$
$$y(s) = y_0 + R_H\left[\sin\left(\Phi_0 + \frac{hs\cos\lambda}{R_H}\right) - \sin\Phi_0\right],$$
$$z(s) = z_0 + s\sin\lambda.$$

The starting point of the helix is denoted by (x_0, y_0, z_0), s is the path length along the helix, λ is the slope (or dip angle) of the helix, R_H is the radius of the helix, h is the sense of rotation of the helix in the x-y plane, and Φ_0 is the azimuthal angle of the track direction at the starting point of the helix. Details of the fitting procedures and a more in-depth discussion of the parameters introduced above can be found in Reference [40].

3.1.3 Global Track Model

Allowances in the STAR software framework have been made for multiple tracking volumes, each capable of providing information to be used in performing track finding. Two main tracking detectors were originally intended to be used by the STAR detector, the TPC along with the SVT, with the possibility of adding additional layers of silicon tracking to increase the tracking quality at points close to the event vertex. Tracks reconstructed in this way were to be referred to as 'global' tracks. In addition to having more information, global tracks were to be reconstructed using a Kalman filter. During the first year of data taking at STAR, one tracking detector (TPC) was used to provide tracking information. Deviations of space points from the track's trajectory due to energy loss and multiple coulomb scattering were incorporated into the global track model. Multiple scattering occurring in the gas volume of the TPC is described using a continuous medium (P10 gas) with the inner field cage acting as an additional source of radiation length. Energy loss is modelled by GEANT using the STAR geometry.

The global track model takes as input to a 3D helix model the points found by the tpt track model. The global tracking is accomplished in three steps. The first step is used to filter the original hits, identifying and removing outliers. The global track is propagated inwards, starting at the outermost hit, removing hits deviating from the trajectory in a gross fashion. Next, a smoothing pass is performed, starting at the inner most point and working its way outwards, incorporating all of the information available, including the energy loss and multiple scattering information. Space points not lying along the tracks trajectory are removed. A third and final pass is done to determine the track parameters and estimate a quality factor for the fitting procedure. Details of the Kalman fitting can be found in Reference [41]

3.1.4 Event Vertex Determination

The next step in the event reconstruction is a determination of the primary interaction point, or event vertex. Accurate reconstruction of the primary vertex is an important part of the global event characterization. Tracks emanating from the primary vertex are found by extrapolating each track to the event vertex and selecting tracks passing within a certain distance from the vertex, typically 3 centimeters. In this way tracks are categorized as primary tracks originating from the primary vertex, or as secondary tracks resulting, for example, from decays of primary particles. Furthermore, accuracy in determining the event's interaction point is an important part of reconstructing a track's momentum vector. Tracks passing within 3 cm from the primary vertex are tagged as originating from the primary interaction and have the primary vertex included in the track fitting, offering an improvement in the momentum resolution of the track.

The method of vertex reconstruction employs a Least Squares Method (LSM) together with removal of outliers to estimate the vertex position. The method starts with an extrapolation of the global tracks back to an initial reference point in the transverse (bend) plane. The beam position is known to a much greater extent in the transverse plane $\sigma_{trans.} \approx 0.5$ mm, $\sigma_{\mathrm{beamaxis}} \approx 90$ cm than along the beam direction and this dictates the initial choice to start the process in the transverse plane. The distance of closest approach, d_i, to a space point along the beam is calculated for each track i. The sum $\chi^2 = \sum d_i^2$ is minimized yielding an estimate for the primary vertex. Tracks extrapolated to points far removed from the initial estimate for the primary vertex can significantly degrade the position resolution and a simple method of eliminating these tracks is used to improve the vertex resolution. The initial reconstructed point is used as a seed to the next iteration where tracks extrapolated to a point far away from the initial vertex are removed, yielding a new estimate for the primary vertex. This process is repeated until a stable result is obtained, typically requiring 3-4 iterations.

The accuracy of the vertex finding for events having a large number of tracks is approximately 150 μm in both the transverse direction as well as the beam direction. The efficiency for finding event vertices having more than 50 primary tracks is near 100%. Event multiplicities used in this analysis are all much more than this number. Additional details on vertex finding can be found in Refs. [42, 7].

3.1.5 Primary Track Model

The determination of the primary event vertex for high multiplicity events is done with a resolution ($\approx$ 150 μm) much better than what is achieved for a single space point reconstructed in the TPC, which is typically around 700μm. Thus the inclusion of the primary event vertex in the fit of the space points for a global track can significantly improve the momentum resolution. A global track pointing back to the primary vertex and having an extrapolated distance of closest approach to the vertex less than 3 cm is considered to have originated from the vertex. Global tracks which satisfy this criteria are termed primary tracks and are subjected to a refit of the track points. The primary vertex, with its much smaller uncertainty, is included in the fit.

Charged particles undertake a helical trajectory in the presence of a static, uniform magnetic field and this helical motion is describable using five parameters. The parameterization presented below describes the helix in cartesian coordinates (x, y, z) expressed in terms of the particle's pathlength, s,

$$x(s) = x_0 + \frac{1}{\kappa}\left[cos(\Phi_0 + hs\kappa\cos\lambda) - \cos\Phi_0\right]$$
$$y(s) = y_0 + \frac{1}{\kappa}\left[sin(\Phi_0 + hs\kappa\cos\lambda) - \sin\Phi_0\right]$$
$$z(s) = z_0 + s\sin\lambda.$$

Listed here are the various parameters used in the above equations:
starting point of the helix x_0, y_0, z_0,
λ is the dip angle,
$\kappa = \frac{1}{R}$ is the curvature,
B is the z component of the homogenous magnetic field ($\mathbf{B} = (0, 0, B_z)$),
q is the charge of the particle in units of positron charge,
h is the sense of rotation of the projected helix in the xy-plane,
i.e. $h = -sign(qB) = \pm 1$,
Φ_0 is the azimuth angle of the starting point (in cylindrical coordinates) with respect to the helix axis, $(\Phi_0 = \Psi - h\pi/2)$,
Ψ is the arctan $\frac{dy}{dx}_{s=0}$, i.e. the azimuth angle of the track direction at the starting point.

The parameters used to describe the helix are obtained in two simultaneous fits to the track points and vertex. A circle fit is made on the space points in the xy-plane, and a straight-line fit is performed in the s-z plane. The circle fit gives the curvature of the helix along with the circle center, x_c, y_c. The line fit gives z_0 and the dip angle, $\tan\lambda$. The parameters important for this analysis are then calculated as follows,
$p_\perp = cqB/\kappa$,
$p_z = p_\perp \tan\lambda$, and
$p = \sqrt{p_\perp^2 + p_z^2}$.

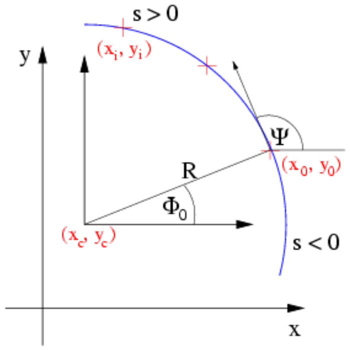

Figure 3.5: Helix projected onto x-y plane. Figure obtained from ref. [6].

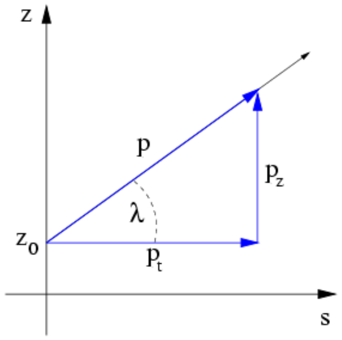

Figure 3.6: Helix projected onto s-z plane. Figure obtained from ref. [6].

3.2 RICH Event Reconstruction

The information recorded by the RICH cathode pad chamber readout consists of signals produced by single-track ionization in the gas and by Cherenkov photons converted in the CsI layer. These signals will produce charge clusters which differ greatly in size, shape and the amount of charge collected. The characteristics of a charge cluster depend on the pad size (8 × 8 mm), induction process and the fluctuation of the charge in the avalanche. Event reconstruction in the RICH attempts to determine the position of every photon and track crossing recorded by the detector. The impact point of the photon or track is referred to as a "hit" and is determined from the information contained in a single cluster. A charge cluster is a collection of one or more pads associated with the charge avalanche produced by either a photo-electron or single-track ionization in the gas. A pad is characterized by its location together with its ADC value and is referred to as a "pixel".

3.2.1 Cluster Finding and Position Resolution

Before the start of a period of data collecting, a pedestal run is done using the RICH detector. During a pedestal run, the RICH detector is triggered, typically 1000 times, before the Au+Au collisions are scheduled to occur. The mean ADC value of each pixel is determined from this set of pedestal runs. The mean ADC value for each pixel is then subtracted away from the pixel ADC values collected during a Au+Au collision. This process is called pedestal subtraction and is done for every event. (Figure 2.30 shows a histogram of the pixel ADC values for a typical pedestal run.)

The cluster finding algorithm begins by selecting an initial pixel from the set of pixels having ADC values above the pedestal threshold. Starting with this seed, any pixels adjacent to the initial pixel are added to a collection which will define the charge cluster. A similar search for adjacent neighbors is conducted for each new addition to the list of pixels defining the charge cluster. This continues until no new pixels are found adjacent to the cluster. Pixels added to the cluster are removed from the pool of available pixels used in forming new charge clusters. Clusters containing many pixels can have more than one local maximum. Thus, a search is conducted for any local maxima contained in the cluster which lie within a square region extending three pixels on a side. The 3x3 pixel matrix defining the search region is shifted about in an iterative fashion to position the center of the matrix on the local charge maximum. The center of gravity of the cluster using the ADC value of each pixel

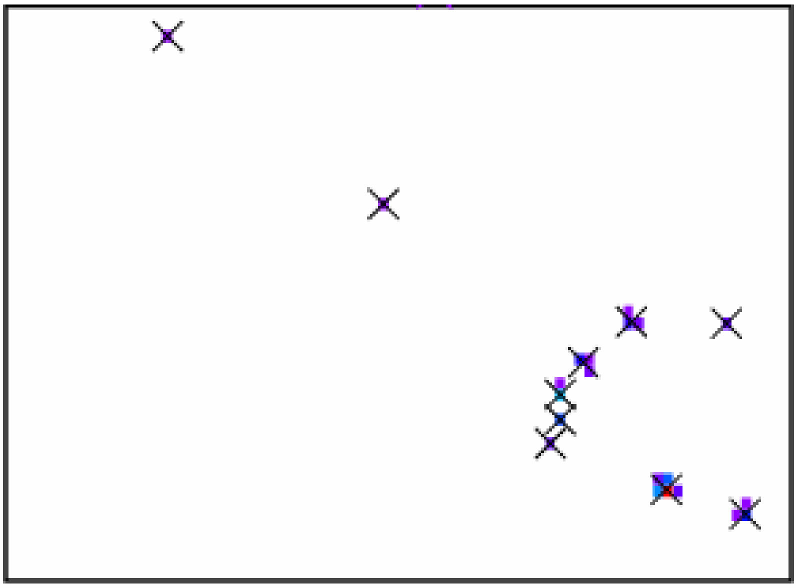

Figure 3.7: Display of one RICH pad plane quadrant taken from a central event. Reconstructed position superimposed over each charge cluster with cross. A charged particle has passed through the RICH, producing a partial ring on the pad plane.

is used to determine the centroid position of the cluster along the two orthogonal directions. Hits having a reconstructed centroid which falls more than one pad away from the center of the search matrix are subjected to a refit using a search matrix centered at the new centroid position. Large clusters can have more than one search matrix applied to deconvolute multiple hits within the single cluster.

Figure 3.7 shows a single quadrant of the RICH pad plane. Charge clusters are seen in the Figure, with the individual pixels making up each cluster shown in a color indicative of their ADC value. A charged particle passed through the RICH radiator, producing a partial Cherenkov ring on the pad plane. The charged particle produced a large charge cluster marking its intersection point with the pad plane, which is surrounded by a group of pixels in a ring, all of which are smaller in size. The reconstructed position of the cluster is shown as a cross superimposed on each cluster. The position resolution depends on a number of factors, most notably the number of pixels making up the cluster. Cherenkov photons typically form clusters having 1-2 pixels and will thus have the worst resolution, typically that of a single pad $\sim 2 - 2.5$ *mm*. Charge clusters formed by single-track ionizations in the gas

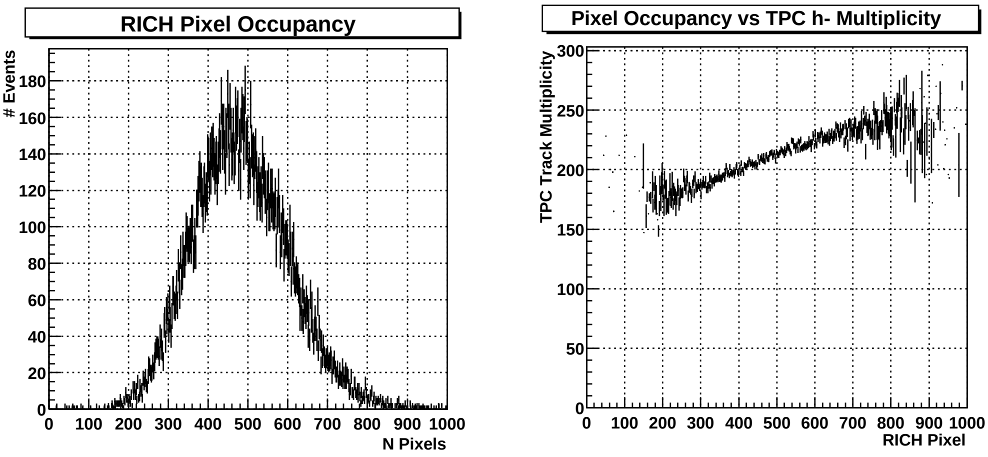

Figure 3.8: Pixel Occupancy for 14% most central Au Au events at $\sqrt{s_{NN}}$=130 GeV. Left panel: Vertical axis shows number of events, horizontal axis shows the number of pixels above threshold. Right panel: Number of TPC negatively charged primary tracks vs RICH pixel occupancy.

will typically have a much larger size, 4-5 pixels, along with a better resolution of $\sim 0.3mm$.

The pixel occupancy is the sum of the pixels above the pedestal threshold in a given event. During the first year of running, the typical pixel occupancy for the 14% most central data set was $\sim$ 3%, and ranged from a low of $\sim$ 0.5% to a maximum occupancy 5%. Figure 3.8 shows the Pixel occupancy for the RICH detector for the 14% most central events during the first years running at $\sqrt{s_{NN}}$=130 GeV. The left panel shows the RICH pixel occupancy (horizontal axis) for a given set of events, while the right panel shows the RICH pixel occupancy vs the number of primary tracks with a negative charge in the TPC.

Chapter 4

RICH Data Analysis

High momentum charged particles can be identified at STAR using the RICH detector. The operating principle of the RICH is the detection of the Cherenkov radiation produced by charged particles passing through a radiating volume. The Cherenkov radiation is emitted in a cone whose opening angle is determined by the particle's velocity. Imaging the cone onto a detection plane, a Cherenkov ring is produced. In general the shape of the ring will be as described in Equations 4.17 and 4.19, where for a normally incident particle a circular ring will be imaged onto the pad plane. In the case of a normally incident particle, the radius of the circle is directly proportional to the particle's velocity. Particle's striking the RICH at angles other than normal produce complicated shapes of light on the detection plane. The velocity information can still be obtained from the pattern described on the detection plane. The particle's momentum together with the velocity information is then enough to provide a measurement of the particle's mass.

In this section, the event triggering and selection process used for the data presented in this thesis will be discussed. The RICH relies on the tracking provided by the TPC to perform particle identification. The placement of the RICH detector outside of the TPC at a radial distance from the interaction of approximately 2.5 meters offers a large lever arm which can be used as a tool in determining the track quality. Tracking errors will be assessed and their effects on the RICH data analysis discussed.

4.1 Event Selection

The ZDC's provided a common triggering system for the four experiments at RHIC and in addition were used to monitor the collision rates at the interaction points. The STAR experiment used the ZDC's along with the CTB to provide a number of different triggers, including an ultra-peripheral trigger, minimum bias trigger as well as a central trigger. A minimum bias trigger was set up by requiring a coincidence between the East and West ZDC's with a summed signal greater than $\sim 40\%$ of a single neutron signal. A correlation between the number of neutrons detected in the ZDC's and the signal seen in the CTB is shown in Figure 4.1. The sum of the East and West ZDC signals is plotted vs the CTB signal and shows a characteristic

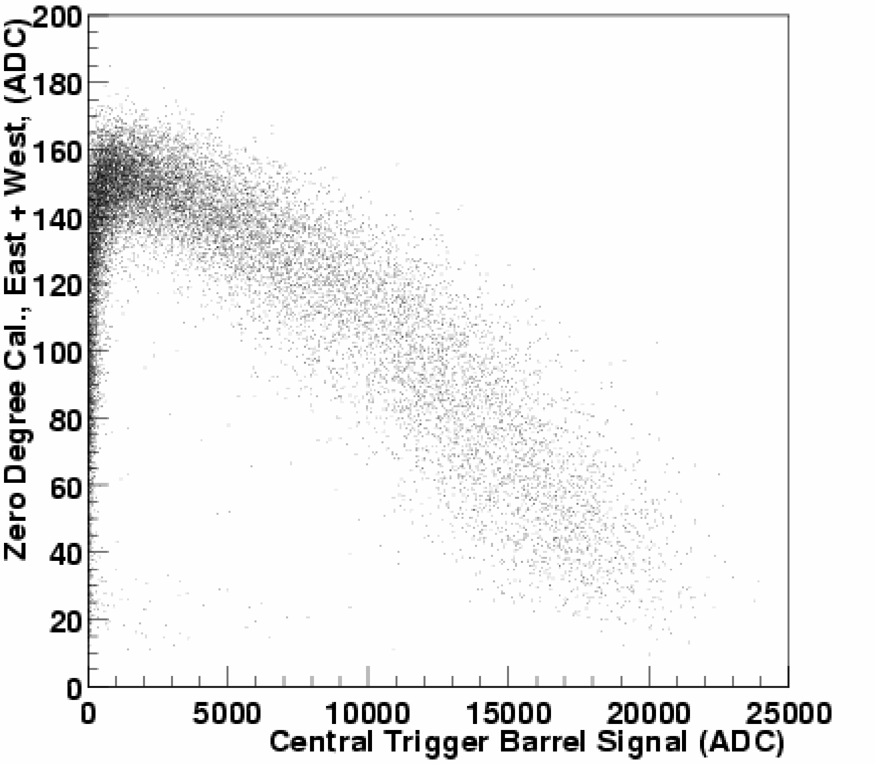

Figure 4.1: The summed East-West ZDC signal vs CTB signal for a small sample of events. Central events are characterized by high counts in the CTB and small ZDC sums. [7]

"boomerang" shape. Collisions between nuclei having a small geometrical overlap result in a small number of dissociation neutrons detected in the ZDC along with a correspondingly low CTB signal. These peripheral events occupy the lower left corner in Figure 4.1. Increasing the geometrical overlap between the colliding nuclei results in a larger number of neutrons detected in the ZDC's along with a larger CTB signal, indicating an increase in projectile dissociation and in the particle production at mid-rapidity. Eventually, a point is reached where the geometrical overlap, or "centrality", is great enough such that many of the neutrons are within the reaction volume, leaving less and less to be detected in the ZDC's. Thus the particle multiplicity, along with the corresponding CTB signal, grows with centrality while the ZDC signal grows less and less. The lower right hand corner of Figure 4.1 consists of the most central events where the CTB signal is largest and only a very small ZDC signal is recorded.

4.1.1 Central Events

A measurement of the total cross section for the Au+Au collisions at $\sqrt{s_{NN}} = 130\,GeV$ was performed by three of the four RHIC experiments using the ZDC's as a minimum bias trigger with STAR reporting a preliminary result of $8.9 \pm 0.3_{stat.} \pm 0.7_{syst.}\ b$. The cross section was measured using the van der Meer scan technique reported in [43]. The ZDC's are sensitive to the neutral energy going in the forward direction which will consist of neutrons resulting from nuclear interactions between the Au nuclei as well as mutual Coulomb Dissociation [44]. Thus what is measured is the combined cross section for minimum bias nuclear interactions plus that of mutual Coulomb Dissociation. The theoretical value calculated for this total cross section is $10.9 \pm 0.6\ b$ [44], in apparent disagreement with the experimental value of $8.9 \pm 0.3_{stat.} \pm 0.7_{syst.}\ b$ reported above. This difference between the calculated and measured total cross section is not understood and is being investigated.

The quantity of interest is the hadronic cross section, σ_{AuAu}, which has to be extracted from the total cross section as determined above. As discussed in another STAR thesis [7], the procedure to do this is not a trivial one, and thus only the conclusions relevant to this analysis will be presented here. The events selected for this analysis were obtained by requiring a high signal in the CTB and correspond to a cross section representing the ~ 14% most central events. Figure 4.2 shows the data sample used in this analysis consisting of approximately 800K events.

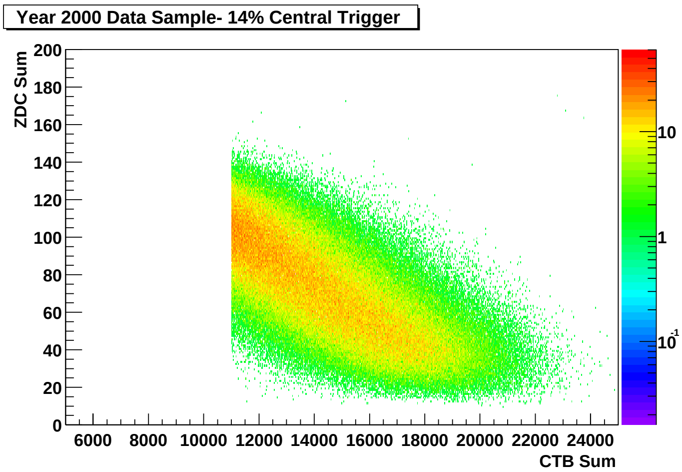

Figure 4.2: The summed East-West ZDC signal vs CTB signal for 14% most central events.

4.1.2 Vertex Acceptance

The large event diamond present in the first year of data taking at RHIC resulted in events being reconstructed with primary vertices ranging along the entire length of the TPC. The vertex distribution was approximately Gaussian with a spread of $\sigma_z \sim 90$ cm. Collisions occurring outside the bounds of the TPC were observed to have produced tracks in the TPC, which in principle allowed these events to be reconstructed. However, no attempts were made to reconstruct these poor quality events. The RICH detector is centered in the TPC at mid-rapidity and extends only ±65 cm along the beam axis. Tracks striking the RICH at large angles produce incomplete patterns on the RICH pad plane and thus are of low quality. This then dictates selecting events having vertices reconstructed directly over the RICH which allows the majority of particles to strike the detector at near normal angles. Events having vertices reconstructed along the beam axis within ±70 cm were selected for this analysis. This represents a cut which is smaller than $1\sigma_z$ and sharply reduces the number of events available for the analysis. A fast online trigger[45] was used to enhance the number of central events having vertices within ±90 cm of the center of the TPC.

4.2 Primary Track Matching with RICH

Predicting the Cherenkov light pattern produced by a charged particle intersecting the RICH radiator requires a determination of the particle's momentum vector and entry point at the radiator. The helical parameterization of a primary track can be used to predict the position and orientation of the charged particle's momentum vector at the intersection of the helix and the plane of the RICH radiator (see Figure 4.3 for example). The plane representing the RICH radiator can be described by it's normal vector, $\overrightarrow{n}$, together with an arbitrary point lying within the plane, $\overrightarrow{r}$. The vector $\overrightarrow{p}$ will represent the intersection point and will necessarily satisfy

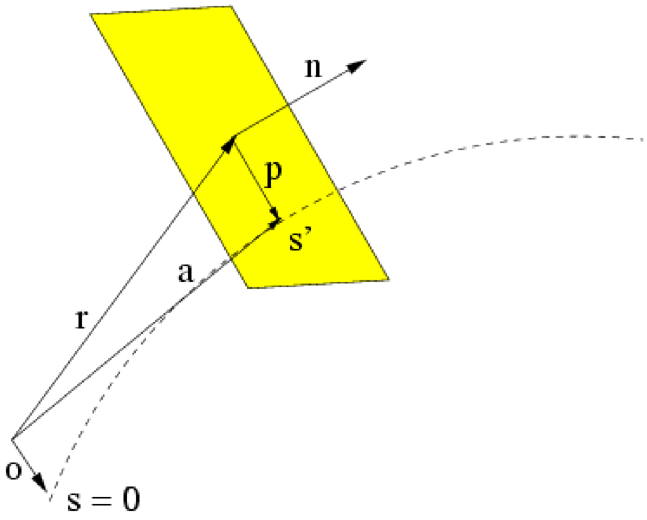

Figure 4.3: Helix intersection with plane. Figure obtained from ref. [6].

$$\overrightarrow{p} \cdot \overrightarrow{n} = 0 \tag{4.1}$$

as it lies within the plane described by $\overrightarrow{n}$ and $\overrightarrow{r}$. Therefore, the vector $\overrightarrow{a}$ describing the particle's trajectory at the point of intersection $\overrightarrow{p}$, can be obtained from the same equation,

$$\overrightarrow{p} \cdot \overrightarrow{n} = (\overrightarrow{a} - \overrightarrow{r}) \cdot \overrightarrow{n} = 0. \tag{4.2}$$

The vector describing the helix at the point of intersection is known as a function of the pathlength s, allowing the above equation 4.2 to be solved,

$$\begin{aligned}&x(s)n_x + y(s)n_y + z(s)n_z - \overrightarrow{r} \cdot \overrightarrow{n} = 0 = \\ &\kappa\,(\overrightarrow{a} \cdot \overrightarrow{n} - \overrightarrow{r} \cdot \overrightarrow{n}) - n_x \cos\Phi_0 - n_y \sin\Phi_0 + n_x \cos S + n_y \sin S + \kappa n_z s \sin\lambda,\end{aligned}$$

with $S = hs\kappa \cos\lambda + \Phi_0$. The root of this equation can be obtained via numerical methods[6] to yield the pathlength s, and thus the particle's momentum vector and position at the point of intersection with the RICH radiator. This method can be similarly used to predict the helix's intersection with the RICH pad plane, with the advantage that this prediction can be compared with the measured intersection point.

4.2.1 Proximity Matching of RICH Clusters

TPC tracks intersecting the RICH pad plane will deposit energy in the MWPC, resulting in the creation of a large amount of charge deposited onto the pad plane marking the particle's intersection with the pad plane. This charge cluster can then be associated with the track's predicted intersection by a proximity matching algorithm. Charge clusters lying within two centimeters of the track's predicted intersection with the pad plane are considered candidates for matching. In the relatively rare case of more than one candidate, a cut on each of the candidate's summed adc value is applied using predetermined thresholds for each quadrant, reducing the possibility of matching a charge cluster resulting from the interaction of a photon with the cesium iodine. Thus, in the ambiguous case of more than one cluster lying near the predicted intersection point, only charge clusters having a summed adc value above a high threshold cut are used, with the charge cluster with the largest summed adc value

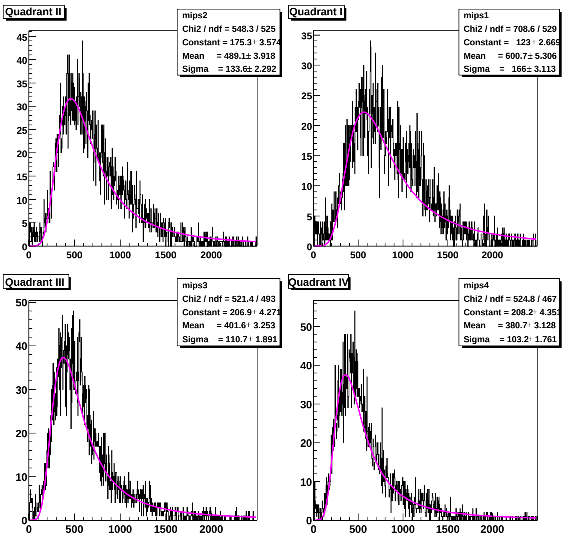

Figure 4.4: RICH Mip cluster adc

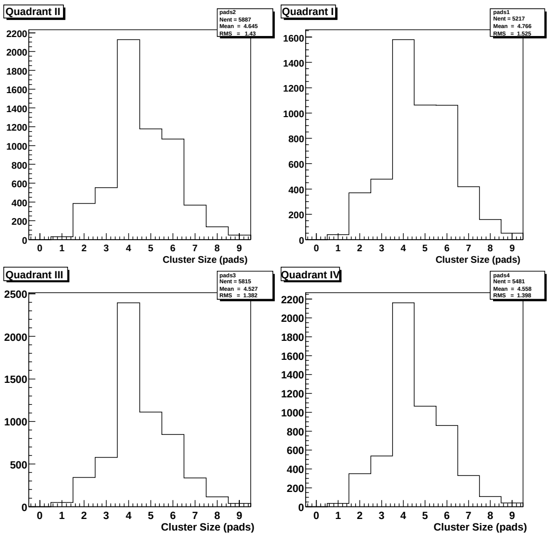

Figure 4.5: RICH Mip cluster size

being selected. Figure 4.4 shows the summed adc value for clusters (Mip clusters) matched to TPC primary tracks. The summed adc values are well approximated by a Landau distribution, and are plotted separately for each pad plane quadrant. Figure 4.5 shows the cluster size in pad units separately for each quadrant.

4.2.2 RICH Detector Alignment

The helix projection to the RICH pad plane requires knowledge of the RICH position relative to the TPC. This was accomplished in an iterative fashion, first using as a rough guide the position of the RICH as determined by a survey. This was followed by a 'fine-tuning' using TPC tracks which will be discussed in the next section. The survey data describing the orientation and position of the RICH detector in the STAR magnet coordinates was generated by the Survey and Alignment Group (SAG) at Brookhaven National Laboratory. There are twenty surveyed points on the RICH detector. Eight of the points are internal to the RICH safety box, with the remaining twelve points external. The eight internal points are located on the back plane of the detector, facing the interaction region. Six of the twelve external survey reference points are positioned on the east face of the safety box, and the remaining six on the west.

Two surveys were conducted on the RICH detector. The first was made before the RICH was inserted into the STAR magnet for the purpose of determining the position of the internal survey points relative to the external points. The second survey was made after the RICH was placed inside the STAR magnet. This survey fixed the position of the twelve external points relative to the STAR magnet. This then constitutes a measurement of the position and orientation of the RICH detector within the TPC magnet. The center of the RICH is defined at the center of the pad plane, and in the global coordinate system is located at $\vec{o} = 120.0957\widehat{x} - 207.9375\widehat{y} - 0.5589\widehat{z}$, a radial distance of ~ 240 centimeters from the origin. The unit normal vector defining, together with the origin, the RICH pad plane was determined to be $\widehat{n} = -0.49723\widehat{x} + 0.86762\widehat{y} - 0.00035\widehat{z}$.

4.2.3 RICH Residuals

The difference between the predicted and the actual intersection point can be used as a track quality parameter and is commonly referred to as a residual. A small residual measured at the pad plane implies a small difference between the predicted and the actual intersection point at the RICH radiator, which is not actually measured. Thus it is desirable to select tracks having small residuals at the pad plane, as this implies a well defined intersection at the RICH radiator where the Cherenkov light originates. The residual between a track's predicted and actual intersection point can be resolved in the TPC's drift direction as well as in the TPC's bending plane, and are well approximated by Gaussians, as shown in Figure 4.6.

RICH Detector Alignment Using TPC Tracks

The position and orientation of the RICH detector has been determined by a survey of the RICH with respect to the STAR magnet system, as described in the previous section. Additional measurements of the position of the RICH can be made using the TPC tracks and their measured intersection points with the RICH pad plane. An iterative procedure was used to fine-tune the position of the RICH, starting with TPC tracks pointing to the RICH having $|\eta| < 0.05$. The restrictive cut on the track's $|\eta|$

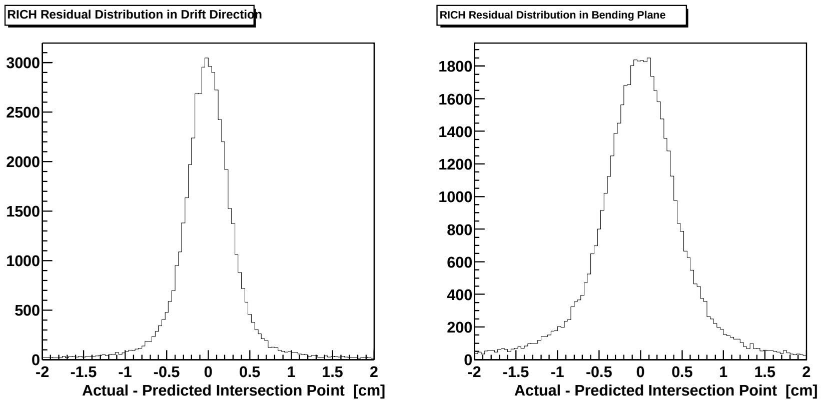

Figure 4.6: RICH residuals in drift, bending directions. Tracks were selected having transverse momentum $1.0 < p_{\perp}[GeV/c] < 1.5$.

essentially selects tracks having a straight line projection in the s-z plane, (i.e. all points having the same z value). These tracks have similar drift times for all points on its trajectory. To cover the entire RICH pad plane, tracks were selected from events having vertices reconstructed directly above the RICH. Residuals from this sample of tracks had small (~ 1 mm) mean offsets in the drift and bend directions. The origin of the RICH was then moved to fix the offsets in the residual means to values compatible with zero (within error). This shifting of the RICH origin can then influence the radial position of the RICH with respect to the STAR magnet. Tracks striking the RICH at large polar angles were then used to fix the radial position of the RICH. To accomplish this the restrictive $|\eta|$ cut was relaxed and residuals were studied as a function of the angle made by the track in the drift and bend directions. Mean offsets were again fixed to values compatible with zero by moving the RICH in the radial direction. Moving the RICH in the drift-bend planes and then in the radial direction was done in an iterative fashion, requiring a few iterations to arrive at the final position of the RICH used in this analysis. Changes made to the survey position were on the order of 2 mm, with the new position being $\overrightarrow{o} = 120.2930\widehat{x} - 207.9396\widehat{y} - 0.3090\widehat{z}$.

Residual Sensitivity to TPC Tracking Errors

The RICH's position outside of the TPC volume at a radial distance of approximately 2.5 meters furnishes a means of making independent assessments of the TPC tracking. The large radial distance of the RICH provides a long lever arm in which to study the effect on the RICH residuals for such things as electric and magnetic field distortions, inclusion of primary vertex in primary fit, and errors in the TPC drift velocity. These effects are not all independent (or known!), making an interpretation of the data difficult at the present time. In light of this, efforts were made to understand the effect of any systematic error in the TPC tracking, and not the cause.

The residual distribution can be fitted to a Gaussian plus a flat background, with the expectation of the mean of the Gaussian being close to zero. This expectation of a mean of zero would indicate that the TPC tracks point, on average, to the predicted intersection point at the RICH pad plane. Figure 4.7 shows the mean residual resolved in the TPC drift direction plotted vs the track's measured intersection point on the RICH pad plane. TPC tracks pointing to the RICH having transverse momenta above 1 GeV/c and $|\eta| < 0.05$ were selected for the following residual study. The restrictive

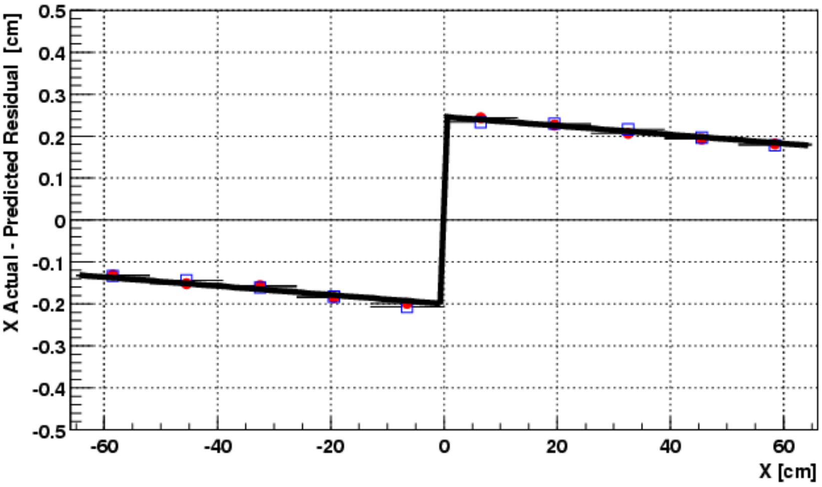

Figure 4.7: RICH residuals in drift direction plotted vs track's impact point in drift direction for $|\eta| < 0.05$.

cut on the track's $|\eta|$ essentially selects tracks having a straight line projection in the s-z plane, (i.e. all points having the same z value). These tracks have similar drift times for all points on its trajectory. To cover the entire RICH pad plane, tracks were selected from events having reconstructed vertices ±70 cm of the center of the TPC. Positively and negatively charged particles were considered separately, and are shown in the same figure. Positive tracks are shown in red, negative in blue. The abscissa shows the track intersection point on the pad plane resolved along the TPC drift direction and ranges from -65 cm to +65 cm. The ordinate shows the Gaussian mean of the RICH residual resolved in the TPC drift direction. A systematic offset of the mean is seen in the residuals, and has a dependence on the tracks intersection point. The offset is greatest near the center of the RICH corresponding to tracks with the largest drift times and decreases in a linear manner for tracks having smaller drift times. The effect in the residuals is of the same magnitude in the two halves of the RICH and has a shape which is suggestive of a small error in the TPC drift velocity. The residual means were fitted to the following function,

$$\frac{x}{|x|}\left(A - A\frac{|x|}{B}\right) + C \tag{4.3}$$

where A and C are free fit parameters. The parameter B is half the effective length of the TPC, B = 210.334 cm. The values obtained from the fit are $A = 0.22$ cm and $C = 0.024$ cm. The C parameter is a measure of a global offset from zero and A gives a measure of the magnitude of the effect at its greatest. The linear decrease in the mean offset on either side of the TPC is suggestive of a small error in the TPC drift time which is made evident by the long lever arm of the RICH. While the linear nature of the residual offset is suggestive of a drift velocity error, it is not conclusive. Nevertheless, taking the slope on either side gives a fractional error on the TPC drift time of 0.001. This is on the order of the accuracy achievable by the TPC drift time calibration. Corrections can be made to account for this mean offset in the track's predicted intersection point with the RICH pad plane. This is done by shifting each track's predicted intersection with the plane in the drift direction by the amount indicated by the fit. The same correction is applied to the tracks predicted intersection with the RICH radiator.

A similar analysis was done for the residuals in the bending plane. Figure 4.8 shows the residuals resolved in the bending direction plotted vs the track's intersection point in the bend plane. This is done using the same track sample used in the above residual study. The residuals are made for tracks whose intersection points in the drift direction are restricted to lie in a small range on the RICH pad plane. This

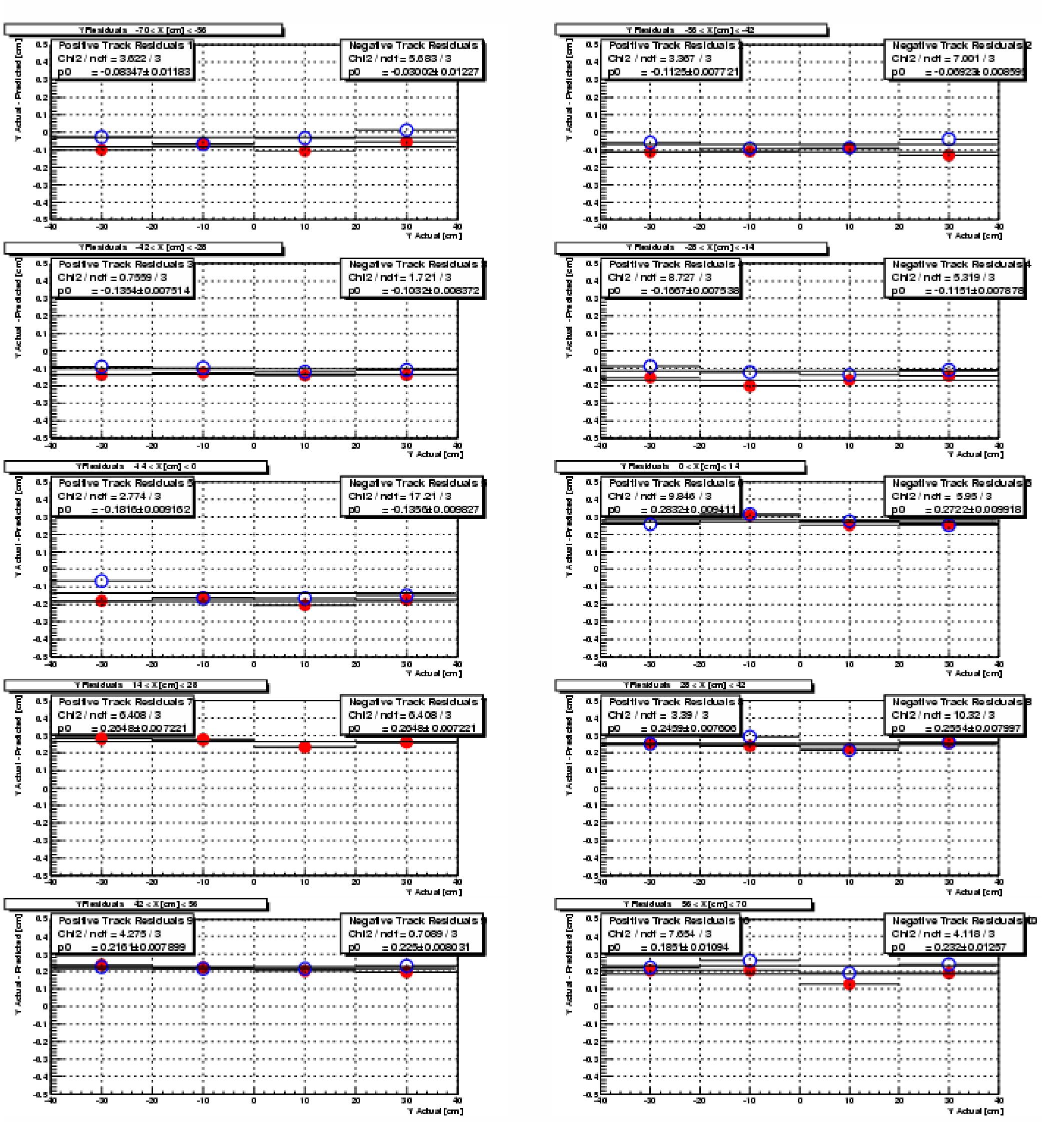

Figure 4.8: RICH residuals in bend plane plotted vs track's impact point in bend plane for $|\eta| < 0.05$. Each figure is for a separate slice in the drift direction.

is done for ten different ranges, or slices, in the drift direction. Thus Figure 4.8 shows the bending plane residuals vs the track's intersection point in the bending plane for different slices in drift direction. Starting in the upper left, the first panel represents the extreme eastern portion of the RICH pad plane. The lower right hand panel then represents the western most portion of the RICH pad plane. The bending plane residuals are flat as a function of the track's intersection point in the bending direction for each slice in the drift direction. However, the mean value of the bending plane residual is different for each slice in drift direction. This is an indication of a dependence on the TPC drift distance. Figure 4.9 shows the bending plane residual as a function of the track's intersection point in the drift direction. Positive (red, closed circles) and negative (blue, open squares) tracks are treated separately and are plotted together on the same figure. Plotted along the ordinate is the track's residual resolved along the bending direction and the abscissa shows the track's intersection with the pad plane in the drift direction. Positive and negative tracks show similar trends, with a slight difference being evident on the eastern side of the detector. A linear dependence on the drift time is clear, but the east and west halves of the detector show different systematics. A straight line fit was done for the points on

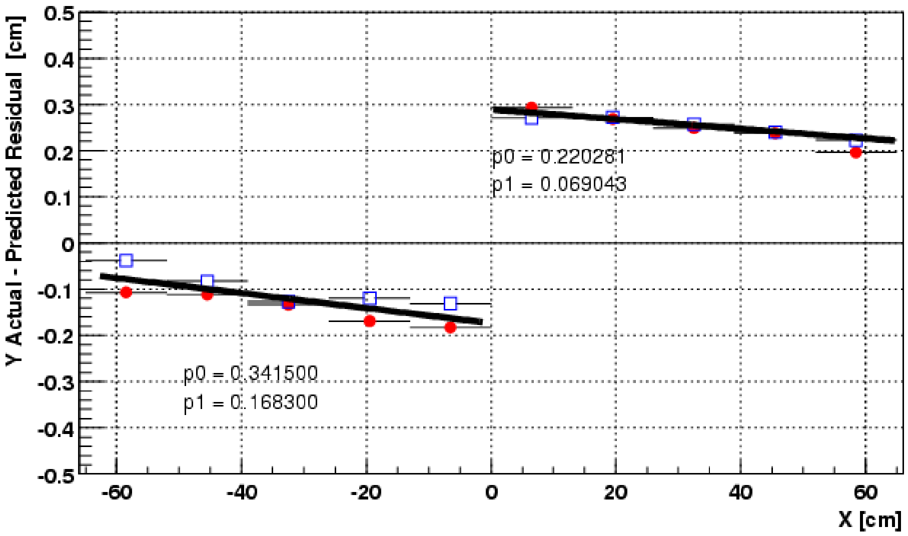

Figure 4.9: RICH residuals in bend direction plotted vs track's impact point in drift direction for $|\eta| < 0.05$.

either side of the detector. The bending plane residuals on the east have a slope of 0.1683 with an intercept of 0.3415 cm. The parameters extracted from the western points give a slope of 0.069943 and an intercept of 0.2202 cm. The cause(s) for this systematic offset in the residuals in the bending plane is(are) not known. Corrections to the TPC track's intersection with the RICH radiator and pad plane are made in the same way as the drift direction corrections were made. The TPC track's intersection point in the bending plane is shifted according to the results from the fits.

The residuals in the drift direction and bending plane vs the track's η are shown for positive and negative tracks in Figure 4.10. Mean offsets of $\sim 1 - 2$ mm are evident in the drift and bend directions. Similar effects are seen in the residuals when plotted vs transverse momentum as in Figure 4.11 for tracks with $|\eta| < 0.3$.

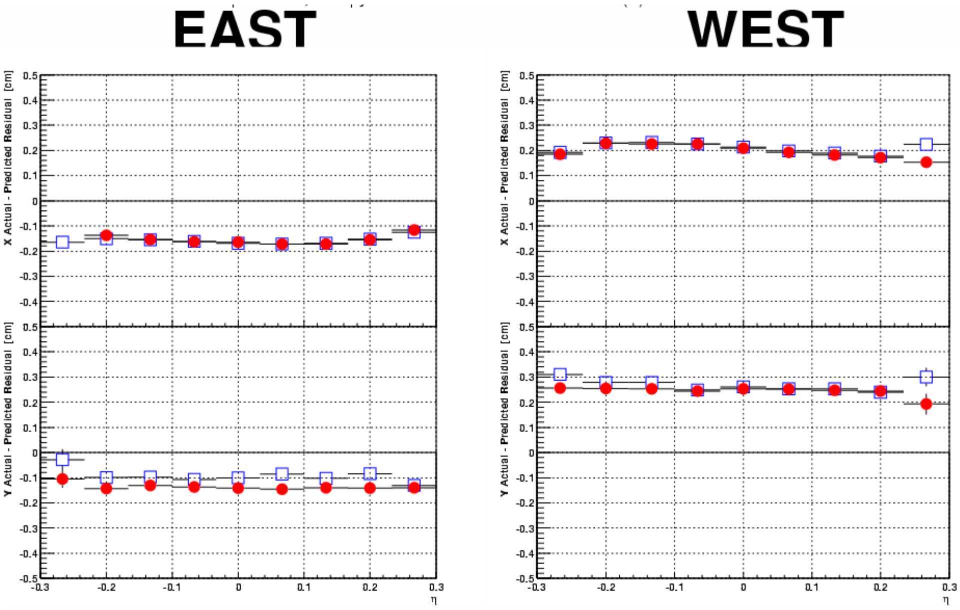

Figure 4.10: RICH residuals in drift, bend directions plotted vs η.

Application of the above corrections yield residuals vs η and $p_\perp$ which are relatively flat and centered at zero as seen in Figures 4.12 and 4.13. The corrected residuals are problematic at large η even after the corrections. The tracks used in the remainder of the analysis will thus be restricted to $|\eta| < 0.2$. Regardless of the cause of these systematic offsets in the residuals in both the drift direction and bending plane, the effect on the RICH analysis can be estimated. Assuming the track is rotated in the

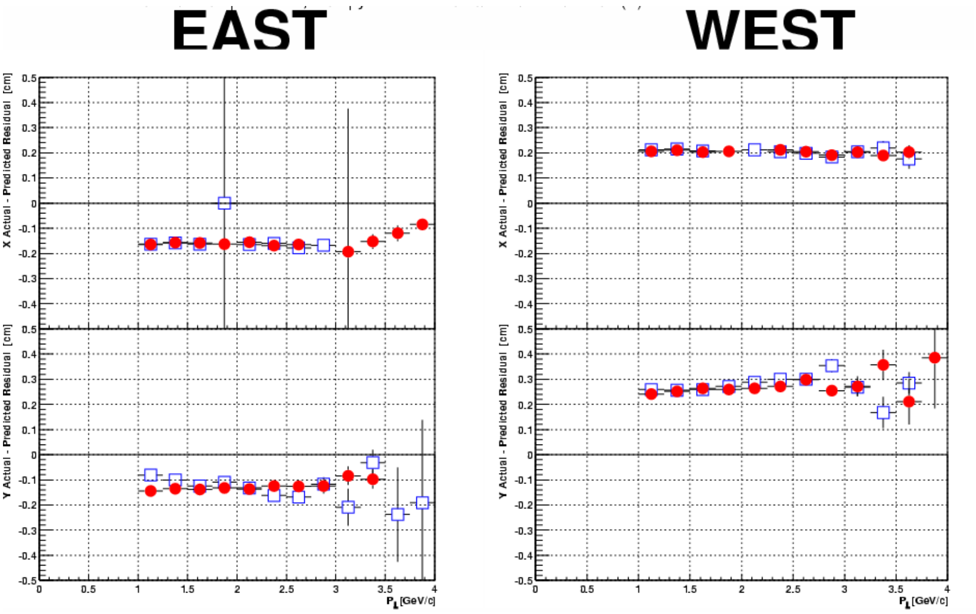

Figure 4.11: RICH residuals in drift, bend directions plotted vs $p_{\perp}$.

TPC due to some unknown reason resulting in the residual offset, the systematic error in the determination of the angle made at the RICH radiator can be calculated. The track travels $\sim$ 2.5 m and the residual offset is $\sim$ 2.5 mm (in the worst case). This implies an error of $\frac{2.5 \text{ mm}}{2.5 \text{ m}} = 1$ mrad $= 0.05$ degrees which is negligible. The pattern of Cherenkov light produced on the RICH pad plane will lie within a narrow band surrounding the track's intersection point (see next section for detailed discussion) and will typically have a width of 1 - 2 centimeters. Thus the tracking irregularities causing the systematic offsets in the residuals have a limited impact on the RICH pattern recognition algorithms used in this analysis.

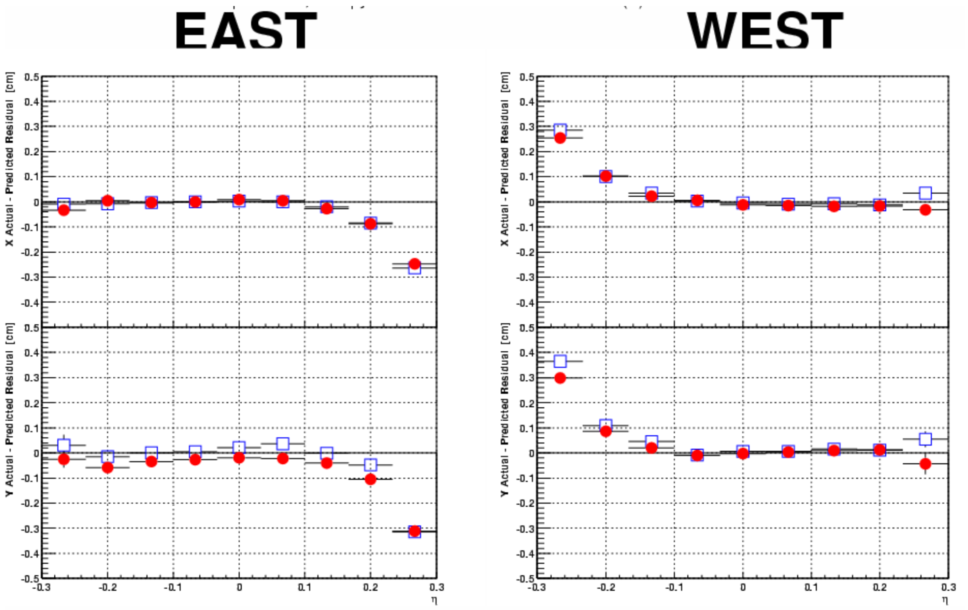

Figure 4.12: RICH residuals in drift, bend directions after corrections plotted vs η.

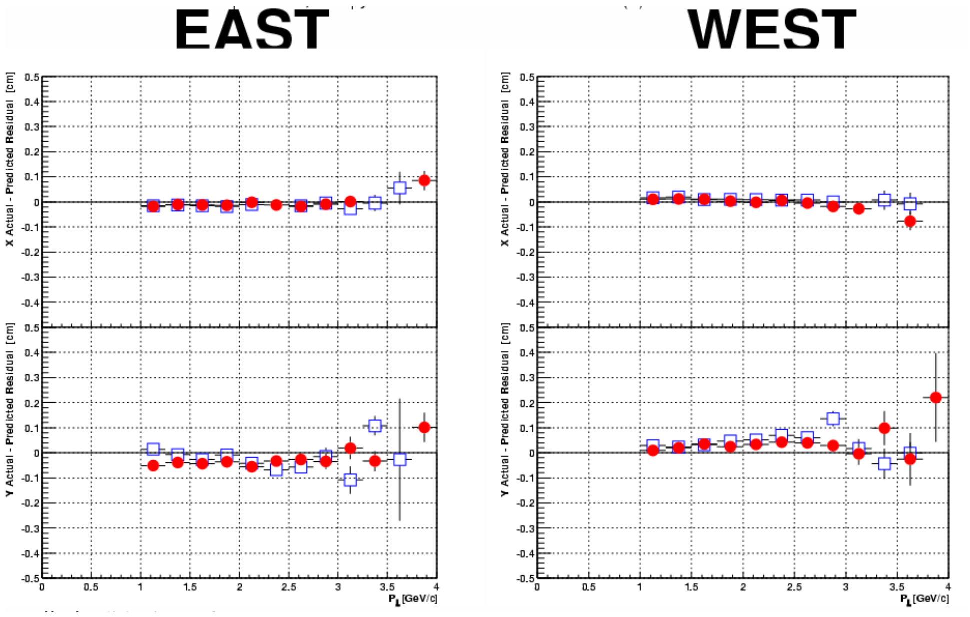

Figure 4.13: RICH residuals in drift, bend directions after corrections plotted vs $p_\perp$.

4.3 Description of Analytical Solution for Pattern Recognition

Particle identification using a Ring Imaging Cherenkov detector is essentially a problem of pattern recognition. A pattern recognition algorithm typically reconstructs a mean Cherenkov angle of the photons found within a certain fiducial area on the detection plane. The mean Cherenkov angle then yields a mass when combined with a momentum measurement. The mass obtained in such an analysis is in principle allowed to have any value, even values which are non-physical. The pattern recognition algorithm employed in this analysis takes advantage of the fact that the particle mass spectrum is discrete and limited in scope (the set of stable particles expected to survive long enough to reach the RICH is small i.e. e, μ, π, K, P). The masses of the e, μ and π are close enough such that the expected Cherenkov patterns for these different masses are indistinguishable for momenta above ~ 0.5 GeV/c. Thus particle identification is needed for only three sets of masses, π, K and P. Rather than attempt to reconstruct the Cherenkov angle for these masses, one can predict the expected Cherenkov Fiducial areas on the detection plane and simply compare the light found on the RICH detection plane with the expected pattern for each hypothetical mass.

The following analytical solution will define the fiducial area on a detection plane which contains the Cherenkov light produced by a charged particle traversing a planar radiator of thickness d_{rad}. The radiator will have a frequency dependent index of refraction, $n_{rad}(\nu)$. The detection plane is separated from the radiator by a set of two refractive media $i = 1$ denotes quartz exit window, $i = 2$ denotes methane gas volume) each having a thickness d_i and frequency dependent index of refractions, $n_i(\nu)$. The refractive boundaries are assumed planar and lie parallel to the radiator. The detection plane lies a distance $d_{rad} + \sum d_i$ from the tracks entry point in the radiator. The analytical solution is discussed in the following sections.

4.3.1 Cherenkov Fiducial Area Determination

Tracks passing through the radiator will be characterized by a momentum vector, $\overrightarrow{p}$ making an incident polar angle, θ_{inc} with the normal to the radiator

$$\theta_{inc} = \arccos \frac{p_z}{|\overrightarrow{p}|} \tag{4.4}$$

and an incident azimuthal angle, ϕ_{inc} with a reference axis (here the x axis, see Figure 4.14)

$$\phi_{inc} = \arctan \frac{p_y}{p_x}. \tag{4.5}$$

A mass hypothesis yields for the track a velocity βc to be used in calculating the opening angle

$$\beta = \frac{|\overrightarrow{p}|}{\sqrt{|\overrightarrow{p}|^2 + m^2}} \tag{4.6}$$

of the Cherenkov light cone. The Cherenkov opening angle, θ_{Cher} depends on β and

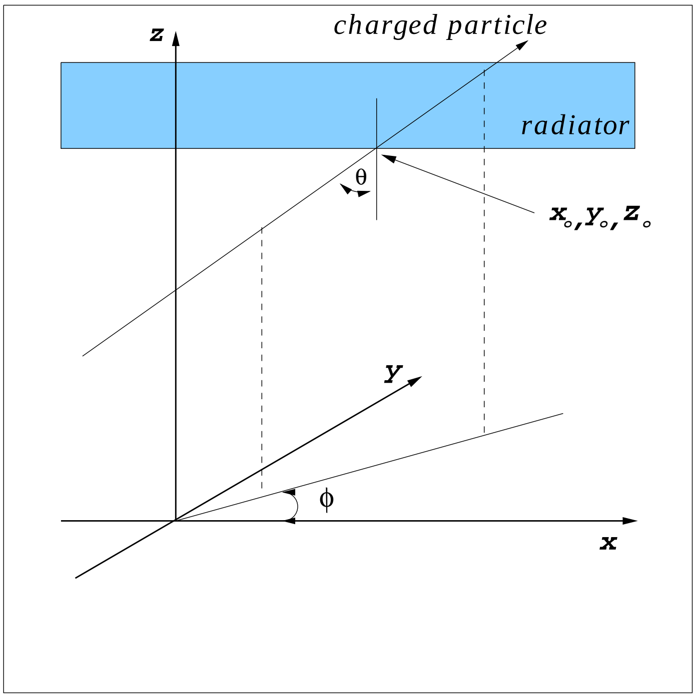

Figure 4.14: Definition of coordinate system used in deriving analytical solution for Cherenkov Fiducial area.

$n_{rad}(\nu)$ and is given by eq. 4.7 shown here

$$\theta_{Cher} = \arccos \frac{1}{n_{rad}(\nu)\beta}. \tag{4.7}$$

The Cherenkov radiation is emitted in a continuous spectrum and this results in a small spread in the possible Cherenkov opening angle of approximately 1 degree, as can be seen by the frequency dependence of $n_{rad}(\nu)$. This frequency dependence, along with the radiator's finite thickness necessitates calculating two cones of light. The first cone is generated at the particle's entry point in the radiator assuming a frequency yielding the largest Cherenkov angle eq. 4.7, and the second cone is generated at the exit point assuming a frequency yielding the smallest possible Cherenkov angle. The two cones are propagated to the pad plane where they define a fiducial area containing all the light produced by the particle in the radiator. The RICH detector geometry and refractive indices together with the track's incident angles, θ_{inc} and ϕ_{inc}, hypothetical Cherenkov angle θ_{Cher} and the tracks entry point into the radiator (x_0, y_0, z_0) are sufficient information to determine the solution. It is assumed that the track's momentum is great enough to ignore any curvature of the track's trajectory within the radiator.

Generation of Light Cone

The equation describing a family of vectors lying on the surface of a cone with an opening angle θ_{Cher} and whose apex is located at the origin is given by

$$\left(\frac{x}{a}\right)^2 + \left(\frac{y}{a}\right)^2 - \left(\frac{z}{c}\right)^2 = 0. \qquad x, y, z > 0 \tag{4.8}$$

The vectors have the origin as a common point, and eventually terminate at the lip of the cone (see Figure 4.15). The ratio $\frac{a}{c}$ is determined by θ_{Cher} and is given by,

$$\frac{a}{c} = \tan \theta_{Cher}. \tag{4.9}$$

Considering a cone of unit height ($z = 1$) then establishes a relationship between x and y,

$$x^2 + y^2 = \left(\frac{a}{c}\right)^2. \tag{4.10}$$

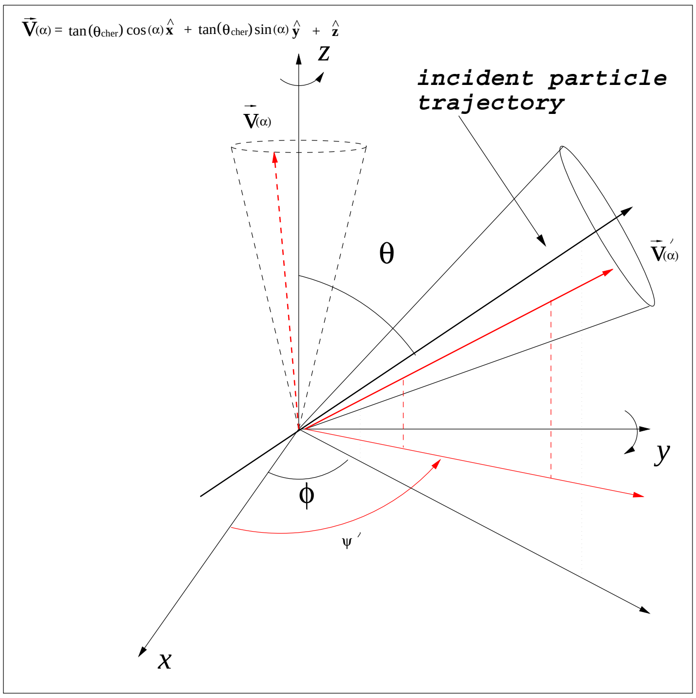

Figure 4.15: Diagram showing original light cone and rotated light cone

The single parameter ψ will be introduced to describe x, which then determines y,

$$y(\psi) = \frac{a}{c}\sin\psi, \qquad x(\psi) = \frac{a}{c}\cos\psi, \qquad\qquad 0 < \psi < 2\pi. \tag{4.11}$$

Thus the family of vectors lying on the surface of the cone can be described by a single parameter, ψ. This parameter can be interpreted as the Cherenkov photon's azimuthal angle that it makes on the cone. The cone will represent the Cherenkov cone of light generated by the charged particle traversing the radiator. However, this cone's major axis does not lie along the particle's trajectory and must be rotated such that the cone's major axis coincides with the particle's trajectory.

Rotation of Light Cone

Rotation of the cone (see Figure 4.15) is accomplished using a rotation matrix, $\mathrm{R}(\theta_{inc}, \phi_{inc})$. The rotation matrix $\mathrm{R}(\theta_{inc}, \phi_{inc})$ is obtained by first rotating about the y axis by an angle θ_{inc} followed by a rotation about the z axis by an angle ϕ_{inc}, and is given by:

$$R(\theta_{inc}, \phi_{inc}) = \begin{pmatrix} \cos\theta_{inc}\cos\phi_{inc} & -\sin\phi_{inc} & \sin\theta_{inc}\cos\phi_{inc} \\ \cos\theta_{inc}\sin\phi_{inc} & \cos\phi_{inc} & \sin\theta_{inc}\sin\phi_{inc} \\ -\sin\theta_{inc} & 0 & \cos\theta_{inc} \end{pmatrix} \tag{4.12}$$

Thus the vectors lying on the surface of the rotated cone can be obtained from the following equation,

$$\begin{pmatrix} x' \\ y' \\ z' \end{pmatrix} = \begin{pmatrix} \cos\theta_{inc}\cos\phi_{inc} & -\sin\phi_{inc} & \sin\theta_{inc}\cos\phi_{inc} \\ \cos\theta_{inc}\sin\phi_{inc} & \cos\phi_{inc} & \sin\theta_{inc}\sin\phi_{inc} \\ -\sin\theta_{inc} & 0 & \cos\theta_{inc} \end{pmatrix} \begin{pmatrix} x \\ y \\ z \end{pmatrix}. \tag{4.13}$$

Refraction of Light Cone

The family of vectors given by eq. 4.13 enable the calculation of the angle the rotated light cone makes with a planar surface parallel with the radiator. The angle θ the light cone makes with this planar surface of course depends on the charged particles incident θ_{inc} and ϕ_{inc} angles, θ_{Cher}, as well as the parameter ψ, and is given by eq. 4.14

$$\theta(\theta_{inc}, \phi_{inc}, \psi, \theta_{Cher}) = \vartheta = \arccos\left(\frac{z'}{\sqrt{x'^2 + y'^2 + z'^2}}\right). \tag{4.14}$$

The Cherenkov radiation produced in the radiator will propagate in the directions described by eq.'s 4.13 up to the first refractive boundary as pictured in Figure 4.16. This refractive boundary is characterized by the ratio $\frac{n_{rad}(\nu)}{n_1(\nu)}$ which determines in part the angle of refraction, $\theta_1^{refraction}(n_{rad}(\nu), n_1(\nu), \vartheta)$ given below

$$\theta_1^{refraction}(n_{rad}(\nu), n_1(\nu), \vartheta) = \arcsin\left(\frac{n_{rad}(\nu)}{n_1(\nu)}\sin\vartheta\right). \tag{4.15}$$

$\theta_1^{refraction}$ will in general be a complex number, the imaginary part of which indicating any internal reflection that might take place at the refractive boundary. The angle of refraction at any refractive boundary $\theta_j^{refraction}(n_{j-1}(\nu), n_j(\nu), \vartheta)$ is in general

$$\theta_j^{refraction}(n_{j-1}(\nu), n_j(\nu), \theta_{j-1}^{refraction}) = \arcsin\left(\frac{n_{j-1}(\nu)}{n_j(\nu)}\sin\theta_{j-1}^{refraction}\right). \tag{4.16}$$

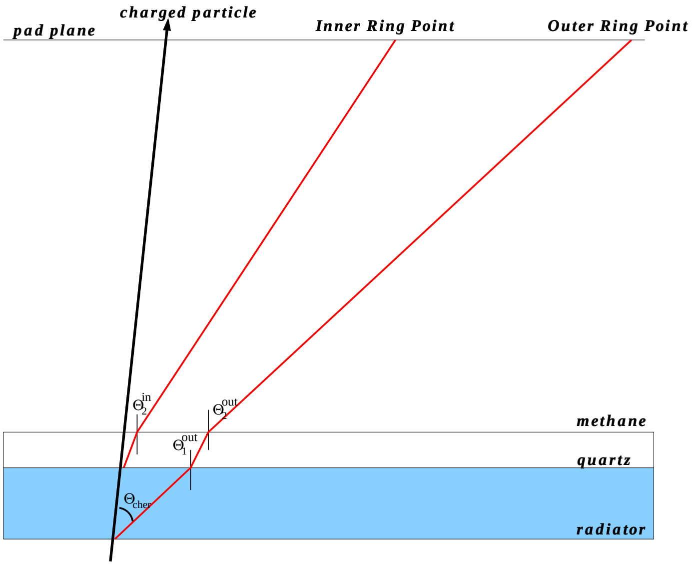

Figure 4.16: Diagram depicting path of Cherenkov Light in RICH detector

Propagation of Light Cone

The determination of the Cherenkov light cone's fiducial area on the detection plane is made by propagating two light cones to the detection plane. The charged particle has no preferred emission point in the radiator, and as such Cherenkov light can be generated at both the entry and exit points of the track in the radiator. This makes it necessary to construct two light cones and then propagate the cones to the pad plane. The cone generated at the track's exit point in the radiator will describe an inner ring on the pad plane and the cone generated at the tracks entry point in the radiator will result in an outer ring, the area bounded by the two rings defining the fiducial area (see Figure 4.17). The frequency dependence of the Cherenkov angle, eq. 4.7, requires using different frequencies in determining the Cherenkov angle to be used in the construction of the inner and outer cones. The cone resulting in the inner ring on the pad plane is described using the Cherenkov angle determined by the low frequency part of the Cherenkov radiation spectrum (i.e. $\lambda = 220\ nm$) yielding the smallest Cherenkov angle, and the cone resulting in the outer ring on the pad plane is described using the Cherenkov angle determined by the high frequency part of the Cherenkov radiation spectrum (i.e. $\lambda = 170\ nm$) which gives the largest possible

Cherenkov angle. The equations describing the inner ring are shown below,

$$\begin{aligned} x_{inner} - x_0 &= d_{rad} \tan\theta_{inc} \cos\phi_{inc} + \sum d_i \cos\psi' \tan\theta_i^{refraction} \\ y_{inner} - y_0 &= d_{rad} \tan\theta_{inc} \sin\phi_{inc} + \sum d_i \sin\psi' \tan\theta_i^{refraction}. \end{aligned} \tag{4.17}$$

The parameter ψ is now modified due to the rotation of the light cone and is shown below,

$$\psi' = \arctan\frac{y'}{x'}. \tag{4.18}$$

The equations describing the outer ring, are similar to those of the inner ring,

$$\begin{aligned} x_{outer} - x_0 &= d_{rad} \tan\vartheta \cos\psi' + \sum d_i \cos\psi' \tan\theta_i^{refraction} \\ y_{outer} - y_0 &= d_{rad} \tan\vartheta \sin\psi' + \sum d_i \sin\psi' \tan\theta_i^{refraction}. \end{aligned} \tag{4.19}$$

The $\psi\prime$ parameter can range from $-\pi$ to π and is defined in a reference frame relative to the particle's momentum vector projected onto the pad plane. Thus values of $|\psi\prime|$ close to zero lie near the forward region of the Cherenkov Fiducial area (the 'fat' region pointed to by the projected momentum vector in the Figure 4.17). Values of $|\psi\prime| \lesssim \pi$ lie in the back region of the Cherenkov Fiducial area. A necessary condition is $\Im x = 0$ and $\Im y = 0$. An imaginary component not equal to 0 indicates that internal

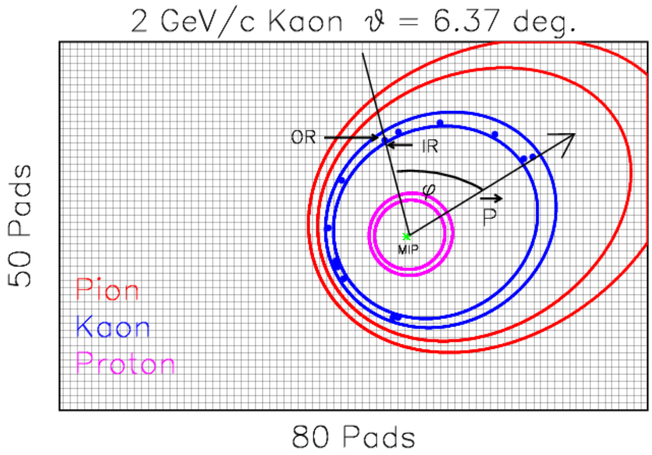

Figure 4.17: Example of Cherenkov Fiducial Area on RICH Pad Plane for a simulated charged Kaon intersecting the RICH radiator with a polar angle of 6° and having a momentum of 2 GeV/c.

reflection has taken place at a boundary interface, and thus no Cherenkov light can reach the detection plane.

4.3.2 Cherenkov Fiducial Area Properties

Equations 4.17, 4.19 describe the Cherenkov Fiducial area on the RICH detection plane for particles striking the RICH with arbitrary momenta and polar angles less than ninety degrees. It is instructive to first consider Cherenkov Fiducial areas for particles striking the RICH at normal incidence. In this case, the Cherenkov pattern produced on the RICH pad plane is circular and has a radius directly proportional to the mean Cherenkov angle of the photons emitted by the particle in the RICH radiator. The particular index of refraction values used for the various refractive materials will be discussed in the next section. The radii for the predicted Cherenkov Fiducial areas are shown in Figure 4.18. The radius for both the inner and outer boundaries are shown for the three different particle species, with the π radii having the largest values of $\sim$ 12 cm at saturation. The difference in the inner and outer radii is partly due to the small difference in Cherenkov emission angles brought about as a result of the dispersion of the liquid radiator. The finite depth of the radiator, (1 cm), contributes to the difference as well. The width of a saturated ring at normal incidence is $\sim$ 2 cm, with the dispersion and radiator depth contributing in roughly equal parts. The rather large width of a saturated ring compares favorably to the residual

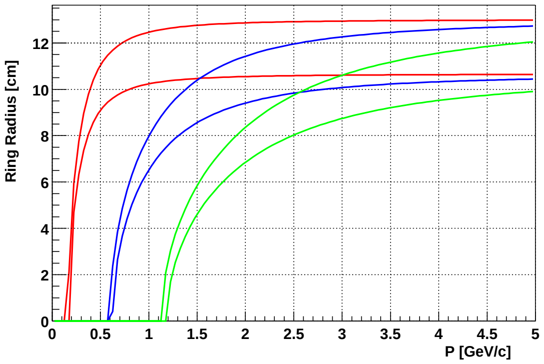

Figure 4.18: Cherenkov Fiducial widths.

offset corrections discussed in the previous section. The area contained within the Cherenkov Fiducial area is $\sim 120\ cm^2$ for a normally incident particle at saturation.

An example of the Cherenkov Fiducial area for a normally incident particle at saturation is shown in Figure 4.19. However, the phase space for particles striking the RICH at normal incidence is very small, making necessary the inclusion of tracks striking the RICH at non-normal angles. The Cherenkov Fiducial areas expected for particles intersecting the RICH radiator at non-normal angles produce patterns on the pad plane which are not circular, (Figures 4.21 and 4.23 are examples for tracks at 10° and 25° respectively). The pattern calculated for a track making a polar angle of 10° with respect to the RICH radiator is plotted in Figure 4.21. The azimuthal angle made by the track is zero degrees in this example and in this coordinate system corresponds to a particle moving from left to right in the Figure. The Cherenkov Fiducial area contained on the RICH pad plane is now larger than for the case of normal incidence. The forward section of the Cherenkov Fiducial area is now much larger than in the normal incidence case and is the result of the non-linear nature of the bending of the light at the refractive boundaries, most notably the quartz exit window and methane gas boundary. Figure 4.20 depicts the path followed by

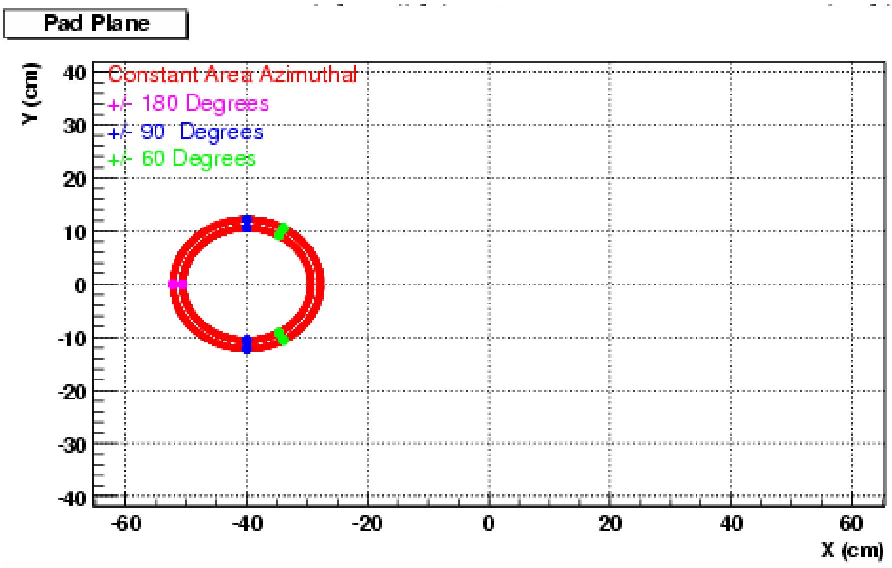

Figure 4.19: Example for track at normal incidence

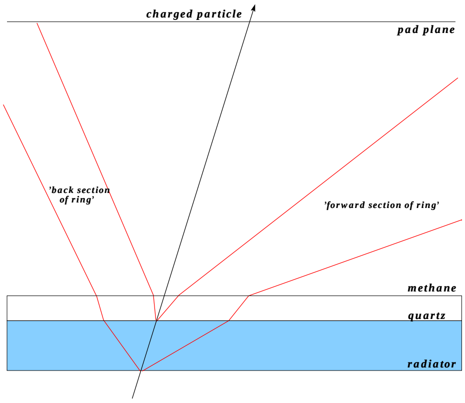

Figure 4.20: Path of Cherenkov light.

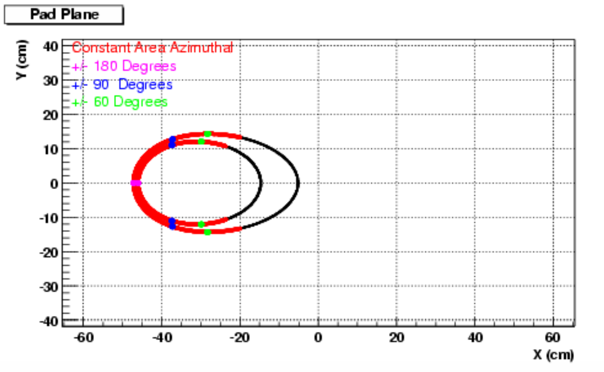

Figure 4.21: Example of track at 10°.

Cherenkov photons lying on the inner and outer Cherenkov cones described by eq. 4.8. The angles made by the light rays at the refractive boundaries are much larger in the forward region of the light cones than in the back region. Thus the predicted region on the pad plane has a complicated shape with a strong dependence on both the particle's angle of incidence made at the RICH radiator as well as $\psi\prime$, the parameter describing the position along the ring. Figure 4.22 shows an example of the pathways followed by the Cherenkov light cones emitted in the RICH radiator for a track having a large angle of inclination, ($\sim 25°$), relative to the RICH radiator. In this example, the light rays defining the forward region of the light cones have suffered total internal reflection at the quartz-methane interface. Thus the Cherenkov light emitted in the

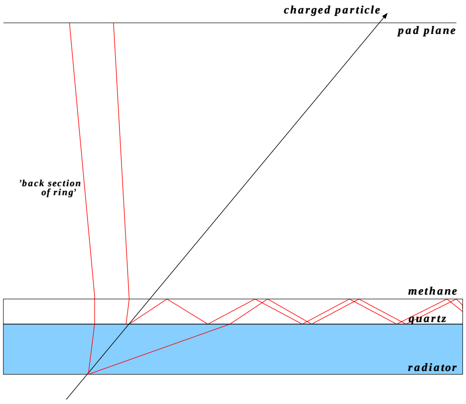

Figure 4.22: Path of Cherenkov light.

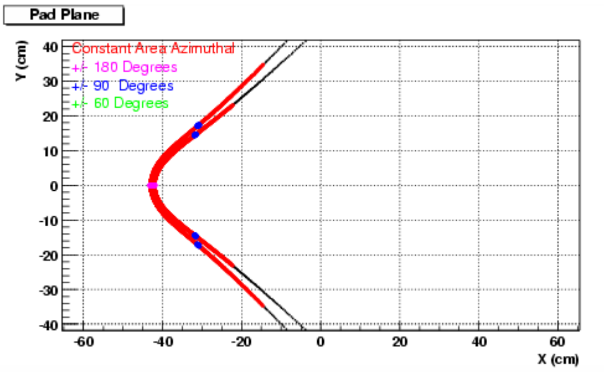

Figure 4.23: Example of track at 25°.

forward direction is trapped in the quartz exit window and cannot reach the pad plane. A similar fate can occur for light striking the radiator-quartz boundary at angles greater than the critical angle, thus trapping the light in the radiator. A track striking the RICH radiator at a highly inclined angle thus has a predicted Cherenkov Fiducial area on the pad plane which is no longer circular, but rather the shape of a hyperbola, as shown in Figure 4.23. The critical angle for light striking the quartz-methane boundary can be calculated for the inner and outer cones separately using Snell's law,

$$\theta_{critical} = \arcsin \frac{n_{methane}}{n_{quartz}}. \tag{4.20}$$

The inner and outer Cherenkov light cones are calculated using slightly different index of refraction values for the liquid radiator and quartz to account for dispersion and have critical angles $\theta_{in} \sim 42.3^\circ$ and $\theta_{out} \sim 40.8^\circ$. Similar calculations yield critical angles for the liquid radiator-quartz exit window boundary of $\theta_{in} \sim 59.17^\circ$ and $\theta_{out} \sim 58.2^\circ$.

EXAMPLE: A charged particle striking the RICH radiator at an angle of 14° *produces a Cherenkov cone of light having a mean opening angle* $\sim 38^\circ$ *at saturation. Since the particle is inclined* 14° *relative to the quartz exit window, the forward portion of the light cone strikes the radiator-quartz boundary at an angle* $\sim 52^\circ$*. Snell's law then gives an angle of* $\sim 42^\circ$ *in the quartz window. This is an angle greater then the quartz-methane critical angle (*$\sim 40 - 42^\circ$*) and thus the forward portion of the Cherenkov light cone is trapped in the quartz window.*

Particles striking the RICH radiator at angles greater than $\sim 10^\circ$ thus have predicted Cherenkov Fiducial areas covering large amounts of area in the forward section of the ring. The Cherenkov light produced in the RICH radiator is emitted in an azimuthally symmetric way. However, because of the various refractive materials present in the construction of the detector, the azimuthal distribution of the Cherenkov photons on the pad plane for particles having non-normal angles of inclination (i.e. all the particles!) will not be symmetric. The forward region of the Cherenkov Fiducial area will have fewer Cherenkov photons per unit area than other regions of the ring.

In addition to this, the background photons on the pad plane are distributed in an approximately random fashion and should scale with area. Thus the forward region of the Cherenkov Fiducial area for tracks having angles of inclination greater than $\sim 10^\circ$ will have fewer signal photons per unit area and have a much larger number of background photons present. To increase the total signal-to-background ratio, a method was developed to truncate the Cherenkov Fiducial area. Photons found within the forward section of the Cherenkov Fiducial area are likely to be background and thus a cut is placed on these photons.

One way to remove the forward region of the Cherenkov Fiducial area is to make a constant cut in the $\psi\prime$ parameter, independent of the particles momentum, angle of inclination, or mass. The $\psi\prime$ parameter describes the azimuthal distribution of points along the inner and outer rings and thus placing a cut on small $|\psi\prime|$ ($< 30^\circ$ for example) would remove the forward section of the Cherenkov Fiducial areas. This is inefficient though, as the predicted Cherenkov Fiducial area has a non-linear dependence on the particle's momentum, angle of inclination, mass and $\psi\prime$. A constant cut applied to all Cherenkov Fiducial areas would over-compensate in some cases, and under-compensate in others. Thus, it is more efficient to introduce a dynamic cut in the Cherenkov Fiducial area's $\psi\prime$ parameter. This is done by demanding the Cherenkov Fiducial area to be limited to the area for a normally incident particle of the same mass and momentum. The area bounded by the inner and outer rings defining the predicted Cherenkov Fiducial area can be calculated via numerical methods. The calculation starts by integrating the area bounded by the two curves defined by eq.'s 4.17 and 4.19 from $\psi\prime = 0$ up to $\psi\prime = \pi$. The calculation is halted when the area is one-half the total area of a normally incident ring. The value of $\psi\prime$ at this point is then used to cut away the forward, or 'fat', portion of the Cherenkov Fiducial area for each of the hypothetical masses on a track-by-track basis. Figures 4.21 and 4.23 show calculations of the saturated Cherenkov Fiducial area for tracks with angles of inclination of 10° and 25° respectively. The Cherenkov Fiducial area is shown in black, with the portion having an integrated area less than the area of a normally incident ring high-lighted in red. Figure 4.24 shows the total integrated angle, Ω_{total}, for the Cherenkov Fiducial area for a 3 GeV/c π as a function of the track's angle of inclination. The black curve is the total angle contained within the ring and is

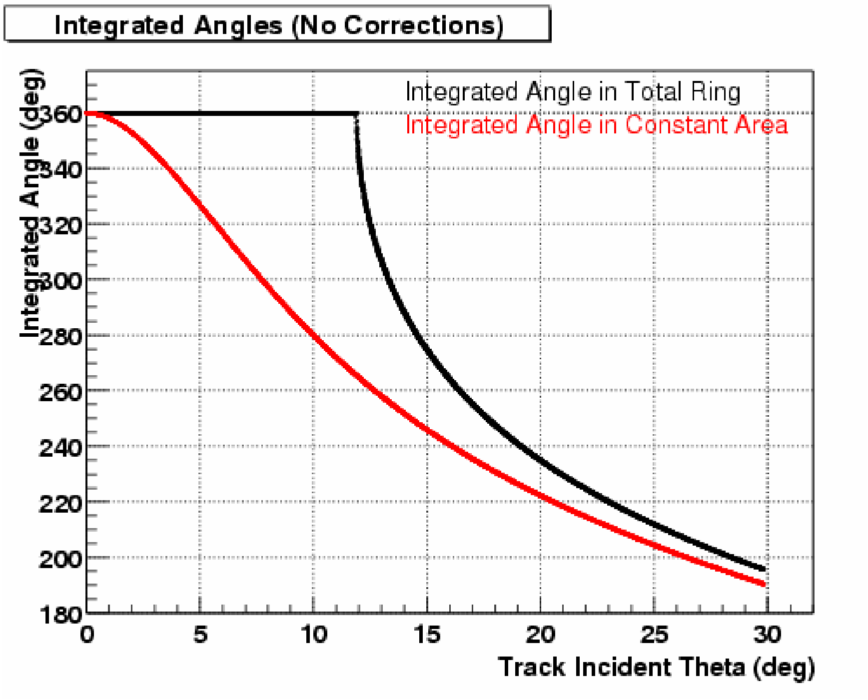

Figure 4.24: Constant Area Angle Cut

flat with a value of 360° (as expected) up to an angle of inclination $\sim 13°$. The Cherenkov light cone is partially trapped in the quartz exit window for angles of inclination greater than this and the total integrated angle of the Cherenkov Fiducial area shows a strong dependence on the angle of inclination. The red curve is the total integrated $\psi\prime$ angle, $\Omega_{constant\,area}$, for the portion of the ring having an area equal to the area of a normally incident π at the same momentum. The value for the $\psi\prime$ cut-off can be obtained from $\Omega_{constant\,area}$,

$$\begin{aligned} \psi\prime_{cut-off} &= (\Omega_{constant\,area} - 360°)/2. && 0 < \psi\prime < \pi \\ \psi\prime_{cut-off} &= -(\Omega_{constant\,area} - 360°)/2. && -\pi < \psi\prime < 0. \end{aligned} \tag{4.21}$$

4.4 Pattern Recognition

Examples of the predicted Cherenkov Fiducial areas on the RICH detection plane are shown in Figure 4.25 using a real event from the first year of data taking at STAR. The RICH detection plane is divided into four separate quadrants as indicated by the outlines in black. The individual pads are shown with a color indicating the amount of charge collected by each pad in adc units. A color bar on the right of the detection plane shows how much charge is to be associated to each color, red indicating high amounts of charge collected and then trending downwards to blue for small amounts of collected charge. Groups of pads (clusters) are seen on the pad plane with black crosses superimposed indicating the mean position of the cluster and are obtained from the cluster finding algorithm explained in the above section. Particles tracked by the TPC and which point to the RICH have their calculated intersection points with the RICH detection plane shown as purple diamonds. In the example shown, all tracks having a transverse momentum above 1 GeV/c have their predicted Cherenkov fiducial areas overlaid on top of the pad plane. The predicted π fiducial area has the smallest amount of curvature and is shown in red. The predicted K fiducial area is shown in black, and the p area is shown in green.

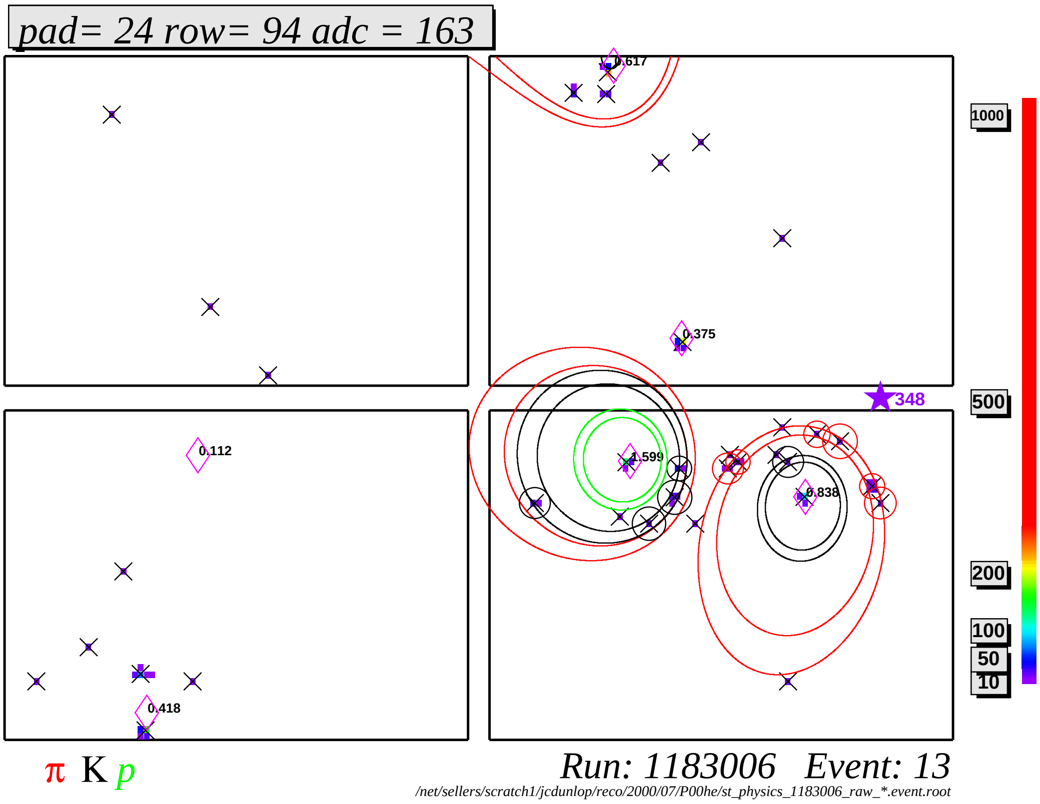

Figure 4.25: Example of RICH pad plane display

4.4.1 Parameters used in Pattern Recognition

The equations 4.17,4.19 describing the predicted Cherenkov fiducial area depend on a number of variables: the magnitude of the particle's momentum, the polar and azimuthal angles made at the radiator ($\overrightarrow{p}$), the particle's intersection point at the radiator ($\overrightarrow{x}$), a hypothetical mass, geometrical factors and index of refraction for the transparent materials in the detector. The $\overrightarrow{p}$ and $\overrightarrow{x}$ parameters are obtained from the TPC tracking, and the parameters describing the detector were determined prior to installation. All of the parameters describing the detector have singular values, except for the index of refraction for the liquid radiator and quartz exit window. This necessarily entails choosing a set of parameters which best describe the Cherenkov pattern produced on the RICH pad plane. The index of refraction for the various materials are shown in the section describing the RICH detector and are shown here again for clarity, (Figures 4.26, 4.27). The C_6F_{14} liquid has values ranging

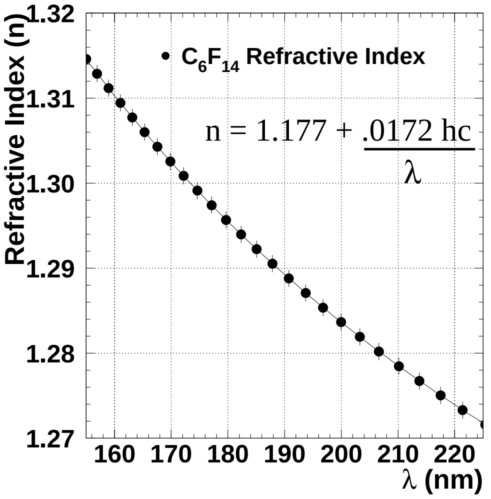

Figure 4.26: Freon Refractive Index. Figure obtained from ref. [1].

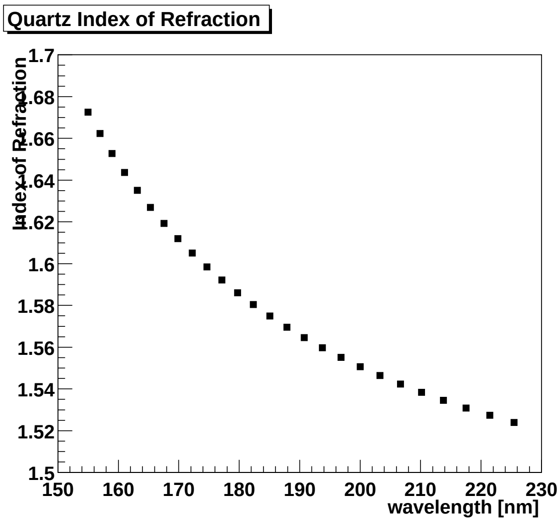

Figure 4.27: Quartz Refractive Index. See ref. [4] for details.

from $n_{C_6F_{14}} \sim 1.29$ for wavelength's near 160 nm down to $n_{C_6F_{14}} \sim 1.27$ for wavelength's near 220 nm. The quartz has larger values for its index of refraction, ranging from $n_{quartz} \sim 1.64$ at 160 nm down to $n_{quartz} \sim 1.53$ for a wavelength of 220 nm. The methane gas has a constant index of refraction in the above wavelength region, $n_{methane} \sim 1$.

To determine which values to use in the calculations of the inner and outer boundaries of the Cherenkov fiducial areas, the index of refraction curve for the liquid radiator (Figure 4.26) has to be used in conjunction with the absorption curves and the CsI response curve (Figure 4.28). The amount of light generated in the radiator for a particle above the Cherenkov velocity threshold is dependent on the index of refraction of the liquid as shown in equation 2.7, and is shown here again for clarity

$$\frac{dN}{dx} = k(\lambda) \int \frac{1}{1 - n^2(\lambda)\beta^2} \frac{d\lambda}{\lambda} \tag{4.22}$$

Figure 4.28[1] shows the curve representing the amount of light generated in the radiator by the passage of a charged particle travelling with a velocity above the

Cherenkov threshold. The relative amount of light generated is plotted along the ordinate and the wavelength is shown on the abscissa. Shown in the same Figure in the solid circles is the effect of absorption of the Cherenkov radiation as it travels through the liquid radiator, quartz exit window, and methane gas. The strong cut-off in the quartz absorption spectrum is mainly responsible for the strong dependence on wavelength near 160 - 180 nm. The effect of the photo-converter's quantum efficiency is also shown in the same plot as the solid triangles. The resulting curve is then used as a starting point to determine the wavelength's for the inner and outer boundaries of the Cherenkov fiducial area calculations, equations 4.17,4.19. The wavelength used for the inner boundary is then found somewhere near the far tail of the curve shown in solid triangles, $\gtrsim$ 200 nm. The outer boundary is determined using a wavelength $\lesssim$ 180 nm. The exact values used to describe the inner and outer boundaries of the

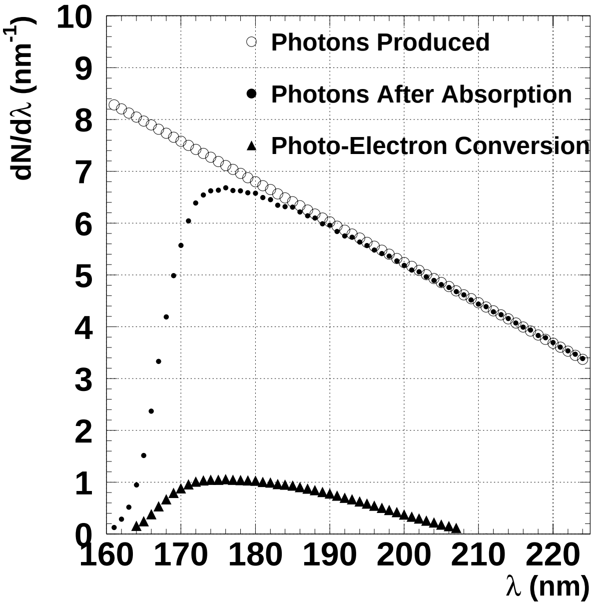

Figure 4.28: Open circles show the amount of light generated in the radiator by a charged particle above threshold. The effect of absorption in the liquid and quartz is shown in the same plot with closed circles. The amount of light reaching the pad plane and yielding photon electrons is shown using triangles. [1]

Cherenkov fiducial area were chosen to be 174.633 nm for the outer boundary and 217.039 nm for the inner boundary. These values were obtained using Figure 4.28 as a starting point, and then in an iterative fashion selecting a set of values which best describe the predicted Cherenkov pattern on the RICH pad plane. The iterative method uses variables defined and described in the next section.

4.4.2 Characterization of Charge Clusters using Pattern Recognition

The photon clusters on the RICH pad plane can be assigned a set of numbers describing the position, d, and orientation, ψ, of the photon cluster relative to the expected Cherenkov pattern for a given hypothetical particle mass, (π, K, P). Figure 4.29 shows the calculated Cherenkov Fiducial areas using equations 4.17,4.19 for a hypothetical particle striking the RICH radiator at a polar angle of $\sim$ 6 degrees and having a momentum of 2 GeV/c. The π Cherenkov Fiducial area has the largest radius and area, as expected from its relatively small mass. The K has a smaller radius

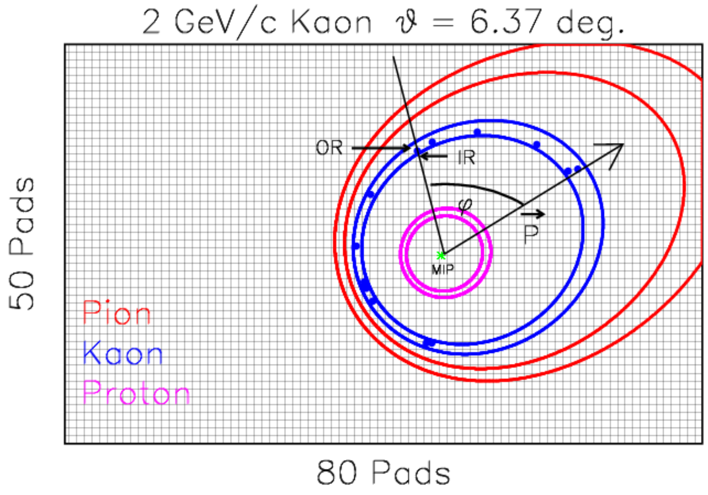

Figure 4.29: Simulated response of a charged kaon travelling through the RICH detector. One quadrant of the RICH pad plane is shown together with the location of the simulated Cherenkov photons generated by the passage of the charged kaon. The predicted Cherenkov Fiducial Areas for π, K, and P are shown as well.

and area than the π and is indicated in the plot by the blue curve. The predicted P Cherenkov Fiducial area is the smallest and is shown in purple. The equations describing the Cherenkov Fiducial areas (eq. 4.17, 4.19), are completely specified by the measured properties of the particle's trajectory in the TPC, geometrical factors, and a hypothetical mass. The $\psi\prime$ variable is a free parameter having values ranging from $-\pi$ to π and specifies a unique position along the inner or outer boundary. The $\psi\prime$ parameter is calculated relative to the particle's momentum vector projected onto the pad plane as shown in Figure 4.29. Every reconstructed photon cluster can be assigned a value for $\psi\prime$ using a minimization routine which determines the location of the photon relative to the calculated Cherenkov Fiducial area. The equations 4.17 and 4.19 for the inner and outer boundaries are non-linear in $\psi\prime$ and for a given $\psi\prime$ can have vastly different positions on the pad plane for Cherenkov Fiducial areas calculated for tracks having large (> 10 degrees) polar angles. Thus photons are localized by minimizing the angle made relative to a reference line defined by the inner and outer ring point at the same $\psi\prime$. The determination of $\psi\prime$ for a reconstructed photon cluster then can be used to calculate the distance of the photon from the predicted Cherenkov Fiducial area using equations 4.17 and 4.19. The position of a reconstructed photon cluster relative to what is expected from the prediction is determined in the following manner. The inner and outer ring points will be denoted with $\overrightarrow{i}$ and $\overrightarrow{o}$, respectively. The distance of the photon, $\overrightarrow{p}$, from the inner boundary, (determined using the reconstructed photon clusters calculated $\psi\prime$) is normalized to the local width of the ring, $|\overrightarrow{i}$ - $\overrightarrow{o}|$, which then describes a photon's normalized distance d from the Cherenkov Fiducial area

$$d = \frac{|\overrightarrow{p} - \overrightarrow{i}|}{|\overrightarrow{i} - \overrightarrow{o}|}. \tag{4.23}$$

Figure 4.30 shows the normalized distance distribution made for reconstructed photon clusters in a given event relative to the predicted π Cherenkov Fiducial area predicted for each track in the same event. The distribution shown was made using tracks having transverse momenta $1.25 < p_{\perp}[GeV/c] < 1.5$ selected from $\sim$ 150K events. Values for the normalized distance d_{π} close to 0 represent photon clusters lying near the inner boundary, and d_{π} values close to 1 indicate the photon lies near the outer

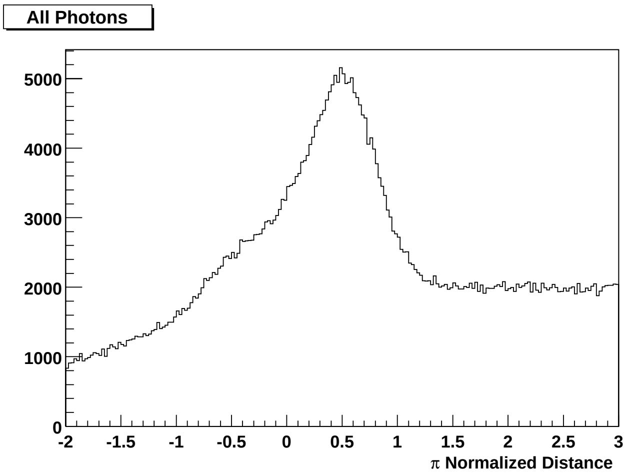

Figure 4.30: d distribution of photon clusters relative to π Cherenkov Fiducial area.

boundary of the π Cherenkov Fiducial area. Thus the large peak centered near $d_\pi \sim 0.5$ is composed of photons which fall within the Cherenkov Fiducial area predicted for the π. A relatively slowly varying background is present on either side of the π peak. This plot of the normalized distance variable d is calculated for every photon on the pad plane using all of the selected tracks, with the assumption that every track is a π. Separate peaks are expected to appear for the tracks in the data sample which are not π's. These peaks represent the Cherenkov photons originating from the different particle species present in the track sample and appear as peaks in the π normalized d variable because the photon distribution for these different particle species are essentially similar to the expected π distribution but lie at smaller radii. Indications of this can be seen in Figure 4.30, where an apparent peak can be made out near $d_\pi \sim$ -0.5 which would correspond to the Cherenkov photons originating from the Kaons in the track sample. The Cherenkov photons from any Protons in the track sample are expected to fall within the Proton's Cherenkov Fiducial area at a much smaller radius and will not show up in this plot.

Photon Clusters

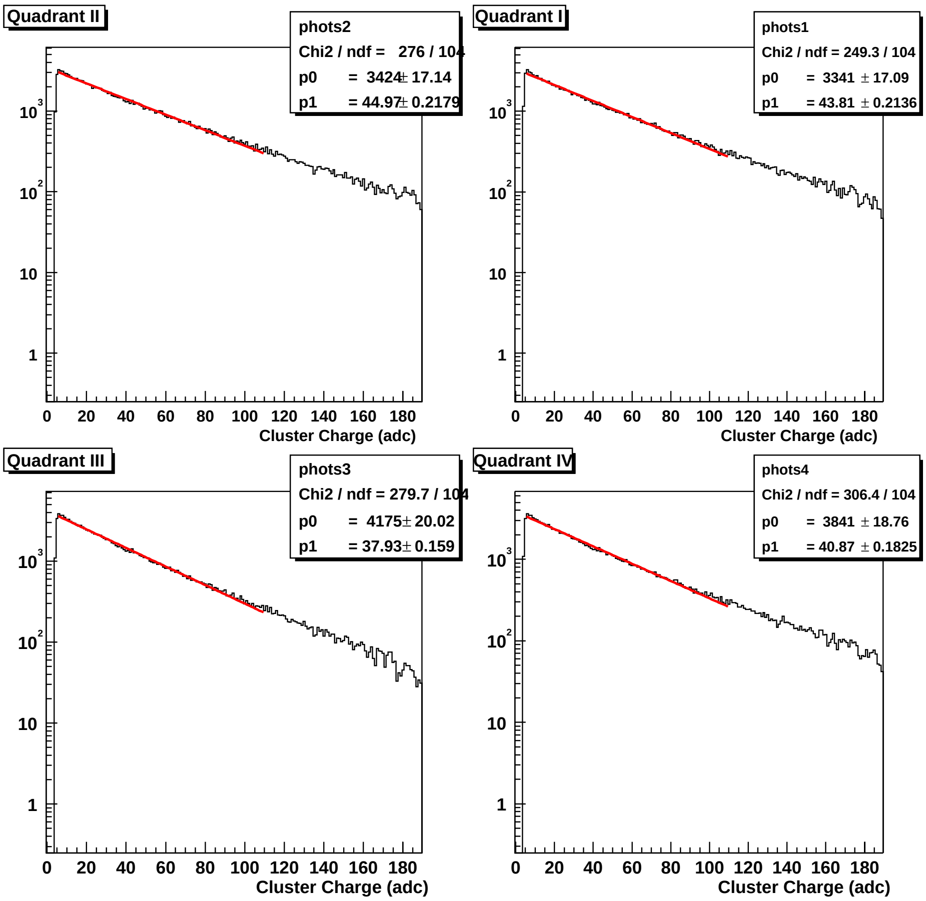

Figure 4.31: Photon cluster adc distribution

The charge clusters found within the predicted Cherenkov Fiducial areas are expected to consist mainly of charge clusters arising from the interaction of a Cherenkov photon with the CsI photo-converter covering the pad plane. The characteristics describing a photon cluster are expected to differ significantly from a charge cluster marking a charged particle's intersection with the pad plane (Mip). The Cherenkov photon will, with a maximum quantum efficiency ∼ 20% (see Figure 2.26), liberate a single electron from the RICH CsI photo-converter. The photon-electron will be accelerated up to the nearest anode wire, creating a charge avalanche in the vicinity of the anode wire. The amount of charge collected on the pads directly below the avalanche is expected to follow an exponential distribution appropriate for single electron spectra (see Reference [39] for details). The summed adc values for the charge clusters found within the predicted Cherenkov Fiducial areas are shown in Figure 4.31, with each pad plane quadrant treated separately. Shown in each sub-figure are the results of exponential fits applied to each summed adc distribution.

The mean adc value for the photon clusters in each quadrant have similar values ∼ 40 adc. This mean adc value is significantly smaller than the mean adc value for the Mip clusters, ∼ 1000 adc. This makes it possible to make a simple adc cut, quadrant by quadrant, to reduce contamination of the photon cluster distribution from Mip clusters. Plots related to those above are shown in Figure 4.32, where the number of pixels in each charge cluster found within the predicted Cherenkov Fiducial area are plotted for each quadrant separately. The size of a mean photon cluster is much smaller than the Mip clusters, approximately 1.8 pad units.

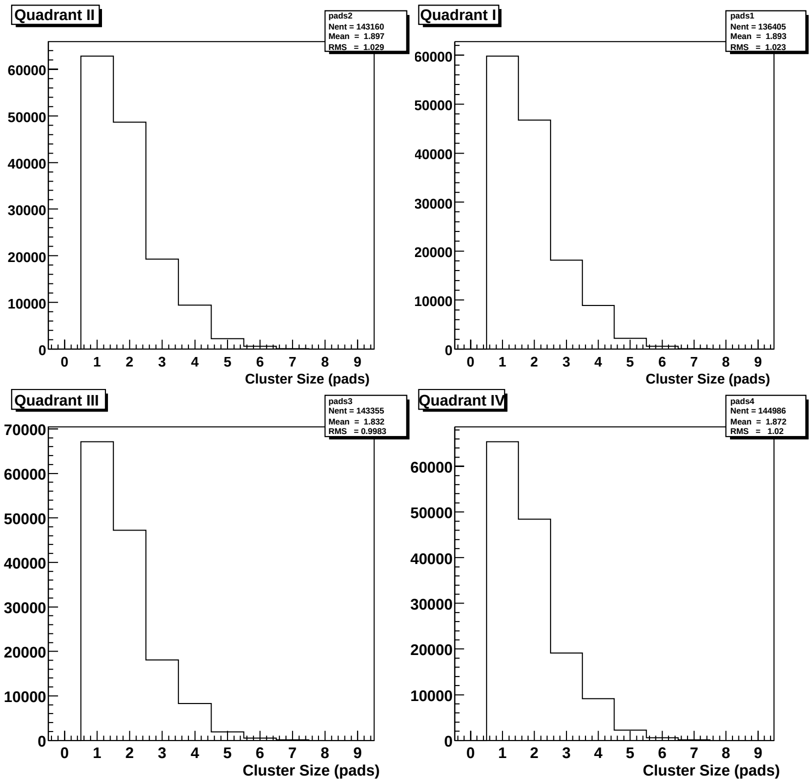

Figure 4.32: Photon cluster size distribution

Normalized Distance Distribution of Photons

The distribution of photons relative to the expected Cherenkov Fiducial area as shown in Figure 4.30 shows strong indications of a peak in the position expected for the π photons, with a somewhat weaker response in the K channel near d_π values ~ -0.5. This apparently poor resolution in the separation of the π and K (as well as P) photon peaks seen in the normalized d_π distribution can be improved by cutting away the forward section of the Cherenkov Fiducial area as discussed in the previous section.

The Cherenkov Fiducial area is narrow and well defined in the back portion of the ring, near $|\psi\prime| \sim 180^\circ$ for track's striking the RICH radiator at any angle, whereas the forward section ($|\psi\prime| \sim 0^\circ$) of the Cherenkov Fiducial area deviates strongly from the circular shape for track's having angles of inclination $\theta_{inc} \gtrsim 10^\circ$. The Cherenkov Fiducial area in the forward region is very large and is characterized by local ring widths which are much larger than what is calculated in the back portion. This rapid variation in the local ring width for tracks inclined relative to the RICH radiator results in a loss of resolution in the d_π distribution. To overcome this, a cut can be applied to remove photons found in the forward portion of the rings. The constant area angle (see Figure 4.24 and eq. 4.21) can be used to remove photons having reconstructed azimuthal angles $\gamma_{reco.photon} < \psi\prime_{cut-off}$. Figures 4.33 and 4.34 illustrate the effectiveness of the cut. The weak K peak in the d_π distribution, Figure

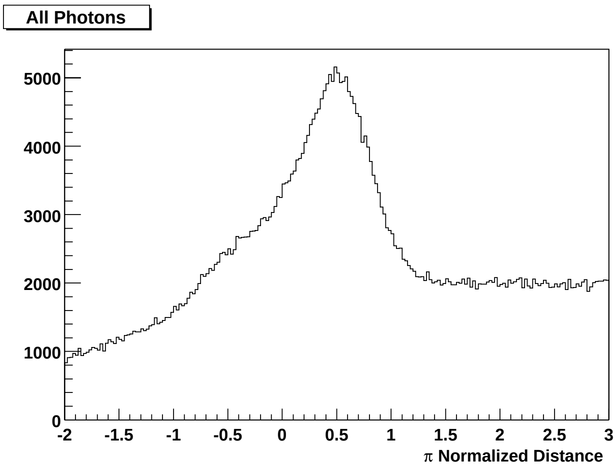

Figure 4.33: No Cuts applied.

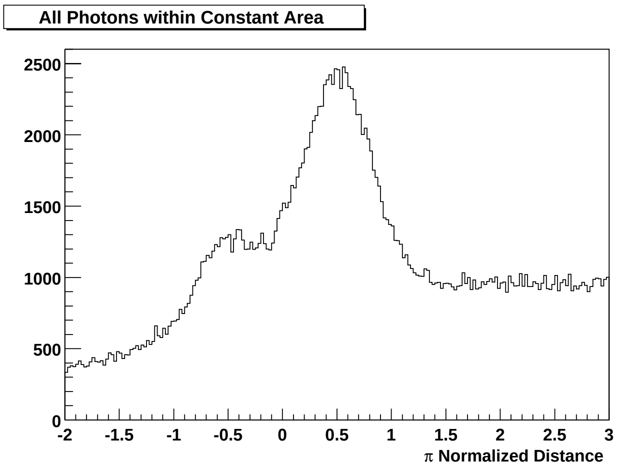

Figure 4.34: Constant Area angle cut.

4.33, is seen with much better clarity after applying the constant area angle cut, as seen in Figure 4.34.

The normalized distribution of photons found within a predicted Cherenkov Fiducial area is approximately Gaussian. Figure 4.35 shows the normalized distance distribution of photons relative to the predicted π Cherenkov Fiducial area for $\sim$ 2000 tracks within a limited range in transverse momenta, $1.49 < p_{\perp}[GeV/c] < 1.7$. The tracks contained in this sample are well above the K and P momentum thresholds, ($\sim .6$ and ~ 1.2 GeV/c) and thus it is expected (and seen) that photon peaks for the K and P should be present in the d_π distribution. The values plotted for d_π range

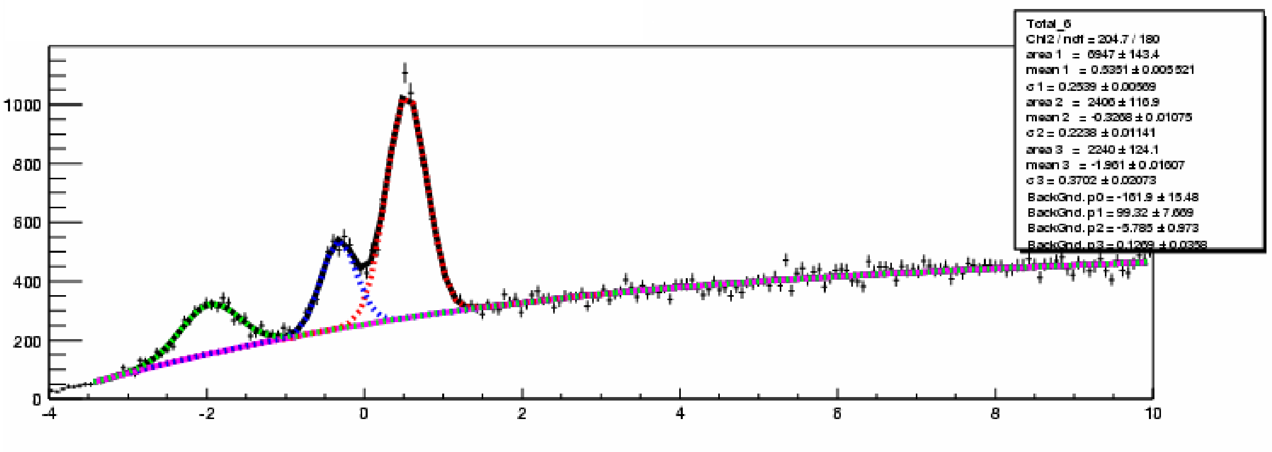

Figure 4.35: Example of normalized distance distribution of photons relative to the π Cherenkov Fiducial area for $1.49 < p_{\perp}GeV/c < 1.7$. Photons falling within the π fiducial area are highlighted in red, while photons corresponding to the K fiducial area are shown in blue, with the photons for the P in green. A cut to remove photons in the forward region of the predicted Cherenkov Fiducial area has been applied.

from a lower limit of -4 to an upper limit of 10. The lower limit corresponds to points well inside the π radius while the upper limit represents photons far removed from the outer radius of the Cherenkov Fiducial area predicted for the π. In addition to the three photon peaks present in the Figure, a smooth background is present extending over the entire range of d_π values. The background is relatively small for small values of d_π values and grows large as d_π increases in value. Large values of d_π correspond to large radii, and thus greater amounts of background are expected for large values of d_π.

The π, K and P photon peaks in Figure 4.35 have been fitted to Gaussian curves simultaneously with a third order polynomial for the background. The Gaussian fit to the π photon peak is highlighted in red, along with the K (blue) and P (green) fits. The result of the polynomial fit to the background is shown in the same figure (magenta). The mean, $\overline{d_\pi}$, and width, σ_π, of the Gaussian fit to the π photon peak is plotted vs the track's transverse momentum in Figure 4.36. The fits were performed for positive and negative tracks separately, with the blue data points representing negative tracks and red data points for the positive tracks. The Gaussian means and widths extracted from the d_π fits show similar behavior for the positive and negative tracks and are flat as a function of the track's primary $p_\perp$. The photons found within the π Cherenkov Fiducial area have a Gaussian mean ~ 0.54 and a width ~ 0.27. Similar trends are found for the means and widths when plotted against the track's angle of incidence or along the ring's $\psi\prime$ parameter.

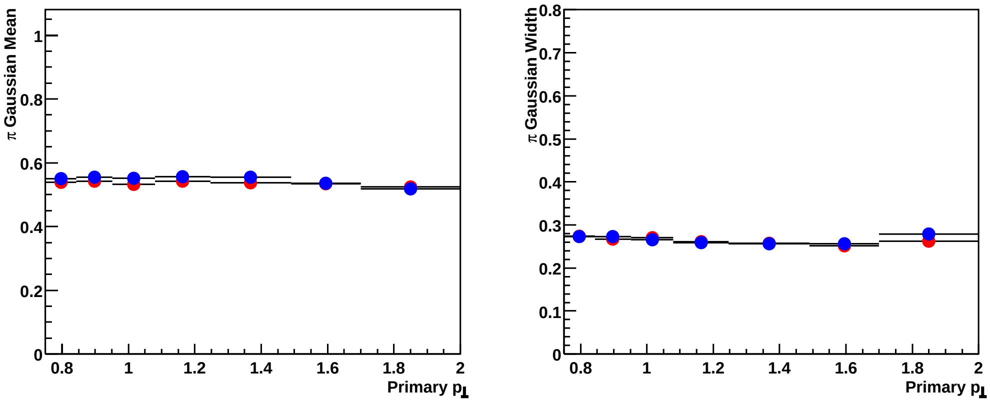

Figure 4.36: π Gaussian mean and width vs $p_\perp$

A similar analysis was done for the the distribution of photons calculated relative to the Cherenkov Fiducial area for the Kaon. Figure 4.37 shows the means and widths ($\overline{d_K}$ and σ_K) of the Kaon Gaussian fit vs the track's transverse momentum. The means describing the Kaon Cherenkov Fiducial area for the positive tracks are flat as a function of the track's $p_\perp$ with a mean value $d_K \sim 0.54$. The means for the negative tracks appear to have a slight dependence on the track's $p_\perp$, showing a $\sim$ 10% variation. The widths show similar trends for positive and negative tracks and have a dependence on the track's $p_\perp$. The Gaussian width parameter has a value $\sim$ 0.4 at $p_\perp = 0.8$ and gradually decreases to a constant value $\sim$ 0.27, similar to the π width. The Kaon widths level out and remain constant at a $p_\perp$ approximately 1.2 GeV/c which corresponds to a $\beta \sim 0.92$. Figure 4.38 details the means, $\overline{d_P}$, and widths, σ_P, for the distribution of photons calculated relative to the Proton Cherenkov Fiducial area. The dependence of the means on the track's $p_\perp$ is similar to that of the Kaons, as are the widths. The Gaussian means are flat versus $p_\perp$ for the positive tracks, but the negative tracks seem to have a dependence at small values of $p_\perp$. The Gaussian widths for the Proton Cherenkov Fiducial area have values $\sim$ 0.55 at the lowest $p_\perp = 1.4$ and level off at widths $\sim$ 0.27 at $p_\perp \sim$ 2.225 GeV/c. This corresponds to a $\beta \sim 0.92$, similar to the velocity at which the Kaon widths levelled off.

4.4.3 Photon Multiplicities

Particle ratio's can be calculated by integrating the photon yields found within the π, K and P Cherenkov Fiducial area's predicted for the different track charges. The error on the ratio determined using the number of photons is an underestimation, as

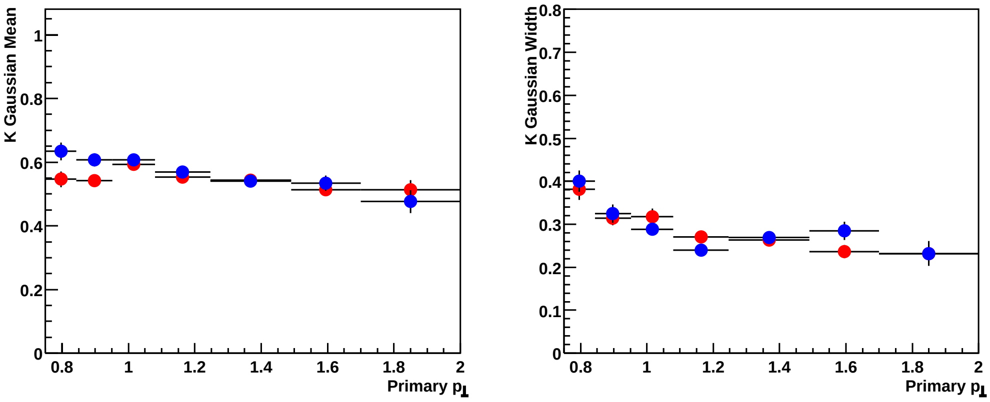

Figure 4.37: Kaon Gaussian mean and width vs $p_\perp$

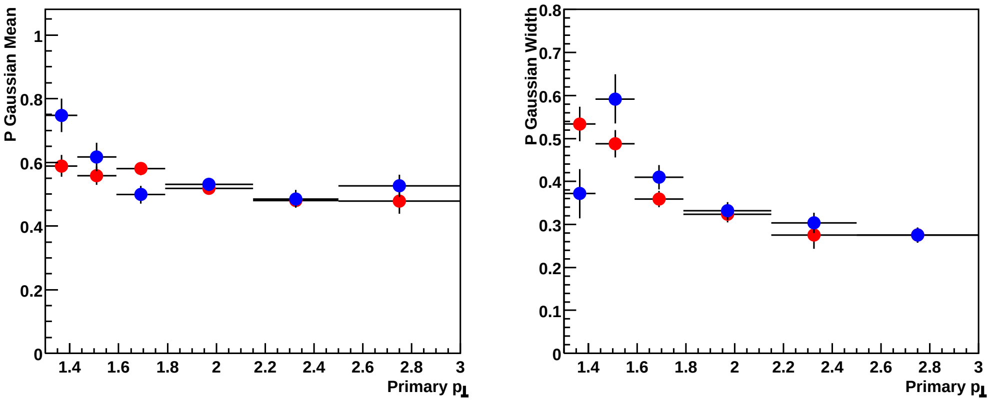

Figure 4.38: Proton Gaussian mean and width vs $p_\perp$

multiple photons are radiated for each charged particle. The area of each Gaussian photon peak then has to be normalized using the mean number of photons radiated by a charged particle of the corresponding mass. Thus, determining the error for the charged particle ratio requires estimating the mean number of photons found within each of the truncated Cherenkov Fiducial areas. To determine the number of photons found within the Cherenkov Fiducial areas, a method has to be devised to discriminate between the different Cherenkov Fiducial areas on a track-by-track basis. The Cherenkov photons radiated by the charged particle will all lie within one of the predicted Cherenkov Fiducial areas. In the absence of any background, a simple counting method would suffice to discriminate between the various possibilities. It is expected that photons will be found in more than one predicted Cherenkov Fiducial area in the presence of backgrounds. The photon background on the RICH pad plane is approximately random in character, and thus the amount of background photons one would expect to find will scale with the search area. The predicted π, K and P Cherenkov Fiducial areas for a given track will, in general, have different integrated areas and thus are expected to pick up differing amounts of background. The Cherenkov Fiducial area depends on a number of parameters, most notably the track's momentum, angle of incidence, and the hypothetical mass. In general, for a given momentum, the area occupied by the Cherenkov Fiducial area predicted for the

π will be the largest, followed by the Kaon and then the Proton. In addition, the number of photons radiated by a charged particle depends on the particle's velocity. It is expected that, on average, π's will generate the most light, followed by Kaon's, and then Proton's (see the section detailing the detector for more details).

A photon density can be defined for each truncated Cherenkov Fiducial area predicted for a particular track by dividing the number of photons found within the truncated Cherenkov Fiducial area by the integrated area occupied on the pad plane. The number of photons found within a predicted Cherenkov Fiducial area for a single track is calculated by selecting photons lying within 2 sigma of the mean, (see Figures 4.36,4.37,4.38). In this way a set of three photon densities can be constructed for each track. Thus, the π photon multiplicity can be estimated by selecting tracks having π photon densities which are larger than the K and P densities. Likewise, the Kaon and Proton photon multiplicities can be estimated in a similar manner. Figure 4.39 shows

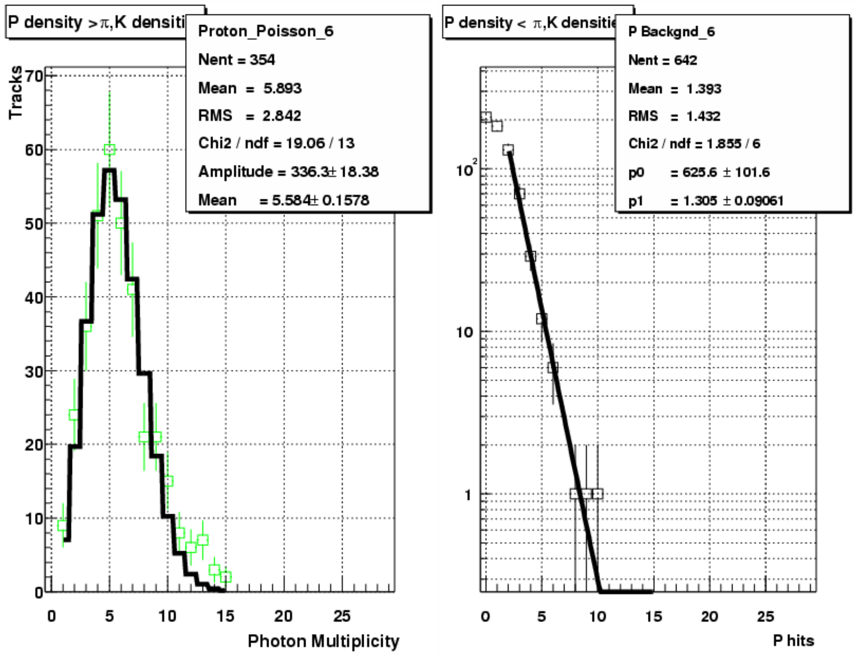

Figure 4.39: Distribution of photons found within truncated Proton Cherenkov Fiducial area, $2.25 < p_{\perp}[GeV/c] < 2.5$. Left panel shows Poisson distribution of photons found for tracks having large proton ring density. Right panel shows background found in proton Cherenkov rings.

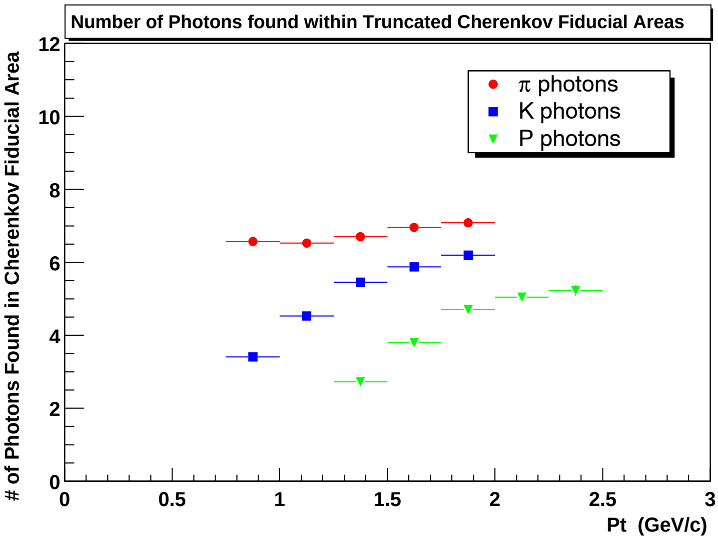

Figure 4.40: Number of photons found in π,K, and P rings as function of transverse momentum. A cut has been applied to the search area for each Cherenkov Fiducial area to remove the forward section of each ring to reduce the background.

the photon multiplicity for tracks having P photon densities greater than the π or K densities. The photon multiplicity distributions for Proton's are well described by Poisson distributions, with similar results for the π and K particle species. The mean number of photons found within each truncated Cherenkov Fiducial area is plotted as a function of momentum in Figure 4.40. The mean number of photons found within the truncated Cherenkov Fiducial areas will depend on the chamber gain and thus will differ quadrant-by-quadrant by small amounts. The difference between the East and West halves of the chamber (see Figure 4.31) are $\lesssim 3\%$ and are averaged to calculate the normalization factor used to calculate the error associated with the particle ratio obtained by the photon counting method.

4.5 Particle Ratio's

The normalized distribution of photons calculated relative to the predicted Cherenkov Fiducial areas for the π, K and P described above can be used to provide a measure of the charged particle ratios for the particle species of interest, $\frac{\pi^-}{\pi^+}$, $\frac{K^-}{K^+}$ and $\frac{\overline{P}}{P}$. The number of Cherenkov photons radiated by a charged particle is independent of the sign of the charge, thus the particle ratios can be measured by counting the number of photons found within the predicted Cherenkov Fiducial areas for positive and negative tracks separately. The number of photons found within the Cherenkov Fiducial area is gotten from the Gaussian area obtained from the fit described in the following subsection.

The tracks were selected having a large number of hits, (> 35), to ensure a well defined track. The last hit used in the primary fit was required to have a cylindrical radius greater than 185 cm, lying very close to the RICH. The tracks were selected having $|\eta| < 0.2$ and residuals at the RICH pad plane of less than 9 mm (in both the drifting and bending directions). The tracks were not allowed to cross the central membrane and were selected from events with a primary vertex located ±70 cm from the center of the TPC. Finally, the tracks were required to have intersection points with the RICH pad plane at least 20 cm away from the center of the RICH. This reduces the influence of any tracking irregularities caused by the central membrane (see Figures 4.7 and 4.9). Variation of the number of hits used or the position of the last hit used in the fit had little impact on the analysis. The cut values for the RICH residuals and the distance from the central membrane were investigated and this will be reported in the following section along with the east-west systematics.

4.5.1 Fitting Procedure

The fit procedure was done within the ROOT [46] environment using MINOS minimization routines. The function used in fitting the normalized distance distributions for the π Cherenkov Fiducial areas is explicitly shown below for the case where the π and K peaks are prominent (as in Figure 4.41),

$$\begin{aligned}\text{fit function} = {} & \frac{\mathrm{A}_\pi}{\sigma_\pi\sqrt{2\pi}}\exp\left(-\frac{(\mathrm{d}_\pi-\overline{\mathrm{d}_\pi})^2}{2\sigma_\pi^2}\right)+\frac{\mathrm{A}_\mathrm{K}}{\sigma_\mathrm{K}\sqrt{2\pi}}\exp\left(-\frac{(\mathrm{d}_\pi-\overline{\mathrm{d}_\mathrm{K}})^2}{2\sigma_\mathrm{K}^2}\right) \\ & +p_0+p_1(d_\pi-d_{offset})+p_2(d_\pi-d_{offset})^2+p_3(d_\pi-d_{offset})^3.\end{aligned} \tag{4.24}$$

Similar functions were used for the fits describing the K and P distributions. The Gaussian parameters $A_{\pi,K}$ describe the area of each Gaussian and represent the number of photons found within the π and K peaks above background. The $\sigma_{\pi,K}$ width parameters along with the means $\overline{d_\pi}$ and $\overline{d_K}$ describe the shape of the photon peaks. The background is described using a polynomial with the parameters p_0, p_1, p_2, p_3. The d_{offset} parameter is used to simplify the fitting procedure and has a value of -6. The polynomial approximation to the background requires four parameters to be used

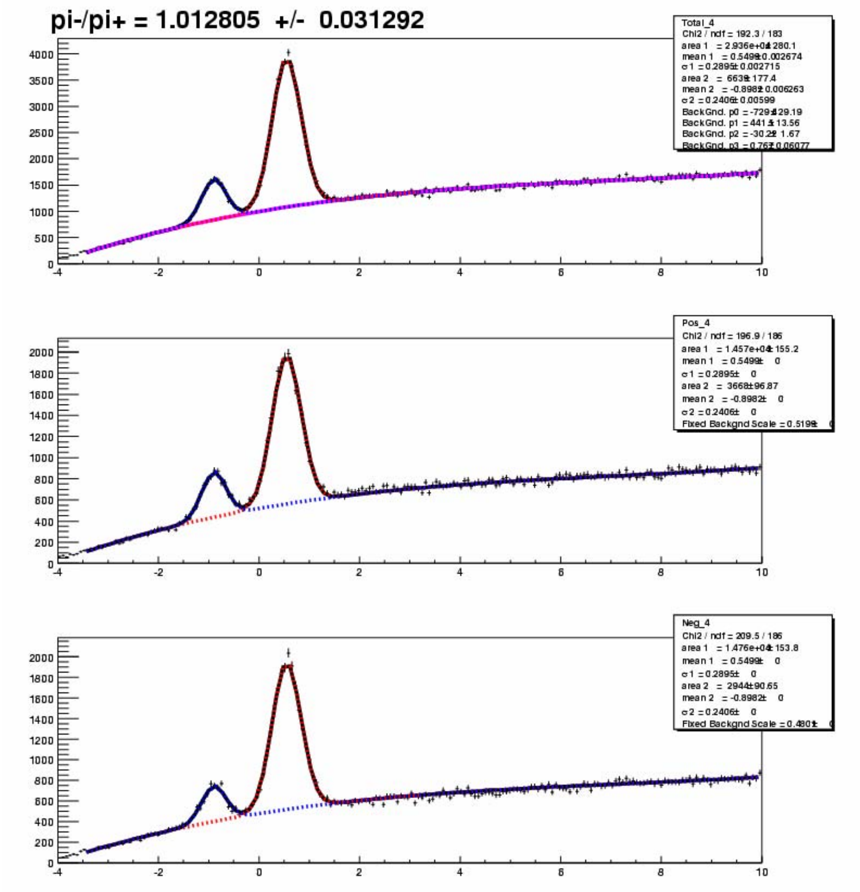

Figure 4.41: d_π distribution for $1.08 < p_\perp[GeV/c] < 1.247$. Top panel: all tracks. Middle panel: positive tracks. Bottom panel: negative tracks.

in the fitting procedure, which, along with the parameters used for the Gaussians, necessitate fits having 10-13 free parameters. The large number of free parameters can be reduced by fixing the means and widths of the Gaussian peaks. The $d_{\pi,K,P}$ distribution can be calculated using the sum of the positively and negatively charged tracks and fitted to the above function. The mean and width for each Gaussian can then be applied to the $d_{\pi,K,P}$ distributions calculated for the positive and negative tracks separately. In addition to this, the shape and magnitude of the background can be fixed using parameters obtained from a fit to the $d_{\pi,K,P}$ distribution using the sum of the positively and negatively charged tracks. The magnitudes for the background shapes used for the positive and negative tracks will be different and were found by calculating the ratio of the photons found for points far removed from the Cherenkov rings ($9 > d_{\pi,K,P} > 10$) for the individual track charge relative to the sum of the track charges. Thus, after fitting the $d_{\pi,K,P}$ distributions for the sum of the positive and negative tracks and applying the results to the fits for the individual track charges separately, the only free parameters left are the areas, $A_{\pi,K,P}$. The particle ratio's $\frac{\pi^-}{\pi^+}$, $\frac{K^-}{K^+}$ and $\frac{\overline{P}}{P}$ can then be measured by taking the ratio of areas obtained in the fits for the positive and negative tracks.

Chapter 5

Results and Discussion

5.1 Overview

The ratios of charged Pions, Kaons, and Protons measured at high transverse momentum using a RICH detector are presented in this section. The ratios were measured in the rapidity interval $|\eta| < 0.2$, and obtained from Au+Au collisions at a center of mass energy of 130 GeV per nucleon pair. The distribution of the hadrons produced in the Au+Au collisions is steeply falling as a function of transverse momentum, and is a strong function of the collision geometry. The number of charged particles crossing the RICH having momenta above 1 GeV/c was measured to be $\simeq$ 1/event for central collisions, and much smaller for peripheral collisions. Thus, due to the small acceptance of the RICH detector, the centrality selection of the collisions was restricted to the 14% most central events to maximize the statistics. The $\frac{\pi^-}{\pi^+}$ and $\frac{K^-}{K^+}$ measurements ranged from a p_T of 0.75 to 2.0 GeV/c, and the $\frac{\bar{p}}{p}$ measurement was done over a larger p_T range from 1.3 to 3.0 GeV/c. The upper limit on the p_T range of π and K ratios was limited by the π-K separation, while the proton upper limit was limited by statistics. The particle ratios are consistent with being flat in the p_T range measured and follow the trends versus $\sqrt{s_{NN}}$ established in pp, pA and AA collisions at lower energies.

In section 5.2 the measured ratios are presented and discussed. Section 5.3 offers comparisons of the measured ratios with similar measurements made with pp and

AA collision systems at lower center of mass energies. Expectations from theory are presented and discussed. Finally, in section 5.4, comparisons with models emphasizing various aspects of the physics are presented as well.

5.2 Charged Particle Ratios

The identified particle ratios were measured as a function of transverse momentum with the RICH. The tracks were selected such that they did not cross the Central Membrane (CM) and had all their points 20 cm or more from the CM. This reduced the influence of electric field distortions on the hit distributions. The pseudo-rapidity range was $|\eta| \leqslant 0.3$. The detected particle yields, $Y_{particle}$, are expected to be affected by detector inefficiencies, which in general will be different for each experimental set-up. To make comparisons with theory and other experiments, corrections $F_{correction}$ to the particle yields will be required, $Y_{corrected} = F_{correction} Y_{particle}$. These correction factors are not always known and as such can pose a serious problem for the experimenter. However, the charged track acceptance for STAR is symmetric for the different track charges. When measuring the ratio of the charged particle yields, the correction factors will tend to cancel. Ratio measurements are therefore inherently less prone to systematic errors, brought about by detector inefficiencies than the corresponding particle yield measurements allowing easier comparison with theory and other measurements. However, the charged particle ratios presented in this thesis and elsewhere, can in principle be modified by effects such as annihilation in the detector material and feed down from weak decay products. Annihilation in the detector material is a strong function of the particle's momentum and is most evident at low momenta. Thus annihilation is a small effect for the high momentum tracks used in this work. These effects all play minor to negligible roles and are not corrected for in this work. Details specific to each ratio measurement will be addressed in the appropriate subsection.

5.2.1 $\frac{\pi^-}{\pi^+}$ vs $p_\perp$

The measured charged pion ratio is shown in Figure 5.1 vs transverse momentum. The panel on the left depicts the ratio measured using tracks originating from the East half of the TPC, while the right hand panel shows results of the measurement using tracks on the West side of the TPC. A residual measured on the RICH pad plane in both the drift and bend directions of less than 0.9 cm was required. The ratio vs $p_\perp$ was fitted to a straight line from 0.75 to 2.0 GeV/c. The $\frac{\pi^-}{\pi^+}$ measurement on the East side has a mean value of $0.994 \pm 0.011_{stat.}$ with a $\chi^2/\text{dof} = 6.991/6$. The $\frac{\pi^-}{\pi^+}$ measurement on the West side has a mean value of $0.995 \pm 0.012_{stat.}$ with a $\chi^2/\text{dof} = 15.32/6$. The measurement conducted on the West side of the TPC exhibits significantly more point-to-point variation as compared to the East side. The reason for this is not completely understood and is still being studied and is reflected in similar behavior in the other STAR measurements, such as track point residual studies for the East

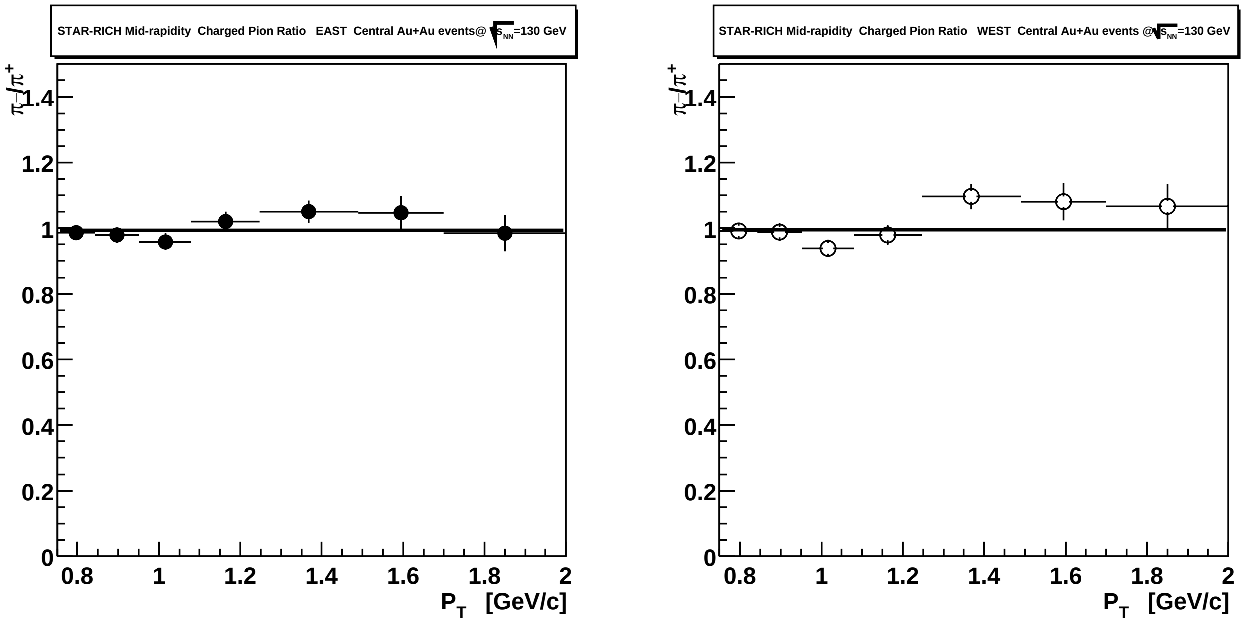

Figure 5.1: $\frac{\pi^-}{\pi^+}$ vs $p_\perp$ at mid-rapidity for the 14% most central Au-Au events at $\sqrt{s_{NN}} = 130$ GeV. Track hit points were required to lie more than 20 cm from CM. Left panel shows measurements conducted on East side of TPC, Right panel shows results from West side of TPC.

and West sides. Nevertheless, the mean ratio on the West side is nearly identical to the East measurement.

The top panels in Figure 5.2 show the mean value of the charged pion ratio plotted vs the track's residual measured at the RICH pad plane. The leftmost panels show the measurements made on the East side (solid points), and the right side panels show the West side results (hollow points). Two sets of measurements are superimposed on each panel. The square data points (blue) show the results for tracks which were required to reside entirely on one side of the TPC, i.e. not crossing the CM. The circle data points (red) are a subset of these tracks, having the additional requirement that all track points be 20 cm or more away from the Central Membrane. The mean values of the $\frac{\pi^-}{\pi^+}$ fit show no variation with the track's residual measured at the RICH pad plane or position relative to the CM, East or West. The upper panels show the χ^2s obtained from the fits performed on each of the ratio measurements. There is only a slight variation of the χ^2 values vs the track's residual measured at the RICH pad plane. The χ^2 values show a systematic decrease with decreasing track residual on the East side, with no decrease and possibly an increase on the West side. The largest difference comes from the ratios measured using tracks that were required to have no track points within 20 cm of the CM. The χ^2 is significantly smaller for the fits performed using these tracks as compared to the track sample having track points lying close to the Central Membrane. This behavior is seen in all the measured ratios, (including K and P) and is of no serious consequence as the East and West mean values are within errors.

The detectors are symmetric for the different track charges and thus no acceptance corrections were necessary for the ratio measurements presented in this work. The Cherenkov ring radii for $e^{\pm}$ and $\pi^{\pm}$ are nearly identical in the momentum range in which the measurements were made and thus, in principle, a correction is necessary to account for the electron contamination. Extrapolating[7] the $e^{\pm}$ yields at small momenta out to high $p_{\perp}$ indicates this to be $\lesssim 1\%$ and therefore is ignored for this study. The charged pion ratio averaged over both halves of the TPC is $0.994 \pm 0.008_{stat.} \pm 0.01_{sys.}$.

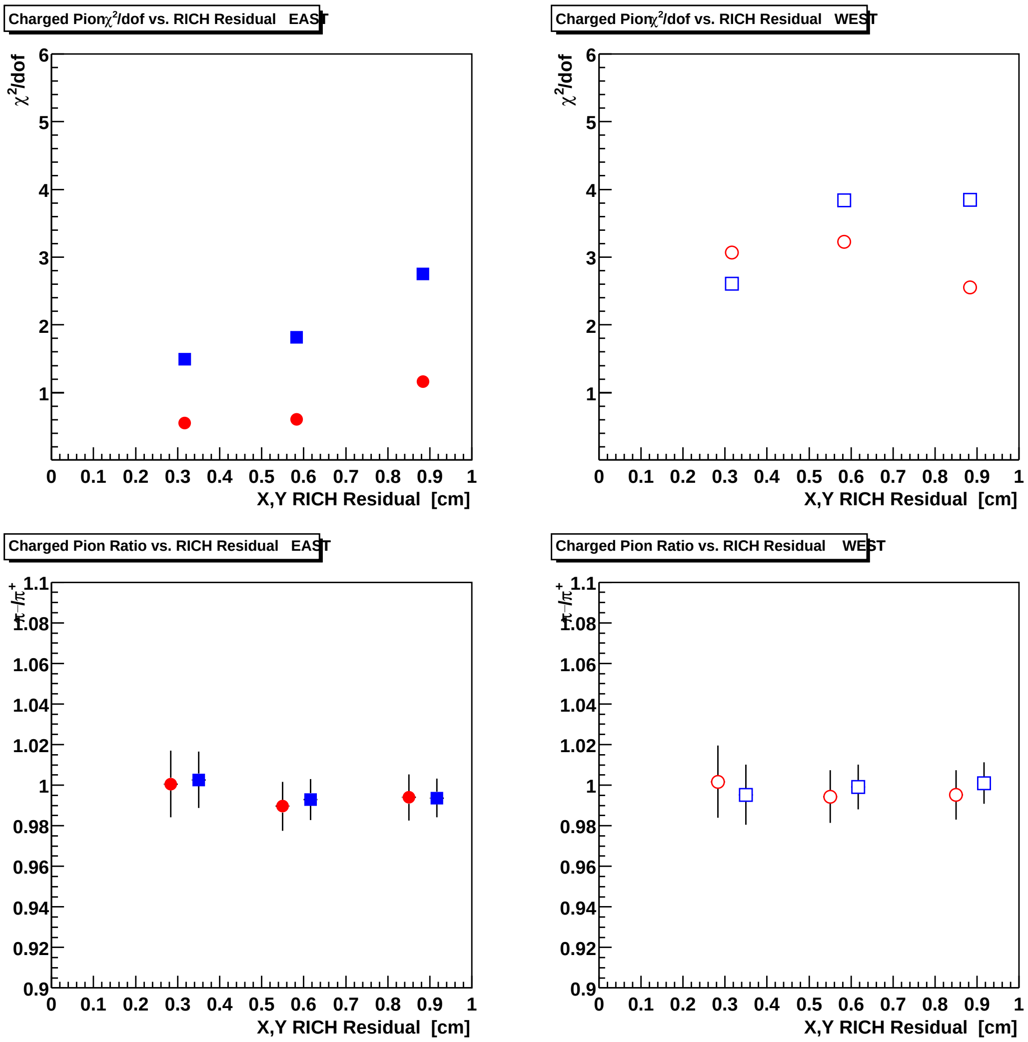

Figure 5.2: Lower left (right) panel shows the $\frac{\pi^-}{\pi^+}$ ratio averaged over $p_\perp$ as a function of the RICH residual for central events as measured in the East (West) side of TPC. Top panel shows the $\chi^2/d.o.f$ obtained from the fit of the $\frac{\pi^-}{\pi^+}$ ratio, plotted as a function of the RICH residual. Solid circles indicate 20 cm cut placed on track points to remove tracks close to CM. Ratio measurements on West side show systematic variations as discussed in the text.

Determination of Mean Value and Systematic Error

The mean values reported for the ratios,$(\frac{\pi^-}{\pi^+}, \frac{K^-}{K^+}, \frac{\bar{p}}{p})$, were selected using the track sample having residuals as measured at the RICH pad plane of 0.9 cm in the bending and drift directions. The residual offers a measure on the track quality. A residual of

0.9 cm represents a 3σ cut on the residual distribution. Tracks having large (> 0.9 cm) residuals are an indication that the tracking was of low quality and/or the track suffered multiple scattering in the material outside of the TPC and in front of the RICH pad plane. To maximize statistics and minimize systematic errors in tracking, tracks having residuals less than 0.9 cm in the drift and bend directions were selected to determine the mean. The systematic error for the charged pion ratio presented in this work, (along with $\frac{K^-}{K^+}$, $\frac{\bar{p}}{p}$), was estimated from the maximum difference in the mean value of the ratio, as determined from measurements made on the East and West sides of the TPC. This is the largest contribution to the systematic error of the ratio for measurements presented in this thesis, as well as for the dE/dx ratio measurements made by STAR.

Collaboration	Centrality	$\frac{\pi^-}{\pi^+}$ Measurement Result	$P_\perp$ [GeV/c]
STAR-RICH	14%	$0.99 \pm 0.01_{stat.} \pm 0.01_{sys.}$	0.75 - 2.0
PHOBOS [47]	12%	$1.00 \pm 0.01_{stat.} \pm 0.02_{sys.}$	0.1-0.55
PHENIX [48, 49]	15%	$0.943 \pm 0.01_{stat.} \pm 0.12_{sys.}$	0.1-2.0
BRAHMS [50]	40%	$0.95 \pm 0.03_{stat.} \pm 0.05_{sys.}$	0.2-1.2
RHIC Ave.		**0.99 ± 0.01**	

Table 5.1: Charged π ratio as measured by the 4 RHIC collaborations. RHIC average determined using statistical errors combined in quadrature with the systematic errors.

5.2.2 $\frac{K^-}{K^+}$ vs $p_\perp$

The charged kaon ratio measured as a function of transverse momentum is shown in Figure 5.3. The panel on the left depicts the ratio measured using tracks originating from the East half of the TPC, while the right hand side panel shows the results of the measurement using tracks on the West side of the TPC. A residual measured on the RICH pad plane in both the drift and bend directions of less than 0.9 cm was required. The ratio vs $p_\perp$ was fitted to a horizontal line from 0.75 to 2.0 GeV/c. The $\frac{K^-}{K^+}$ measurement on the East side has a mean value of $0.871 \pm 0.019_{stat.}$ with a $\chi^2/\text{dof} = 5.24/6$. The $\frac{K^-}{K^+}$ measurement on the West side has a mean value of $0.893 \pm 0.022_{stat.}$ with a $\chi^2/\text{dof} = 21.32/6$. Figure 5.4 is similar to Figure 5.2 and

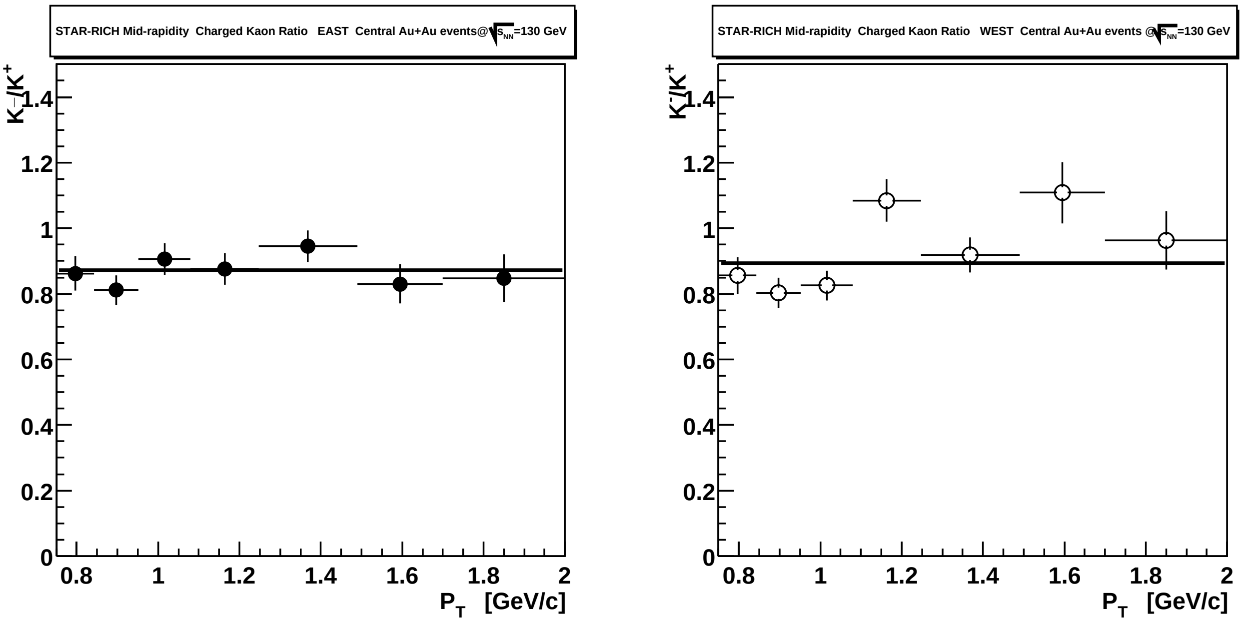

Figure 5.3: $\frac{K^-}{K^+}$ vs $p_\perp$ at mid-rapidity for the 14% most central Au-Au events at $\sqrt{s_{NN}} = 130$ GeV. Track hit points were required to lie more than 20 cm from CM. Left panel shows measurements conducted on East side of TPC, right panel shows results from West side of TPC.

shows the variation of the mean versus the track's residual measured at the RICH pad plane in the bottom panels. The effect of the 20 cm CM cut is shown in color, in the same manner as for the pion ratio in Figure 5.2. The mean value of the charged kaon ratio shows a maximum variation of approximately 8% when comparing the East and West measurement. The upper panels in Figure 5.4 show the χ^2 values from the fits performed on the charged kaon ratio measured as a function of $p_\perp$. The χ^2 values for the means measured on the West side of the TPC are far larger than the corresponding values on the East half, and show a similar pattern as seen in the χ^2 values for the charged pion ratio, Figure 5.2. Again, no acceptance corrections were made due to the charge symmetry of STAR.

The charged kaon ratio has been measured within the STAR experiment using two other techniques, via specific energy loss in the TPC gas and via a "Kink" measurement where the kaon is identified by the decay topology of the kaon following a weak decay, $K^\pm \rightarrow \mu^\pm \nu$ and $K^\pm \rightarrow \pi^\pm \pi^0$. The dE/dx measurement was limited to a $p_\perp$

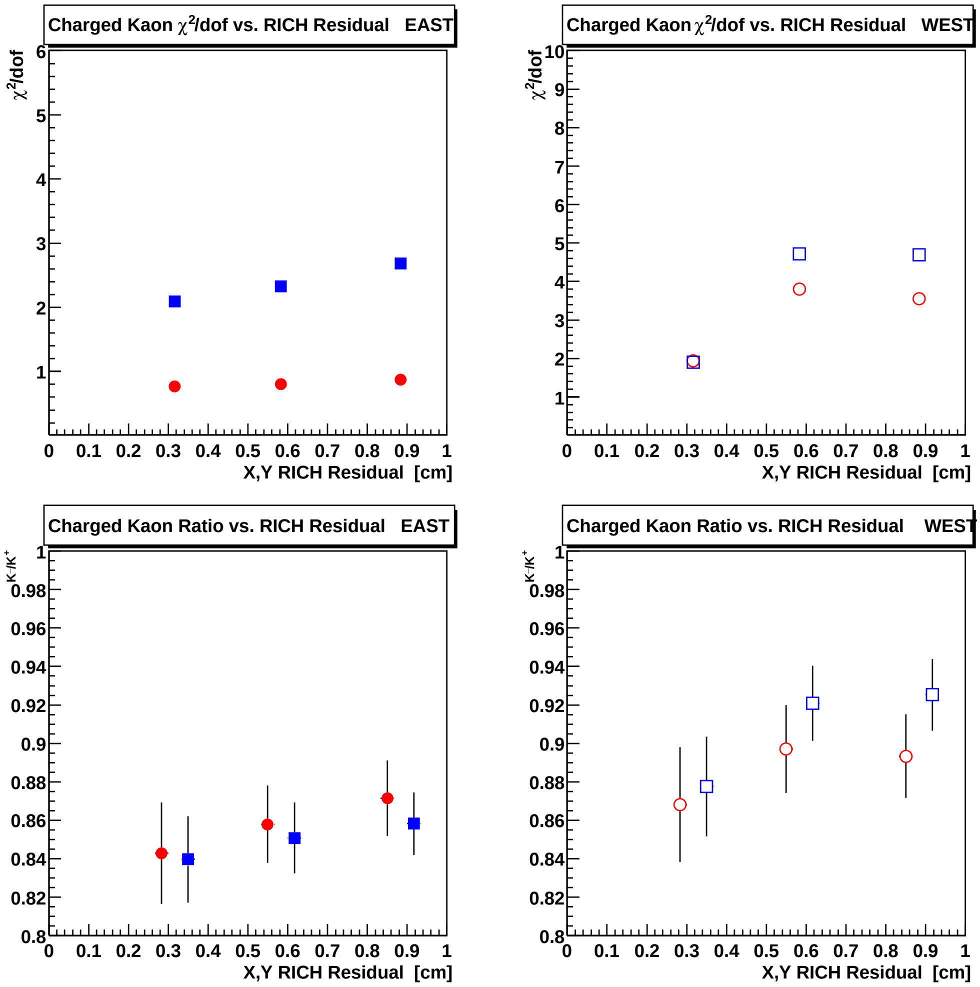

Figure 5.4: Lower left (right) panel shows the $\frac{K-}{K+}$ ratio averaged over $p_\perp$ as a function of the RICH residual for central events as measured in the East (West) side of TPC. Top panel shows the $\chi^2/d.o.f$ obtained from the fit of the $\frac{K-}{K+}$ ratio versus $p_\perp$, plotted as a function of the RICH residual. Solid circles indicate 20 cm cut placed on track points to remove tracks close to CM. Ratio measurements on West side show systematic variations as discussed in the text.

range of 0.15 - 0.6 GeV/c while the Kink measurement was able to extend the range up to 2.0 GeV/c. Kink measurements give a $\frac{K-}{K+}$ ratio of $0.89 \pm 0.008_{stat.} \pm 0.038_{sys.}$ and the dE/dx measurement of the ratio is $0.94 \pm 0.007_{stat.} \pm 0.026_{sys}$. The charged kaon ratio as measured with the STAR-RICH (averaged over both halves of the TPC) is $0.880 \pm 0.014_{stat.} \pm 0.068_{sys.}$. The small difference between these three types of measurements are within the errors of the methods. Additional measurements of this ratio were made by other experimental collaborations at RHIC, and are presented in table format, 5.2.2.

Collaboration	Centrality	$\frac{K^-}{K^+}$ Measurement Result	$P_\perp$ [GeV/c]
STAR-RICH	14%	$0.88 \pm 0.014_{stat.} \pm 0.068_{sys.}$	0.75 - 2.0
STAR-TPC (dE/dx) [51, 7]	11%	$0.92 \pm 0.007_{stat.} \pm 0.026_{sys}$	0.15 - 0.6
STAR-TPC (Kink) [51, 7]	11%	$0.88 \pm 0.011_{stat.} \pm 0.04_{sys.}$	0.15 - 2.0
PHENIX [48, 49]	14%	$0.87 \pm 0.05_{stat.} \pm 0.13_{sys.}$	0.5-1.5
PHOBOS [47]	12%	$0.91 \pm 0.07_{stat.} \pm 0.06_{sys.}$	0.2 - 0.7
BRAHMS [52]	40%	$0.89 \pm 0.07_{stat.} \pm 0.05_{sys.}$	0.4 - 1.6
RHIC Ave.		**0.903 ± 0.02**	

Table 5.2: Charged K ratio as measured by the 4 RHIC collaborations. RHIC average determined using statistical errors combined in quadrature with the systematic errors.

5.2.3 $\frac{\bar{p}}{p}$ vs $p_\perp$

The anti-proton to proton ratio measured as a function of transverse momentum is shown in Figure 5.5. The panel on the left depicts the ratio measured using tracks originating from the East half of the TPC, while the right hand side panel shows the results of the measurement using tracks on the West side of the TPC. The tracks used in the measurement presented in this thesis were subjected to the same track cuts applied to the pion and kaon ratio measurements discussed in subsections 5.2.1 and 5.2.2. The ratio vs $p_\perp$ was fit to a straight line from 1.3 to 2.5 GeV/c and is consistent with being flat. The $\frac{\bar{p}}{p}$ measurement on the East side has a mean value of $0.639 \pm 0.032_{stat.}$ with a $\chi^2/\text{dof} = 3.39/5$. The $\frac{\bar{p}}{p}$ measurement on the West side has a mean value of $0.642 \pm 0.0352_{stat.}$ with a $\chi^2/\text{dof} = 4.2/5$. Figure 5.6 is similar to Figures 5.2 and 5.4 and shows the variation of the mean versus the track's residual measured at the RICH pad plane in the bottom panels. The effect of the 20 cm CM cut is shown in color, in the same manner as for the other two ratio measurements. The mean value of the anti-proton to proton ratio shows a maximum systematic variation

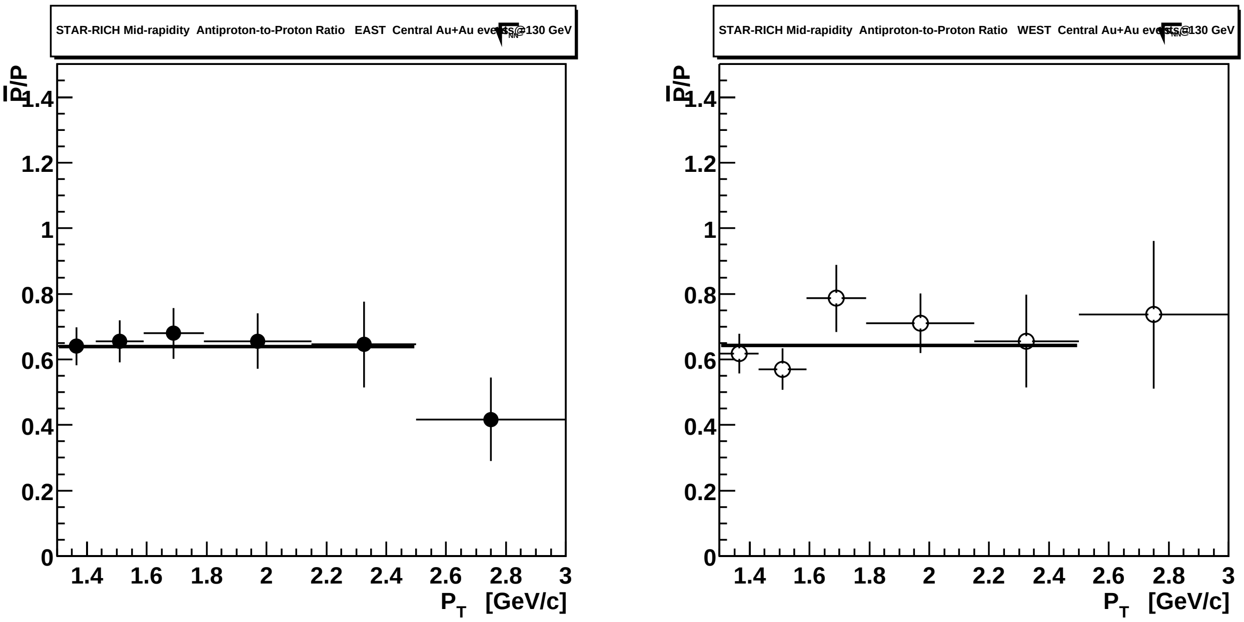

Figure 5.5: $\frac{\bar{p}}{p}$ vs $p_{\perp}$ at mid-rapidity for the 14% most central events. Results for the measurements conducted on the East and West sides of the TPC are shown separately. Tracks were selected by requiring all track hits to be at least 20 cm away from Central Membrane and have a RICH residual of less than 0.9 cm in the drift and bend directions.

of approximately 6% when comparing the East and West measurements. The upper panels in Figure 5.6 show the χ^2 values as a function of the tracks residual. The χ^2 values for the means measured with the West half of the TPC are far larger than the corresponding values on the East side, and show a similar pattern as seen in the χ^2 values for the charged pion and kaon ratios, Figures 5.2 and 5.4.

Like the other two ratio measurements, the STAR experiment is symmetric for the different track charges and thus no acceptance corrections were made. In principle, the anti-proton yield will be slightly reduced as a result of annihilation in the detector material, requiring a correction to the anti-proton to proton ratio. However, this correction factor was calculated in Ref. [53] to be less than 2% for all momenta above 0.6 GeV/c, and thus is not needed for this analysis. The proton yield contains, in principle, contributions from decays of heavier baryons, most prominently from the Λ, Σ, Ξ and Ω particles. In [51] the $\frac{\bar{\Lambda}}{\Lambda}$ ratio has been measured to be $0.69{\pm}0.01_{stat}$, the $\frac{\bar{\Xi}^+}{\Xi^-}$

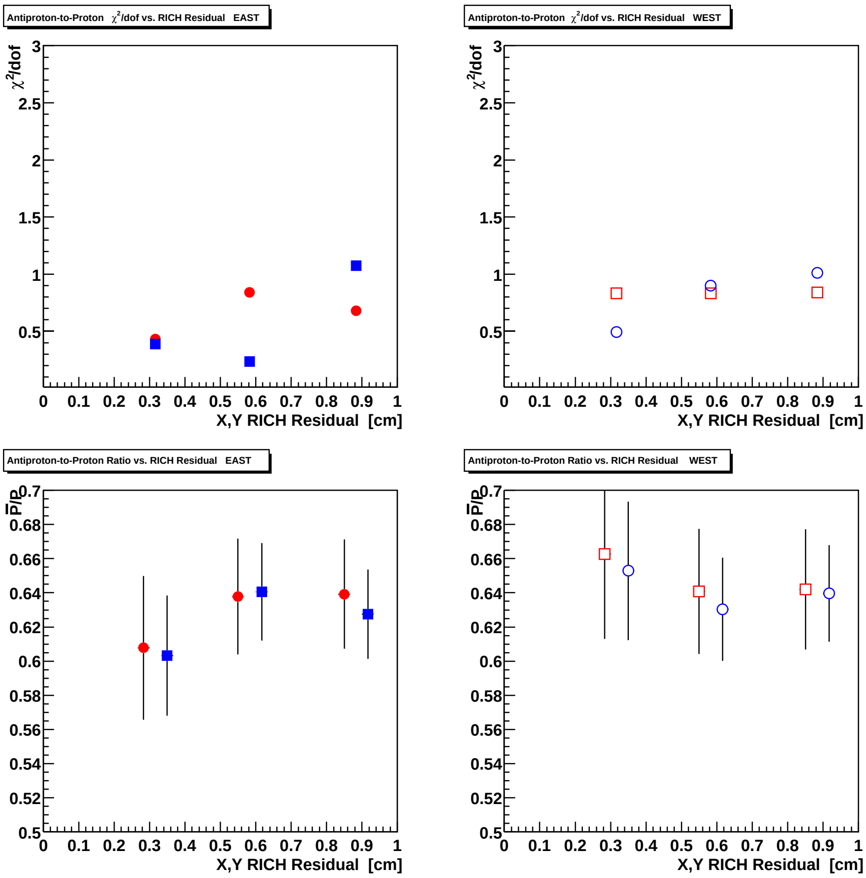

Figure 5.6: Lower left (right) panel shows the $\frac{\bar{p}}{p}$ ratio averaged over $p_\perp$ as a function of the RICH residual for central events as measured in the East (West) side of TPC. Top panel shows the $\chi^2/d.o.f$ obtained from the fit of the $\frac{\bar{p}}{p}$ ratio versus $p_\perp$, plotted as a function of the RICH residual. Solid circles indicate 20 cm cut placed on track points to remove tracks close to CM. Ratio measurements on West side show systematic variations as discussed in the text.

has been measured to be $0.86 \pm 0.04_{stat}$ and the $\frac{\bar{\Omega}^+}{\Omega^-}$ was measured to be $0.95 \pm 0.15_{stat}$. The effect of feed-down has been taken into account in these ratios. The values for the $\frac{\bar{\Lambda}}{\Lambda}$, $\frac{\bar{\Xi}^+}{\Xi^-}$, and $\frac{\bar{\Omega}^+}{\Omega^-}$ ratios are close to the $\frac{\bar{p}}{p}$ value reported in this work and thus the correction is expected to be minor. Feed-down from these higher mass particle states into p and $\bar{p}$ occurs mainly through the Λ and $\bar{\Lambda}$ decays. It is possible to estimate the maximum feed-down effect from Λ decay on the $\frac{\bar{p}}{p}$ ratio by assuming the yield of Λ particles is the same as for protons, and the Λ particles decay 100% into protons.

This leads to a correction of ∼14% which is an overestimation, as the integrated yield of Λ particles is expected to be lower than that of protons. In addition, the branching ratio[54] for Λ decay into protons ($\Lambda \rightarrow p\pi^-$) is approximately 64% and thus the actual feed-down effect is expected to be smaller, ∼8-9% which is within the quoted error of the $\frac{\bar{p}}{p}$ reported in this work. Regardless of origin, all corrections are believed to play minor roles in the ratio and are not included.

The ratio is consistent with being flat over the entire momentum range in which the ratio was measured. However, beyond 2.5 GeV/c the $\frac{\bar{p}}{p}$ ratio (Figure 5.5) shows a possible drop in the last data point. The large error bars associated with the data points precludes any definitive statement on this, and as such the ratio was fit to a straight line only over the limited momentum range of 1.3 - 2.5 GeV/c. The mean value of the ratio (averaged over both halves of the TPC) is then $\frac{\bar{p}}{p} = 0.640 \pm 0.024_{stat.} \pm 0.06_{sys.}$. This is in agreement with the 14% most central $\frac{\bar{p}}{p}$ as measured by the STAR TPC using the dE/dx method [53]. Additional measurements of this ratio were made by other experimental collaborations at RHIC, and are presented in table format, 5.2.3.

Collaboration	Centrality	$\frac{\bar{p}}{p}$ Measurement Result	$P_{\perp}[GeV/c]$
STAR-RICH	14%	$0.64 \pm 0.024_{stat.} \pm 0.06_{sys.}$	1.3 - 2.5
STAR-TPC (dE/dx) [53, 7]	14%	$0.63 \pm 0.02_{stat.} \pm 0.06_{sys}$	0.4 - 1.0
PHENIX [48, 49]	15%	$0.66 \pm 0.03_{stat.} \pm 0.09_{sys.}$	0.5 - 3.0
PHOBOS [47]	12%	$0.60 \pm 0.04_{stat.} \pm 0.06_{sys.}$	0.15 - 1.0
BRAHMS [55]	40%	$0.64 \pm 0.04_{stat.} \pm 0.06_{sys.}$	0.15 - 2.4
RHIC Ave.		**0.63 ± 0.03**	

Table 5.3: Anti-proton to proton ratio as measured by the 4 RHIC collaborations. RHIC average determined using statistical errors combined in quadrature with the systematic errors.

5.3 Nucleon-Nucleon and Nucleus-Nucleus Comparisons

Given the complexity of Nucleus-Nucleus collisions, it is fruitful to make the assumption that a Nucleus-Nucleus collision can be treated as a simple superposition of Nucleon-Nucleon collisions. In this way any deviation from the established pp results can then be directly attributable to the nuclear environment. In order to do this, it is helpful to first review the event structure of a typical high energy pp collision, with a particular emphasis placed on the charged particle ratios, $\frac{\pi^-}{\pi^+}, \frac{K^-}{K^+}, \frac{\bar{p}}{p}$. Particle identification was accomplished in a limited fashion at the UA1-5 ($\sqrt{s}$ varied from 0.2 to 0.9 TeV) experiments by identifying the strange particles through their weak decay topologies. However, this leaves out the other charged particles. So this thesis will focus on the pp physics and the charged particle ratios measured at the ISR ($\sqrt{s}$ varied from 23 to 63 GeV), where particle identification was attempted on all stable, charged particle species using a combination of a Cherenkov counter together with a Time of Flight technique. In the following section, comparisons to the charged particle ratios measured at the ISR will be made with the $\frac{\pi^-}{\pi^+}, \frac{K^-}{K^+}, \frac{\bar{p}}{p}$ ratios reported in this thesis using Au+Au data at $\sqrt{s_{NN}} = 130$ GeV.

The phenomenology of pp collisions has many features, with the mechanisms responsible for the energy loss between the incoming baryons in an inelastic collision being the most relevant for this discussion. This can be described starting with the leading particle effect [56]. Baryons in the final state are preferentially produced with large $|x_f| = \frac{P_{particle}}{P_{beam}}$ and are seen to carry the conserved baryon number present in the initial state. These leading baryons are seen even in the cases where the nature of the particle changes, as in the event of a flavor- or charge-changing reaction. The greater the similarity between the incoming and leading baryons, the more pronounced is the leading particle effect. Baryon production at small $|x_f|$ is the result of the baryon number either being transported from the beam rapidity to mid-rapidity, or by pair production. The combination of stopping and pair production (in particular their ratio $\frac{Y_{pair}}{Y_{pair}+Y_{stop}}$), can be studied by measuring $\frac{\bar{P}}{P}$.

In general, one expects pair production to be the source of particle production at

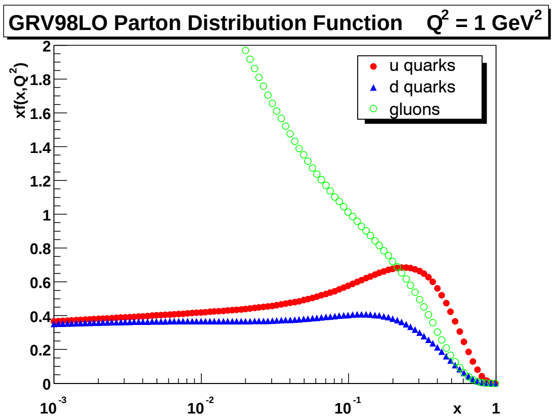

Figure 5.7: The distribution functions xf for up-,down-quarks and the gluons as a function of x, for Q^2=1 GeV^2 as calculated to leading order by GRV [8, 9]

high energies. Parton distribution functions characterize the structure of the incoming proton in terms of the momentum fraction, x, of the proton shared by its constituents. The valence quarks together typically contain about 1/2 of the protons momentum, while the remaining fraction is found in the sea quarks and gluons. The distribution of the partons within the proton will depend on x, as well as the momentum transfer Q^2. Figure 5.7 shows a recent[8, 9] theoretical parameterization of the parton distributions calculated at a scale $Q \sim \frac{p_\perp}{2} = 1$ GeV. The gluons and sea quarks are typified by very small values of x, and are found in increasing numbers at smaller and smaller x. The Q^2 dependence leads to the expectation of much larger gluon densities for the small x values ($x \sim x_\perp = \frac{2p_\perp}{\sqrt{s}} = 0.03$ at $p_\perp = 2$ GeV/c) accessible at the RHIC center of mass energies (as compared to those at the SPS where $x_\perp = \frac{2p_\perp}{\sqrt{s}} \sim 0.2$ at $p_\perp = 2$ GeV/c). Due to the large number of gluons, pair production is then expected to dominate via gluon fragmentation. The large number of gluons present in the initial stage of the collision has important consequences for collisions between heavy ions. It is expected that the large number of gluons will lead to the creation of numerous "mini-jets" which are expected to play a crucial role in the thermalization of the system formed in the heavy ion collision. However, this effect may be reduced somewhat by nuclear

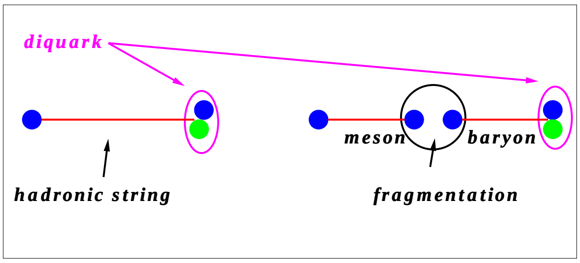

Figure 5.8: Diagram depicting baryon production via diquark-quark string fragmentation.

shadowing, which essentially reduces the number of gluons having small x.

Baryon number transport from the beam- to mid-rapidity region is typically referred to as baryon stopping, and is studied by measuring the net baryon yield, $p - \bar{p}$, as a function of rapidity (see Ref. [57] for a study of baryon stopping at the SPS). Baryon stopping is thought to be one of the mechanisms responsible for converting the energy contained in the incoming projectiles longitudinal motion into transverse momentum and particle production. The amount of baryon stopping is seen to increase from pp to AA collisions[57], indicating an increasing amount of energy being transferred from the beam to the center of mass system in going from pp to AA collisions. The mechanisms responsible for stopping, (both in pp and AA), are still not well understood theoretically. Figure 5.8 shows a simple diagram showing the fragmentation of a diquark-quark hadronic string configuration. Many models incorporate a diquark-quark (qq-q) hadronic string mechanism to describe the stopping, (HIJING for example). However, these models still under-predict the amount of stopping seen in hadronic collisions. Various alternatives have been proposed to enhance

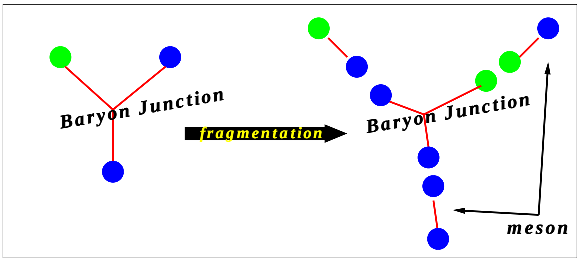

Figure 5.9: Diagram depicting baryon production via the baryon junction mechanism.

the predicted stopping, ranging from diquark breaking, double string fragmentation to baryon junctions, with the baryon junction perhaps being the most successful. Figure 5.9 shows a simple depiction of baryon production via baryon junction fragmentation. In the baryon junction model, the excited baryon is described as a "Y"-shaped string configuration. When the strings undergo fragmentation via $q\bar{q}$ production, the resulting baryon is composed of sea quarks and the valence quarks are contained in mesons. The $p_{\perp}$ of the baryon is obtained by adding the $p_{\perp}$ of the 3 sea quarks. This then leads to a significant enhancement in the baryon's $p_{\perp}$, with the $\langle p_{\perp}^2 \rangle$ of the junction baryon increasing by a factor of three relative to that obtained from qq-q type stopping. For a review on the subject of baryon stopping, see Ref. [57], and for a treatment on baryon junction transport, Ref. [58].

$\frac{\bar{p}}{p}$ Results

The contributions to $\frac{\bar{p}}{p}$ from pair production and from stopping in pp collisions indicate that pair production dominates[59] at the center of mass energies available at the ISR. Figure 5.10 shows $\frac{\bar{p}}{p}$ versus the center of mass energy, $\sqrt{s_{NN}}$, as measured by ISR, together with measurements made with heavy-ion induced reactions. The data points are measured at mid-rapidity. The ISR data points have been corrected for isospin using a simple prescription described in Ref. [60]. The value of $\frac{\bar{p}}{p}$ is seen to generally increase as a function of $\sqrt{s_{NN}}$. The trend established in the pp reactions at ISR seems to be followed by the corresponding values obtained in the heavy-ion induced reactions. The $\frac{\bar{p}}{p}$ value reported in this thesis indicates that pair production

$$\frac{Y_{\bar{p}}}{Y_p} = \frac{Y_{pair}}{Y_{pair} + Y_{stopping}} \approx 0.64 \tag{5.1}$$

continues to dominate at the highest center of mass energy, $\sqrt{s_{NN}} = 130$ GeV. The relative contributions to $\frac{\bar{p}}{p}$ from pair production and from stopping can be estimated as in Equation 5.1, (where Y is the particle yield), indicating that pair production dominates over stopping by a factor of approximately

$$\frac{Y_{pair}}{Y_{stopping}} \approx 3/2. \tag{5.2}$$

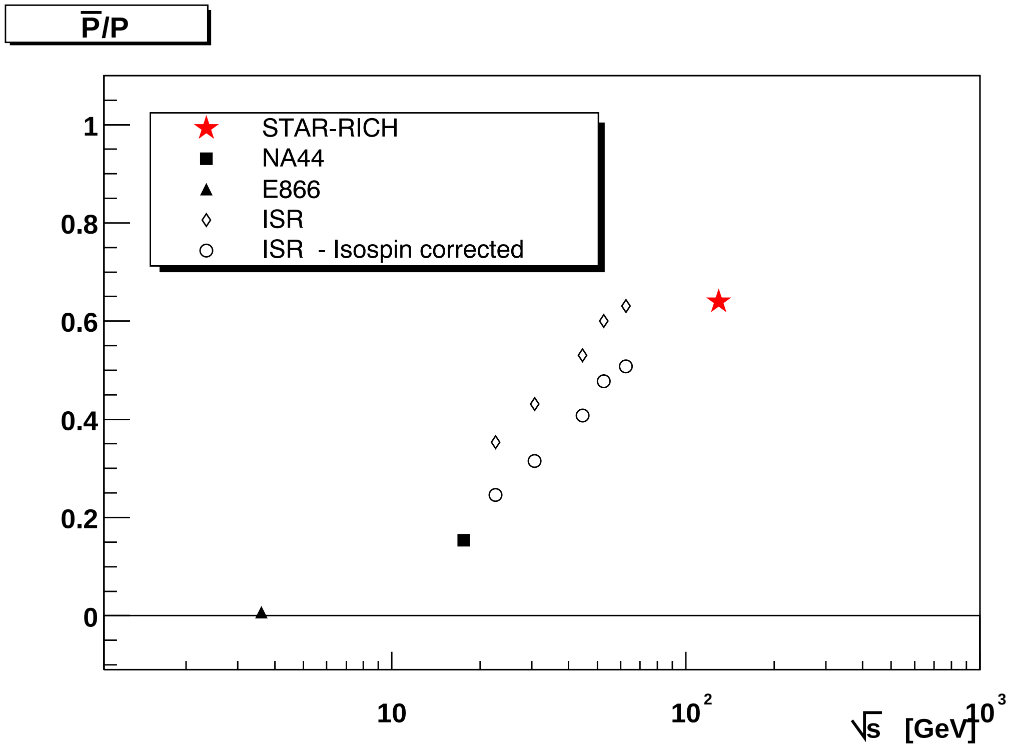

Figure 5.10: $\frac{\bar{p}}{p}$ vs $\sqrt{s_{NN}}$ for pp and AA collision systems. The ISR pp data points are shown with and without isospin corrections applied.

While exhibiting a general increase with $\sqrt{s}$, the antiproton-to-proton ratio, at $0.64 \pm 0.024_{stat.} \pm 0.06_{sys.}$, is still significantly less than 1. This is an indication that the dense matter formed in the heavy ion collisions at RHIC is still not net-baryon free. The implications of a finite net-baryon density has important consequences in the evolution of the system when interpreted in terms of a thermodynamical model and will be discussed later, in subsection 5.4.2.

$\frac{K^-}{K^+}$ Results

A similar trend is seen in the charged kaon ratio. Figure 5.11 shows the charged kaon ratio at mid-rapidity, measured at ISR together with measurements conducted by heavy ion experiments as a function of $\sqrt{s}$. The charged kaon ratio receives contributions from pair production, as in Equation 5.3, as well as from associated

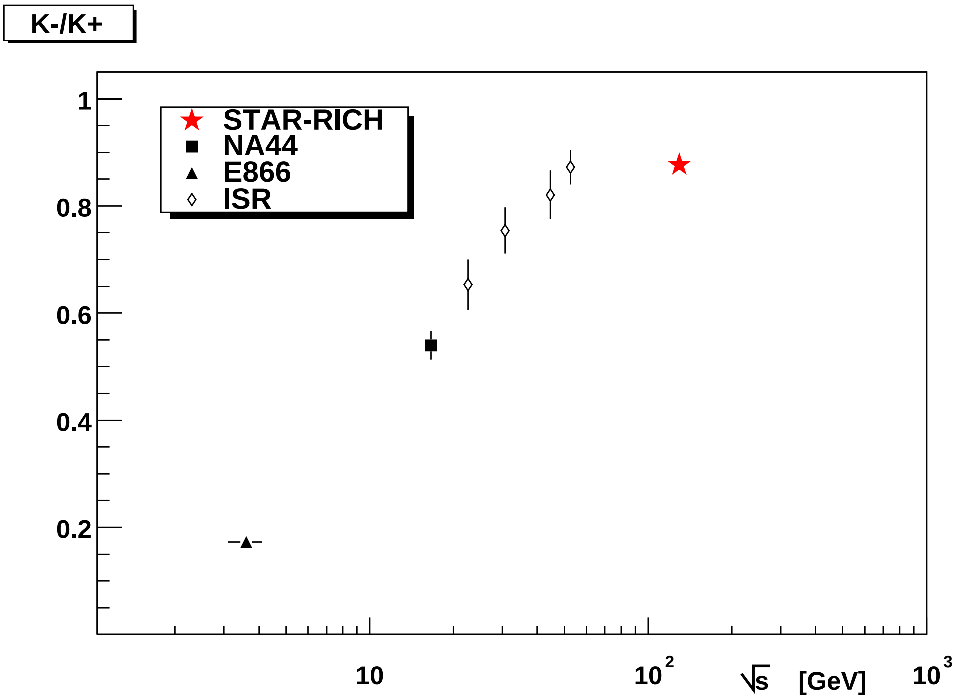

Figure 5.11: $\frac{K^-}{K^+}$ vs $\sqrt{s}$. Data points measured at mid-rapidity. No isospin correction has been applied to the ISR data points.

production, as in Equation 5.4. K^+ production is predominantly due to

$$NN \rightarrow K^+K^- + NN \tag{5.3}$$

$$NN \rightarrow N\Lambda K^+ \tag{5.4}$$

valance quark scattering. This can be contrasted to the case of K^- production. The strange sea quarks contain only a small fraction of the incoming projectile's momentum, making it difficult to participate in a hard scattering that results in the production of a strange meson having high $p_\perp$. Hard scattering involving a strange sea quark would result in the strange quark showing up in a jet together with the strange anti-quark in a separate jet, which is not seen. Rather, charged kaons preferentially appear together in the same jet, indicating K^- production at high $p_\perp$ is dominated by gluon fragmentation. At lower $p_\perp$, sea quarks play a larger role in the particle production. Parton scattering involving an $s\bar{s}$ sea pair can result in the creation of a Λ in conjunction with the strange meson. The charged kaon ratio presented in this thesis is seen to follow the trend established at lower center of mass energies by both the pp and AA measurements (see Figure 5.11), and is an indication that pair production dominates the particle production at large $\sqrt{s}$.

5.3.1 Transverse Momentum Dependence

Nucleon-Nucleon Expectations

In addition to being sensitive to the combined effect of stopping and pair production, the transverse momentum dependence of the anti-proton to proton ratio (as well as $\frac{K^-}{K^+}, \frac{\pi^-}{\pi^+}$) is a sensitive measure of perturbative effects. Particle production at high transverse momentum becomes dominated by the leading hadrons produced by hard scattering amongst the valence quarks of the incoming projectiles. The high $p_\perp$ hadron is increasingly likely to originate from a hard scattering between the incoming valence quarks which carry a significant fraction of the incoming projectile's momentum. For simple colliding systems like pp, the excess of up-quarks relative to down-quarks leads to the expectation of a falling value for the $\frac{\pi^-}{\pi^+}$ ratio as a function of $p_\perp$. This ratio will eventually saturate at a value of ~ 0.5, reflecting the valence number of down-quarks relative to up-quarks present in the initial state.

Similar behavior is expected for the $\frac{K^-}{K^+}$ and $\frac{\bar{p}}{p}$ ratios. However, the valence quark content of $K^-(s\bar{u})$ and the $\bar{P}(\bar{u}\bar{u}\bar{d})$ differ from the charged pions. Neither the $\bar{p}$ nor the K^- have any valance quarks in common with the colliding protons. These particle states necessarily originate from a hard scattering involving a parton from the nucleon sea. The nucleon sea is composed of partons each carrying only a small fraction of the incoming proton's momentum, and are therefore unlikely to participate in the creation of a high $p_\perp$ particle in the final state. Thus, the $\frac{K^-}{K^+}$ and $\frac{\bar{P}}{P}$ ratios are expected to eventually reach values close to zero for sufficiently high values of $p_\perp$.

This behavior of the ratios can be seen in Figures 5.12,5.13 and 5.14, showing the charged particle ratios presented in this thesis, along with those measured at the CERN ISR[61, 62] as well as similar measurements performed at Fermilab[63, 64]. The measurements (ISR) conducted at the higher center of mass energy are systematically higher than the corresponding measurements conducted at the lower center of mass energy (Fermilab). In addition, the ratios are consistent with being flat at the lower momenta and seem to remain so out to larger values of $p_\perp$ for the measurements conducted at the higher center of mass energy before dropping in value. In [65], it is shown that pQCD calculations are able to accurately predict the absolute ***yields*** of the charged particles for values of transverse momenta $p_\perp \gtrsim 4.5$GeV/c. For $p_\perp$ smaller than this, the theory significantly under-predicts the ***yields***. However, it is then shown that the same theory is able to successfully predict the charged particle ***ratios*** for values of $p_\perp$ as low as ~2 GeV/c. The uncertainties in the absolute normalization of the particle ***yields*** tend to cancel when taking the ***ratio***, making the ***ratio*** calculation a more robust one. The predicted[65] $p_\perp$ dependence of the charged pion and kaon ratios are shown with the data in Figures 5.12 and 5.13 and are in relative agreement with the data at high $p_\perp \gtrsim 2$GeV/c.

In [65], the relative contributions from the elementary subprocesses to the charged particle ratios indicate that gluon-quark and gluon-gluon scattering have a stronger dependence on energy than the contribution from quark-quark scattering. Thus, with increasing $\sqrt{s}$, one expects gluon scattering to dominate, resulting in the charged particle ratios tending towards unity, which is what is seen in Figures 5.10 and 5.11.

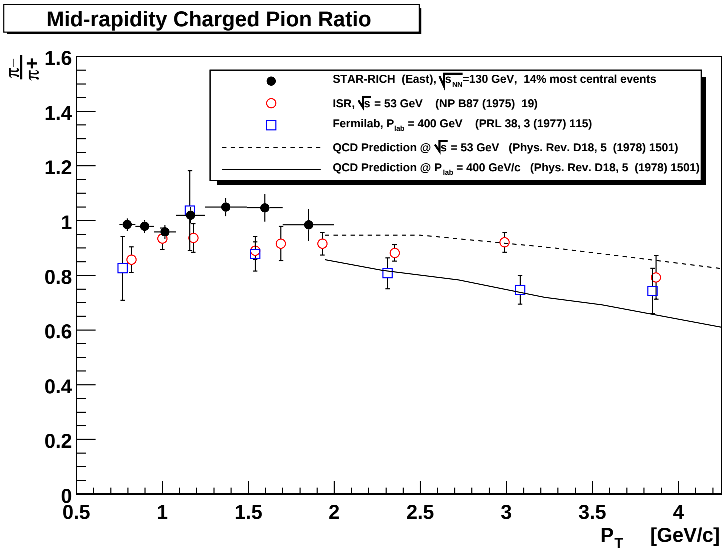

Figure 5.12: $\frac{\pi^-}{\pi^+}$ vs $p_\perp$. The ratio reported in this thesis is compared with data and theoretical calculations for pp collisions at two different values of $\sqrt{s}$.

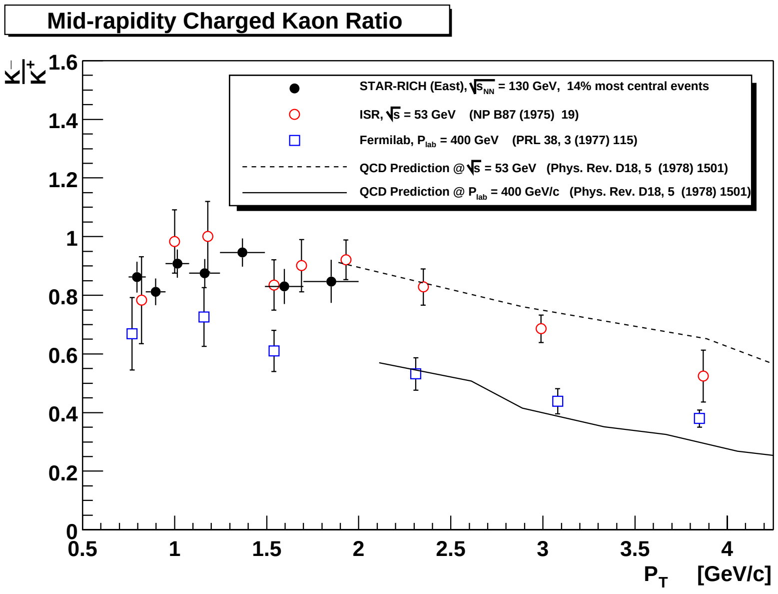

Figure 5.13: $\frac{K^-}{K^+}$ vs $p_\perp$. The ratio reported in this thesis is compared with data and theoretical calculations for pp collisions at two different values of $\sqrt{s}$.

For a fixed value of $\sqrt{s}$, the gluonic contribution decreases rapidly with increasing $p_\perp$, leaving the quark-quark scattering contribution the dominate one at high $p_\perp$. Thus the charged particle ratios at the $\sqrt{s_{NN}}$ attainable at RHIC should tend to stay flat as long as gluon scattering dominates. The ratios are expected to drop only when the quark-quark scattering term increases in importance. This behavior of the charged particle ratios is explained in [65],

> "For fixed p_T, the increasing importance of the gluonic contributions for larger $\sqrt{s}$ is due to the decrease in the effective value of $x_T = 2p_T/\sqrt{s}$, thereby probing smaller regions of x, ..., where the gluon distribution increasingly dominates over the quark distributions."

Thus one expects gluon scattering to be the dominant contribution to the charged particle ratios at the high center of mass energies reached at the RHIC collider. Interpreting the charged particle ratios presented in this thesis as resulting from a simple superposition of nucleon-nucleon collisions, one expects the charged particle ratios to be close to unity, and to remain flat out to a higher $p_\perp$, as explained in [65],

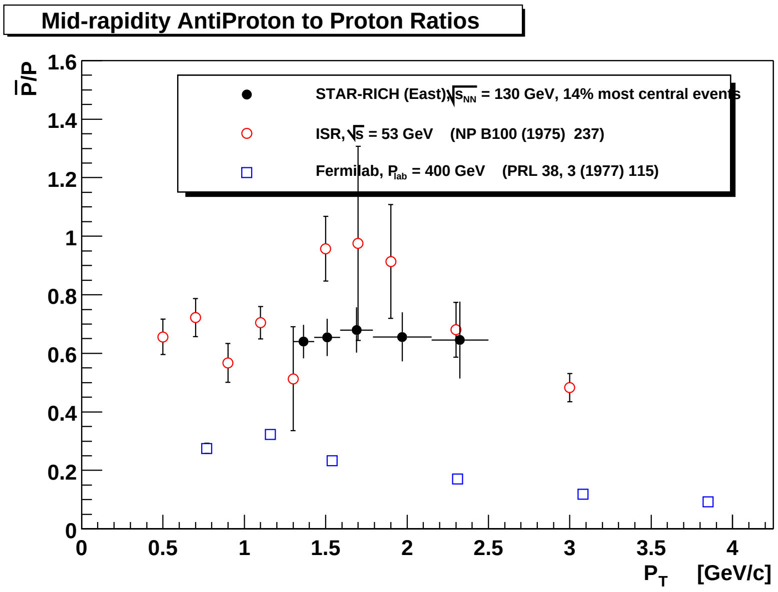

Figure 5.14: $\frac{\bar{P}}{P}$ vs $p_\perp$. The ratio reported in this thesis is compared with data and theoretical calculations for pp collisions at two different values of $\sqrt{s}$. No Iso-spin correction has been applied to the pp data (which would reduce the ratio value approximately 15%).

> "The energy dependence shown by the π^+/π^- and K^+/K^- ratios is easy to understand since both the data and the model curves approximately scale in x_T."

The relatively flat values reported for the ratios at low values of $p_\perp$ as measured at the lower center of mass energies (ISR and Fermilab) can be predicted to remain flat for RHIC measurements out to larger values of $p_\perp$. Compared to the ISR data points, one expects the RHIC ratios to remain flat out to a $p_\perp$ approximately 2-3 times as great as seen at the ISR. The charged particle ratios presented in this thesis are consistent with this expectation.

Nuclear Expectations

This behavior predicted by perturbative QCD differs from what is expected from statistical models, where a constant ratio is predicted for all momenta. This predicted constant ratio as a function of $p_\perp$ is a result of the small mass differences between the differently charged particles making up each particle species studied in this thesis. Naively, the particle production mechanism is expected to follow an exponential distribution in the particles transverse mass, $m_\perp = \sqrt{p_\perp^2 + m^2}$, leading to a flat dependence on $p_\perp$ for particles of similar mass.

In a nuclear environment, perturbative QCD predicts a rising value for the charged pion ratio, $\frac{\pi^-}{\pi^+}$, as a function of $p_\perp$, starting from a value of ~ 1 and eventually saturating at a value of ~ 1.14 for Au-Au. The value of 1.14 corresponds to the initial isospin imbalance of a Au-Au heavy ion reaction. To understand this, it is useful to appeal to pp collision phenomenology. The particle production in pp collisions at low momentum is dominated by non-perturbative physics, and as such cannot, as yet, be described in a fundamental way. Phenomenological models, such as a string model coupled with a LUND type hadronization scheme, exist which successfully describe most aspects of the particle production at these low momenta. In a collision involving two beam quarks, a color field is established which is confined in a narrow tube-like region (string) connecting the two quarks. The string will fragment via $q\bar{q}$ production, predominately forming mesons. The production of up-,down-, and strange-quarks is determined by the probability of the quark to tunnel out of the vacuum. The small mass difference between the up- and down-quarks then results in a charged pion ratio of 1 at low momentum. As the $p_\perp$ of the meson increases, perturbative effects become an increasingly important part of the particle production, eventually dominating the non-perturbative component. Thus, interpreting a Nucleus-Nucleus collision in terms of a simple superposition of nucleon-nucleon collisions, one expects a charged pion ratio $\frac{\pi^-}{\pi^+} \sim 1$ at low $p_\perp$ which then smoothly increases to a saturation value of 1.14 at high $p_\perp$. In a similar fashion perturbative QCD predicts a dropping value as a function of $p_\perp$ for the $\frac{\bar{P}}{P}$ and $\frac{K^-}{K^+}$ ratios in a nuclear collision.

Particle production in nucleon-nucleon collisions has been described in a two-component model[66, 67], where it is assumed that the events can be separated into those with and without (semi-) hard scatterings. The different physics involved in the two event classes is separated by a momentum cut-off scale, p_0. In the past this cut-off scale was believed to be independent of energy, and it is only recently[68] that evidence has been reported that supports both an energy and nuclear dependence,

$p_0(\sqrt{s}, A)$. The charged particle ratios presented in this thesis ($\frac{\pi^-}{\pi^+}, \frac{K^-}{K^+}, \frac{\bar{P}}{P}$ in Figures 5.1, 5.3, 5.5) show no dependence on the particle's transverse momentum over the currently measured range, with the possible exception of $\frac{\bar{P}}{P}$. Results similar to those reported here have been obtained with AA collisions recorded at lower center of mass energies. The CERES collaboration measured the charged pion ratio[69] in 158 AGeV/c Pb-Au collisions. The $\frac{\pi^-}{\pi^+}$ ratio was measured out to a transverse momentum of 2.2 GeV/c and was found to be constant over the entire momentum interval. This constancy of the measured charged particle ratios with $p_\perp$ is an indication that hard scattering does not dominate the collision dynamics below $\sim$ 2 GeV/c, and would seem to set a lower bound for $p_0 \gtrsim$ 2 GeV/c.

Nuclear effects on Perturbative Spectra

There is a long history of predicting the behavior of fast partons propagating through the dense matter formed during a heavy ion collision, starting with Bjorken [70] in 1982 where he predicted a suppression of high p_T particles in heavy ion collisions due to the energy loss via elastic scattering of fast partons travelling through a QGP. The magnitude of this energy loss has been estimated [13, 71, 72] to be modest, $\frac{dE_{el}}{dx} \sim 0.2 - 0.3\ GeV/fm$. In addition to energy loss via elastic scattering, the transverse momentum imbalance (acoplanarity) of a jet pair produced in a QGP was investigated [73, 74]. Pairs of fast partons initially produced back-to-back in the dense matter undergo elastic scattering off the QGP constituents as they propagate, leading to the expectation of a reduction in the jet acoplanarity relative to that found in pp and $p\bar{p}$ collisions [75, 76]. In a paper published subsequently [77], it was shown that experimental effects ignored in [73, 74], (such as hadronic backgrounds), lead to a serious reduction in the usefulness of jet acoplanarity as a probe of partonic energy loss in dense matter.

In addition to energy losses due to elastic scattering it is expected that radiative energy losses should also play a role. This induced soft gluon bremsstrahlung associated with multiple collisions [78, 79] has been estimated [71] to be much larger in magnitude than that due to elastic scattering. This has then led to a great effort to understand the non-abelian nature of this energy loss and its effects on particle spectra at high transverse momenta [80, 81, 82, 83, 84, 85, 86, 87, 88, 89, 90, 91, 92, 93, 94]. The angular dependence[84, 95] of the gluon bremsstrahlung results in a nearly collinear emission spectrum with the induced radiation confined within a small angular region surrounding the fast parton. The fast parton will ultimately be associated with a hadronic jet measured in the lab. The particles contained in this hadronic jet will have originated from both the hadronization of the fast parton as well as from the hadronization of the radiated gluons. Because of this, the number of particles found within the jet will generally increase relative to the case of no energy loss and are expected to show a reduction in their average transverse momentum. The total energy of the jet however, is expected to remain fairly constant, as the gluons are radiated in a nearly collinear fashion resulting in particle production largely contained within the original jet cone. The resulting modification to the jet fragmentation function has been suggested as a means of measuring, in an indirect manner, the energy loss of the fast parton[96, 97]. The proposed method relied on measuring the high p_T particle distribution in the opposite direction of a high energy photon. In the same paper[96] the feasibility of making such a measurement was studied and shown to be very poor at the luminosities and collision energies achievable at RHIC. In an alternative approach taken in [93], the single particle spectrum at high p_T is used to study the partonic energy loss. Fast partons will lose energy in the medium which will result in a reduction of the number of particles seen at high p_T. This leads to a prediction of the suppression of high p_T particles propagating through a QGP and has received much attention[90, 91, 92]. In a similar fashion, the charged particle ratios are a gauge of the flavor dependence[90] of the predicted partonic energy loss experienced by the fast partons and as such offer a stringent test of the proposed models.

In the initial development of the field, predictions made by different theorists typically differed in the functional form of the predicted energy loss, resulting in significant differences in the expected energy loss. None, however, was able to accurately describe the results obtained from the moderately high transverse momentum spectra at the CERN SPS[91, 98] which were suggestive of no measurable energy loss at all, $dE/dx \lesssim 0.01$ GeV/fm. This was in direct contrast with the predicted partonic energy loss of $dE/dx \sim 1$ GeV/fm and essentially remained a mystery until recent theoretical calculations[82] showing the importance of including effects such as re-scattering of the gluon bremsstrahlung, finite gluon formation times, and realistic jet kinematics. The previously predicted value of an average $dE/dx \sim 1$ GeV/fm for the partonic energy loss was made assuming asymptotic jet energies occurring in static, infinite nuclear matter. This was subsequently shown to be unrealistic for nuclear collisions at SPS energies. The number of interactions a fast parton is expected to suffer as it propagates through the excited nuclear matter created in an SPS Pb-Pb collision was estimated to be very small, on the order of 1-2. In addition, the inclusion of realistic jet energies when calculating the energy loss was shown to be crucial, where the asymptotic assumption led to a large over-estimation in the energy loss expected at the SPS. At the higher collision energies available at the RHIC collider, these short comings are much reduced in magnitude. The number of interactions a fast parton can be expected to suffer is estimated to be somewhere between 4-10 and the asymptotic assumption is expected to lead to a smaller over-estimation in the predicted energy loss. In [99], an estimation of the partonic energy loss in central collisions was made using the preliminary RHIC data and was suggestive of significant energy losses. The flavor dependence of this energy loss is measurable via the $p_\perp$ dependence of $\frac{\bar{P}}{P}$. This can be understood in the following argument. Gluons have a higher color charge as compared to quarks, and as such are expected to lose more (~ 2) energy in deconfined matter. Gluons show no preference for Protons or Antiprotons upon fragmentation, whereas quarks will preferentially fragment into Protons. Thus Antiprotons are expected to be more sensitive to the partonic energy loss than Protons. The anti-proton to proton ratio is expected to be reduced in value when compared to the corresponding ratio in pp collisions at sufficiently high $p_\perp$ due to this partonic energy loss.

Other nuclear effects like nuclear shadowing are likewise expected to play a role in the reduction of the ratio when going from pp to Au-Au collisions. Mini-jet production is thought to play a major role in the particle production at the center of mass energies achieved at RHIC and is calculable using perturbative QCD calculations. However, it is necessary to understand the incoming parton distribution to make reliable predictions of the initial mini-jet production. These parton distributions depend in a sensitive way on the transverse momentum transfer, Q, and the $\sqrt{s}$ of the collision, and are typically described using the kinematic variables x and Q. For a momentum transfer $Q \sim p_\perp = 2$ GeV/c, the corresponding value of $x_\perp = \frac{2p_\perp}{\sqrt{s}} \sim 0.03$. At these small values of $x_\perp$, it is expected that the gluon distribution will be dominant over the corresponding quark distribution in a nucleon. Deep-inelastic scattering experiments at HERA [100] indicate that the parton distribution in nuclei at small x is not simply A times the nucleon distribution. The parton distribution for nuclei is reduced relative to what is expected from a simple superposition of the parton distribution functions obtained from nucleons. This is typically referred to as shadowing, and essentially results in a reduction of the jet cross section at small x. Modelling a heavy ion collision as a linear superposition of individual nucleon-nucleon collisions thus requires modelling this shadowing. These effects are non-perturbative in nature and their effects on the ratio have to be modelled, as in a Monte-Carlo type calculation.

5.4 Comparison with Models

The usefulness of comparing Nucleus-Nucleus data with similar measurements obtained in Nucleon-Nucleon collisions is largely limited to the physics associated with Nucleon-Nucleon collisions. The theoretical concepts currently used to predict the physics of a high energy Nucleus-Nucleus collision, (such as QGP formation, jet quenching, elliptical flow, etc...), differ in many respects from those used to describe the behavior of Nucleon-Nucleon collisions. To address the physics predicted in Nucleus-Nucleus collisions, models have been developed which incorporate one or more of these ideas into a framework used to describe a Nucleus-Nucleus collision. Many times these models are implemented in terms of a Monte Carlo type calculation, leading to definite predictions for many of the observables used to characterize heavy ion collisions. In this section, comparisons of the measured charged particle ratios will be made with predictions of various models used to describe relativistic heavy ion collisions. One of these models, HIJING, incorporates partonic energy loss effects along with a momentum independent cut-off scale, p_0, separating the hard and soft physics involved in a hadronic collision. Predictions made by other models which attempt to describe the nuclear collision without perturbative elements, such as UrQMD, will also be compared to the data. In addition, the measured particle ratios can be interpreted in a statistical way, such as in the context of a thermodynamical model. While the thermodynamical models predict no $p_\perp$ dependence for the measured particle ratios presented in this thesis, definite relations between the various ratios are predicted and can be tested. This will be done using a thermodynamical model described in ref [10, 101].

5.4.1 Monte Carlo Models

Heavy Ion Jet INteraction Generator (HIJING and HIJING/B)

HIJING attempts to model pp, pA and AA collisions using a perturbative QCD inspired model to account for minijet production, thought to play a major role in the high energy Nucleus-Nucleus collisions at the RHIC collider and the upcoming CERN LHC experiments. The hard and soft physics involved in the hadronic collisions are separated using a two-component model with a constant cut-off parameter, $p_0 = 2$ GeV/c. Nuclear collisions are simulated by assuming nucleus-nucleus collisions can be modelled as a series of binary nucleon-nucleon collisions together with a Glauber model of the nuclear collision geometry. The probability of interaction for each binary collision is then calculated, along with the number of produced minijets which are modelled using pQCD. The energy carried off by the hard scattered partons is then subtracted and the remaining energy is used to form an excited string state to model the soft physics. The excited string is allowed to undergo further collisions using a geometrical probability, the possibility of becoming de-excited is allowed as well. Upon fragmentation, the produced hadrons are assumed to not interact with any other strings or nearby hadrons, i.e. multiple scattering effects at the hadronic stage are not simulated. Model parameters were tested against pp data. The extrapolations up to AA collisions require modifications due to nuclear effects, like parton shadowing and jet quenching. A parameterized parton distribution function is used to account for nuclear shadowing, along with a constant dE/dx for jet quenching.

Baryon stopping is described using a diquark-quark hadronic string configuration. This mechanism, responsible for the baryon number transport from the beam rapidity to mid-rapidity, was seen to significantly under-predict the baryon stopping as measured at the SPS[57]. A modified version of HIJING exists, HIJING/B, which incorporates a baryon junction mechanism (see subsection 5.3 for description of the baryon junction) to model the baryon stopping.

Ultra-relativistic Quantum Molecular Dynamics (UrQMD)

The UrQMD model attempts to describe a heavy ion collision at high energy using hadronic degrees of freedom, the hadrons follow classical trajectories using relativistic kinematics. A nucleon contained in one of the two incoming nuclei is described with a Gaussian shaped density profile. The Gaussian centers of these nucleons are distributed in a random fashion within the nucleus. Collisions occur when two hadrons come within a certain minimum distance, d_0, which depends on the $\sqrt{s}$ of the collision, as well as the hadron species and quantum numbers involved. For interactions taking place at high center of mass energies, typically in the initial stages of the nuclear collision, string excitations are used to describe the hadron interactions, with their subsequent fragmentation leading to the creation of additional hadrons within a certain formation time. During this formation time, the leading hadrons are described with a reduced cross section. Newly formed hadrons created by string fragmentation are not allowed to interact during their formation time, which typically lasts 1-2 fm/c. This system of hadrons becomes meson dominated after a few fm/c and the interactions thereafter are described in terms of the creation of resonance states.

5.4.2 Statistical Models

While many of the models currently available (like those described above) attempt to describe a high energy heavy ion collision in terms of interactions involving individual nucleons, another class of models takes a different approach. The initial interaction between the two nuclei is not modelled, but is assumed to lead to the creation of a thermally equilibrated system in a sufficiently short period of time. Thereafter, the system is describable in terms of a thermodynamical model with the collective motion of the system governed by hydrodynamics. These statistical descriptions have been applied to a number of different colliding systems, with surprising success[102]. In Ref. [102], the hadronic multiplicities in e^+e^- collisions are assumed to originate from a thermally equilibrated hadron gas, and are well described in terms of a thermodynamical calculation.

In a fashion typical for the field, the densities of particles produced in heavy ion collisions can be calculated from the ideal gas expression relating the particle density n_i with a small number of model parameters, $\mu^B_{chem}, \mu^{\mathrm{S}}_{\mathrm{chem}}, \mu^{\mathrm{I}}_{\mathrm{chem}}$ and T_{chem},

$$n_i = \frac{g_i}{2\pi^2} \int_0^\infty \frac{p^2 dp}{exp\left[\left(E_i - \mu^B_{chem} B_i - \mu^S_{chem} S_i - \mu^I_{chem} I_i\right)/T_{chem}\right] \pm 1} \tag{5.5}$$

in addition to the variables for the hadron spin degeneracy factor g_i and the baryon number B, strangeness S, z-component of the isospin I, and energy E. The above equation 5.5 is used to calculate the number of particles of a particular species that are present at the time inelastic collisions cease, typically referred to as chemical "freeze-out". The model parameters μ^S_{chem} and μ^I_{chem} are the strangeness and isospin chemical potentials and are constrained by requiring strangeness and electric charge conservation. The remaining two parameters, μ^B_{chem} and T_{chem} then fully describe the chemical make-up of the system at chemical freeze-out. These parameters can be determined by constructing various particle ratios from the data. The chemical freeze-out temperature, T_{chem}, is predominately constrained by the pion/baryon ratio, which is most sensitive to the system temperature. This can be understood as resulting for the large mass difference between the pions and baryons. Production of particles with a particular mass in a thermal model depends sensitively on the energy available, which is related to the temperature of the system. The baryon chemical potential, μ^B_{chem}, is then determined by the anti-nucleon/nucleon ratio which is most sensitive to the baryon number composition of the system.

5.4.3 $P_\perp$ Dependence of Charged Particle Ratios: Model Predictions

In the following subsections, the UrQMD, HIJING and HIJING/B model predictions for the charged meson ratios, $\frac{\pi^-}{\pi^+}$, $\frac{K^-}{K^+}$, along with the Antibaryon-to-baryon ratio $\frac{\bar{P}}{P}$ will be presented together with the measured ratios reported in this Thesis. The model calculations were conducted using the code "as is", with the original settings found in the computer codes used whenever possible. The only exceptions to this were to change the collision centrality selection to correspond to the event sample used in this Thesis, and the collision energy. The centrality corresponds to the 15% most central events and roughly translates to an impact parameter distribution ranging from 0 to 5 fm. The impact parameter was chosen in a random fashion for the model calculations, with the probability of an event occurring at a particular impact parameter weighted in a quadratic fashion. The center of mass energy $\sqrt{s_{NN}}$ was set to the corresponding energy for the first years data set, $\sqrt{s_{NN}} = 130$ GeV. The calculated charged particle ratios are restricted to $\eta < 0.2$ to allow an easy comparison with the data.

Charged Pion Ratio

The prediction for the ratio of the charged Pions versus their transverse momentum for the various models is shown in Figure 5.15. The model calculations predict little to no dependence of the charged Pion ratio with transverse momentum from the lowest $p_\perp$ up to 4 GeV/c and are in both qualitative and quantitative agreement with the data. The similarity between the predictions made by the various models is not surprising given each model employs a string-like excitation to describe the initial interactions between the nucleons early in the collision between two nuclei. HIJING and its variant HIJING/B describe the particle production entirely in terms of string type excitations together with perturbative scattering terms. Hadrons formed from the string fragmentation are not allowed to re-interact with the surrounding matter, essentially "freezing out" after their initial formation from the string's decay. The UrQMD model differs from the HIJING(B) treatment in the way the hadrons are handled after their formation. In UrQMD, the system formed in a heavy ion collision is meson dominated early on in the collision. The mesons are allowed to interact, or "rescatter", with other hadrons in their vicinity, tending to flatten out the ratio. However, the small mass of the Pion allows for copious production in any reasonable model. The string fragmentation mechanism is modelled via quark tunnelling, and given the small mass difference between the two light quarks will produce a charged Pion ratio close to 1. This behavior is expected based on a simple extrapolation from nucleon-nucleon collisions as seen in Figure 5.12.

Charged Kaon Ratio

The prediction for the ratio of the charged Kaons versus their transverse momentum for the various models is shown in Figure 5.16. The models predict similar values for the charged Kaon ratio, which is expected as all the models incorporate a string-like

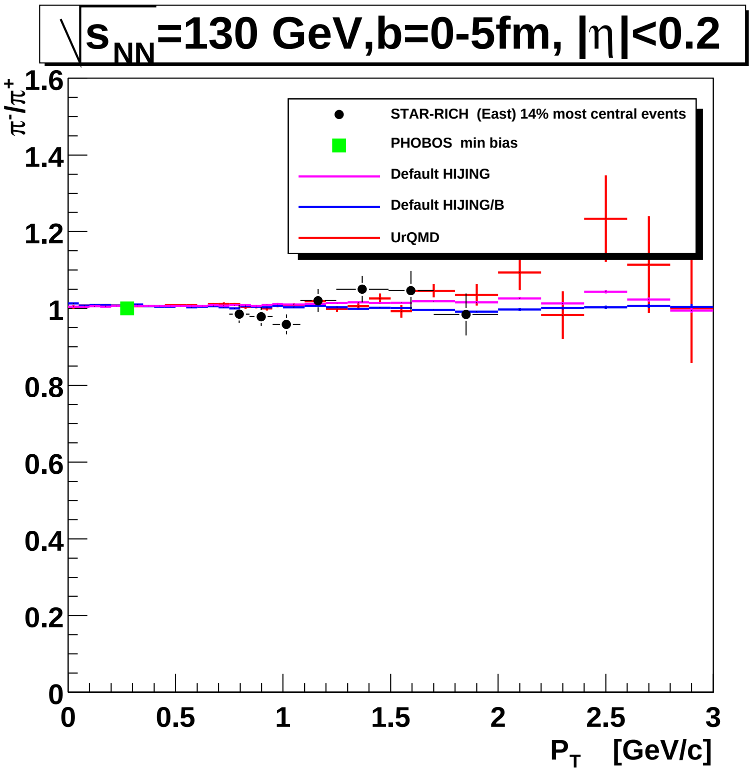

Figure 5.15: $\frac{\pi^-}{\pi^+}$ vs $p_\perp$. The ratio reported in this thesis is compared with various model calculations for Au+Au collisions at $\sqrt{s_{NN}} = 130\text{GeV}$.

excitation to describe the nucleon-nucleon interactions at the high $\sqrt{s_{NN}}$ achieved by the RHIC collider. The model calculations predict a constant value for the ratio of approximately 0.9 for $p_\perp \lesssim 1$ GeV/c. Beyond a $p_\perp$ of 1 GeV/c, the models show a modest dependence of the ratio with transverse momentum, reaching a value of ~ 0.8 at $p_\perp = 2$ GeV/c. The models are in excellent agreement with the data at the lowest $p_\perp \lesssim 1$ GeV/c. The $p_\perp$ dependence of the data is consistent with a constant value out to the highest $p_\perp$ reported in this thesis for the charged Kaon ratio, which is different from the model predictions of a falling ratio. However, the large uncertainty in the individual data points results in only a small discrepancy on the order of $\lesssim 1\ \sigma$ between the various model predictions and data, effectively disallowing any distinction to be made between the various models.

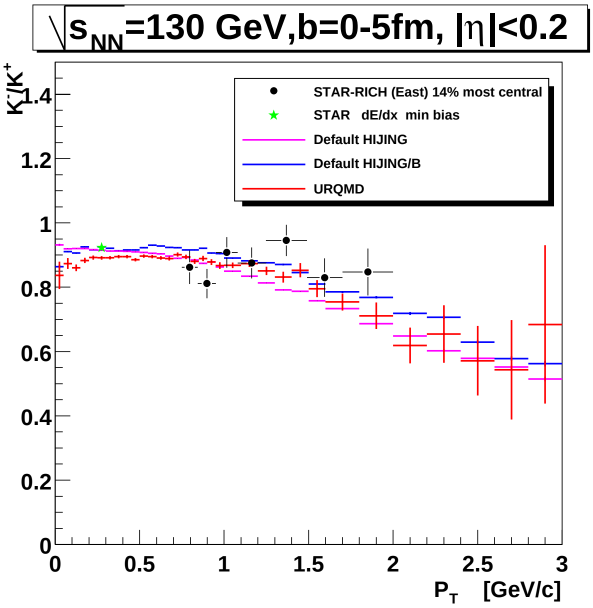

Figure 5.16: $\frac{K^-}{K^+}$ vs $p_\perp$. The ratio reported in this thesis is compared with various model calculations for Au+Au collisions at $\sqrt{s_{NN}} = 130$ GeV.

Antiproton-to-Proton Ratio

The prediction for the $\frac{\bar{P}}{P}$ ratio for the various models is shown in Figures 5.17,5.18 and 5.19 together with STAR data points. In contrast with the model predictions for the charged meson ratios, significant differences exist between the model calculations for the η and $p_\perp$ dependencies of the $\frac{\bar{P}}{P}$ ratio. In Figure 5.17 the $\frac{\bar{p}}{p}$ ratio as calculated by HIJING, HIJING/B and UrQMD is plotted versus η together with the STAR dE/dx data point [53]. The HIJING model significantly over-predicts the $\frac{\bar{p}}{p}$ ratio by ∼30%. Describing the baryon production using the baryon junction mechanism via HIJING/B results in a much smaller discrepancy between the data and model calculation of ∼15%. However, making a transverse momentum comparison between the data and the model calculations highlights the different physics involved in the model calculations (Figure 5.18). At the low end of the $p_\perp$ scale HIJING predicts a constant value for the $\frac{\bar{P}}{P}$ ratio of ~ 0.8 out to a $p_\perp \lesssim 1$ GeV/c. This high value is typical for string-type models, which predict a $\frac{\bar{P}}{P}$ ratio of approximately 0.9 for nucleon-nucleon collisions at RHIC's high center of mass energies. These high values predicted for the ratio are an indication that the quark-diquark string fragmentation employed in these models is not sufficient to describe the stopping, necessitating the introduction of new

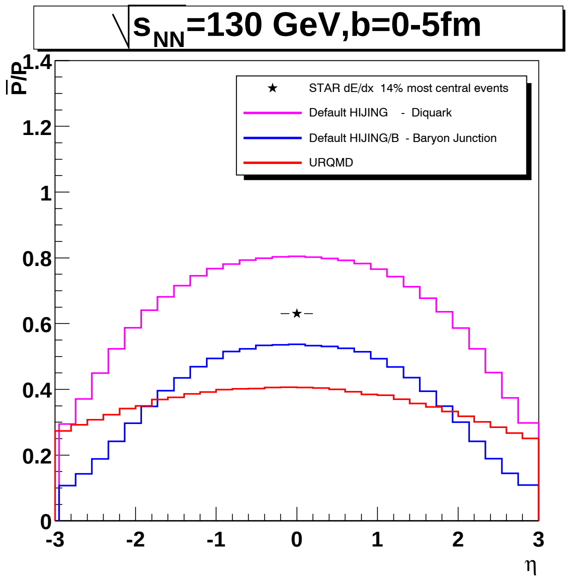

Figure 5.17: $\frac{\bar{P}}{P}$ vs η. The STAR dE/dx ratio integrated over $p_\perp$ is compared with various model calculations for Au+Au collisions at $\sqrt{s_{NN}} = 130$ GeV. Error bars are statistical only.

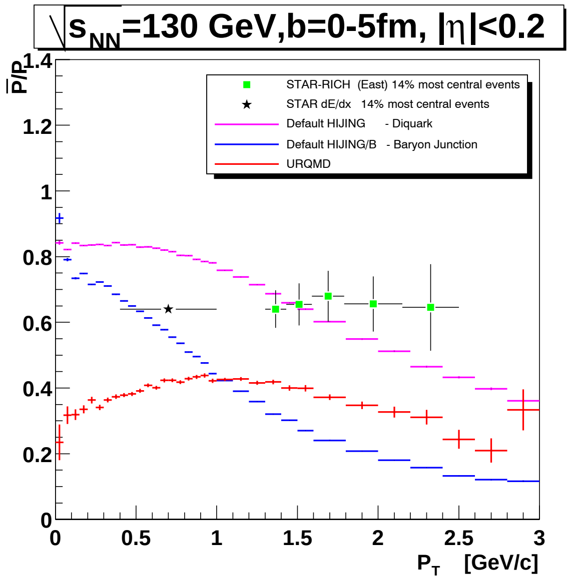

Figure 5.18: $\frac{\bar{P}}{P}$ vs $p_\perp$. The ratio reported in this thesis is compared with various model calculations for Au+Au collisions at $\sqrt{s_{NN}} = 130$ GeV. Error bars are statistical only.

physics to properly take into account the stopping. HIJING/B describes the baryon stopping entirely in terms of a baryon junction stopping mechanism. With the inclusion of the baryon junction, HIJING/B predicts a lower value for the mid-rapidity $\frac{\bar{P}}{P}$ ratio of ∼0.5. While both HIJING and HIJING/B are in disagreement with the established RHIC average of $\frac{\bar{P}}{P} = 0.63 \pm 0.03$ (see Table 5.2.3), the introduction of the baryon stopping mechanism brings the predicted ratio closer to the measured ratio. However, a comparison of the transverse momentum dependence of the ratio as determined by model calculation and with the ratio measured by STAR (both dE/dx and RICH) shows a significant difference in the ratio predicted by HIJING/B and the data which grows with $p_\perp$. At 2 GeV/c, this leads to a greater than 3 σ discrepancy between the HIJING/B prediction and the data. At high $p_\perp$, HIJING predicts a dropping value of the ratio for $p_\perp \gtrsim 1$ GeV/c and would seem to be contradicted by the data, which is consistent with a constant value for $p_\perp \lesssim 2.5$ GeV/c. However, the large uncertainties in the measured data points disallows any such conclusion. For $p_\perp$ values greater than $\sim$ 1 GeV/c, the HIJING calculations are all within 1σ of the measured data points.

UrQMD calculations show a behavior entirely different from the trend established by data. The $\frac{\bar{P}}{P}$ ratio is predicted to be $\sim$ 0.3 at the lowest $p_\perp$ and rise in a linear fashion to 0.45 at a $p_\perp$ of $\sim$ 1 GeV/c. For $p_\perp$ higher than this UrQMD predicts a gradual dropping of the ratio, eventually reaching a value of $\sim$ 0.3 at $p_\perp = 2$ GeV/c. The near linear increase of the ratio for $p_\perp$ less than 1 GeV/c is a direct result of the rescattering experienced by the hadrons in the UrQMD treatment of the collision. The initial production of particles is described in terms of string excitations, which are allowed to decay within a few fm/c and rescatter with any nearby hadrons. Without rescattering, a $\frac{\bar{P}}{P}$ similar to HIJING is expected. However, due to the rescattering modelled by UrQMD, the Antiprotons are likely to suffer annihilation through the numerous collisions experienced by the Antiproton in the dense system formed during the collision. This leads to a significant reduction of the ratio, resulting in the $\frac{\bar{P}}{P}$ ratio being close to 0.3. The behavior of the $\frac{\bar{P}}{P}$ ratio at low $p_\perp$ is a result of the transverse momentum dependence of the Antiproton's annihilation cross section. The annihilation cross section for the Antiproton is a rapidly changing function[103] of

$p_\perp$, showing an almost linear decrease for $p_\perp \lesssim 5$ GeV/c. Thus, with increasing $p_\perp$, the Antiproton is less likely to suffer annihilation, leading to the increase in the $\frac{\bar{P}}{P}$ with $p_\perp$. Beyond 1 GeV/c, the $\frac{\bar{P}}{P}$ ratio plateaus and eventually begins to drop in a fashion similar to HIJING.

Nuclear Effects on $\frac{\bar{P}}{P}$ ratio

HIJING (and its variant HIJING/B) attempt to describe a relativistic heavy ion collision in terms of a linear superposition of nucleon-nucleon collisions. Nuclear effects such as partonic energy loss and shadowing are included in the model calculations and have important consequences for the predicted particle yields at high and low $p_\perp$, respectively. To model the partonic shadowing, HIJING employs the Duke-Owens (DO) [104] parameterization of the parton distribution functions (pdf) together with a model dependent shadowing parameter. However, it was recently[100] shown that the DO pdf underestimates the gluon distribution at small x and leads to a significant reduction in the number of gluons at small x as compared to that expected from [100]. For a fast ($p_\perp > p_0 = 2$GeV/c) gluon, HIJING models the energy loss using a constant degradation of the gluon's energy with its distance travelled through the deconfined matter, $\left(\frac{dE}{dx}\right)_g = 2$ GeV/fm. Quarks, having a smaller color charge than gluons, are assumed to lose only 1/2 this energy. In light of recent findings [99], this is thought[105] to be too high and a more likely value would be closer to $\left(\frac{dE}{dx}\right)_g \sim 0.5$ GeV/fm.

In Figure 5.19, HIJING predictions for the transverse momentum dependence of the $\frac{\bar{P}}{P}$ ratio are shown together with the data collected by STAR. The default version of HIJING (shown in red on Figure 5.19) is made using a value of $\left(\frac{dE}{dx}\right)_g = 2$ GeV/fm for the energy loss of a gluon and includes a modification to the parton distribution functions at small x due to shadowing. In addition to the calculation using the default model parameters, two calculations are shown which have a single parameter changed to ascertain the effect of the partonic energy loss and nuclear shadowing parameters separately. The effect of the partonic energy loss on the HIJING prediction for the $\frac{\bar{P}}{P}$ ratio can be seen in Figure 5.19 by comparing the calculations made with (in purple) and without (in green) partonic energy loss and shows a $\sim 30\%$ difference in the

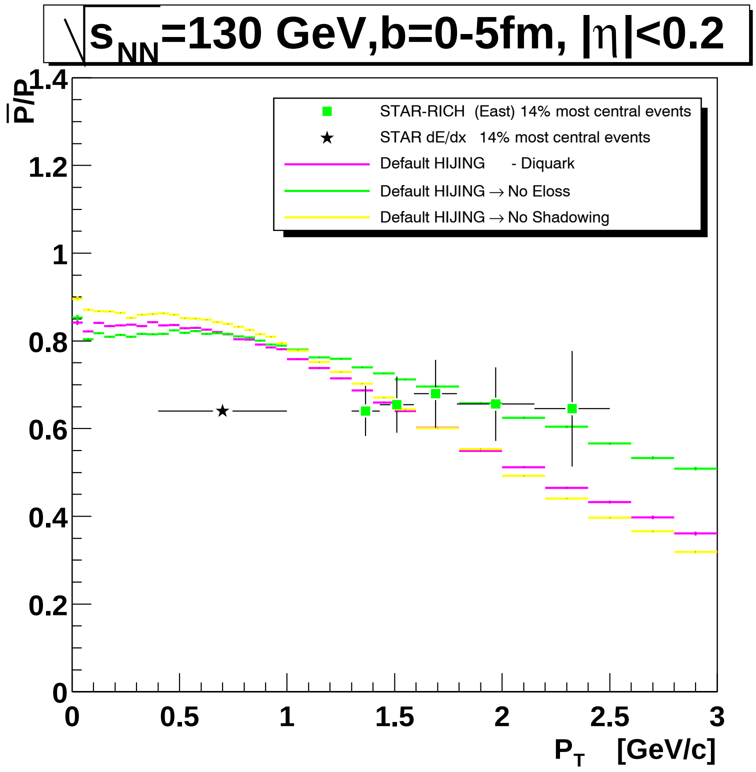

Figure 5.19: $\frac{\bar{P}}{P}$ vs $p_\perp$. The ratio reported in this thesis is compared with various model calculations for Au+Au collisions at $\sqrt{s_{NN}} = 130$ GeV.

ratio at a $p_\perp = 2.5$ GeV/c. The effect of the shadowing can be seen by comparing the default HIJING (in yellow) calculation which has both shadowing plus partonic energy loss, with the calculation which has only the partonic energy loss included, and no shadowing (in purple). For low $p_\perp \lesssim 1$ GeV/c, shadowing results in a $\sim 5\%$ reduction of the ratio as expected. Shadowing essentially reduces the number of gluons at small x and thus reduces the Antiproton yields from gluon fragmentation at these small momenta. At the higher $p_\perp$= 2.5 GeV/c shadowing results in a $\sim 5\%$ increase of the ratio.

A comparison of the HIJING predictions with the data collected by the STAR-RICH (Figure 5.19) at high $p_\perp$ indicates that the data favors model parameters for the energy loss much smaller than the default value of 2.0 GeV/fm used in the HIJING model calculations. This is in line with the much lower parameter value $\sim$ 0.5GeV/fm advocated by Gyulassy in [105]. The large uncertainties in the data points in the high $p_\perp$ range covered by the STAR-RICH measurements presented in this thesis makes it impossible to make a definite statement on the HIJING model predictions of the flavor dependence of the partonic energy loss. It is interesting to note that the inclusion of the baryon junction to account for the stopping seen in pp and Au+Au collisions results in a dramatic decrease in the $\frac{\bar{P}}{P}$ versus $p_\perp$. At the higher values of $p_\perp \gtrsim$ 2GeV/c where the perturbative calculations are expected to be reliable, the difference between the HIJING and HIJING/B calculations is $\sim 60\%$. HIJING describes the proton (and anti-proton) production entirely in terms of diquark breaking plus a perturbative component. HIJING/B, on the other hand, employs the baryon junction to account for the baryon stopping (along with the same perturbative elements as HIJING) with no contribution from diquark breaking. It is likely that a combination of diquark breaking + baryon junction stopping mechanisms will be needed to fully account for the measured $\frac{\bar{P}}{P}$ ratio. It is then likely that the measured $\frac{\bar{P}}{P}$ ratio would be describable without the need to invoke any partonic energy loss effects by mixing the appropriate amount of baryon junctions with the conventional string dynamics to describe the baryon yields at mid-rapidity. This emphasizes the need to better understand the dynamics of the baryon junction stopping at the low $p_\perp$ to fully understand the baryon yields at high $p_\perp$.

Thermal Model Calculations

Statistical analyses of heavy ion collisions have been applied in the past with great success for systems involving heavy ions [106, 107, 108] at the SPS as well as in elementary particle collisions [102]. In [101], charged particle ratios measured at RHIC at $\sqrt{s_{NN}} = 130$ GeV by the four experiments were interpreted in terms of a thermal model. The model has two free parameters (T_{chem}, μ_B) which were varied to obtain the best fit to the data yielding $T_{chem} = 174 \pm 7$ MeV and $\mu_B = 46 \pm 6$ MeV. In [101] 9 particle ratios are used to arrive at this conclusion and are listed here, $\frac{\bar{P}}{P}$, $\frac{\bar{\Lambda}}{\Lambda}$, $\frac{\bar{\Xi}}{\Xi}$, $\frac{\pi^-}{\pi^+}$, $\frac{K^-}{K^+}$, $\frac{K^-}{\pi^-}$, $\frac{\bar{P}}{\pi^-}$, $\frac{\bar{K}^{*0}}{h^-}$ and $\frac{K^{*0}}{h^-}$. The different ratio's have varying influences on the fit parameters based on their masses and quantum numbers as expressed in the

Boltzmann approximation to the ratio in eq. 5.6

$$\frac{n_1}{n_2} \sim \frac{g_1}{g_2}\left(\frac{m_1}{m_2}\right)^{3/2}\frac{e^{(\mu_1-m_1)/T}}{e^{(\mu_2-m_2)/T}}. \tag{5.6}$$

where $\mu_i = \mu_B B_i - \mu_S S_i - \mu_I I_i$ and g_i is the spin-isospin degeneracy factor. In Figures 5.20 and 5.21 the sensitivity of the charged particle ratios presented in this thesis to the system temperature and baryon chemical potential at freeze-out are shown. The charged Pion ratio proves to be rather insensitive to the system temperature and baryon chemical potential. However, in Figures 5.20 and 5.21, the system's chemical potential is tightly constrained by both the charged Kaon ratio as well as the Antiproton-to-Proton ratio. In addition to constraining the system's baryon chemical potential, the Antiproton-to-Proton ratio proves to be sensitive to the system's

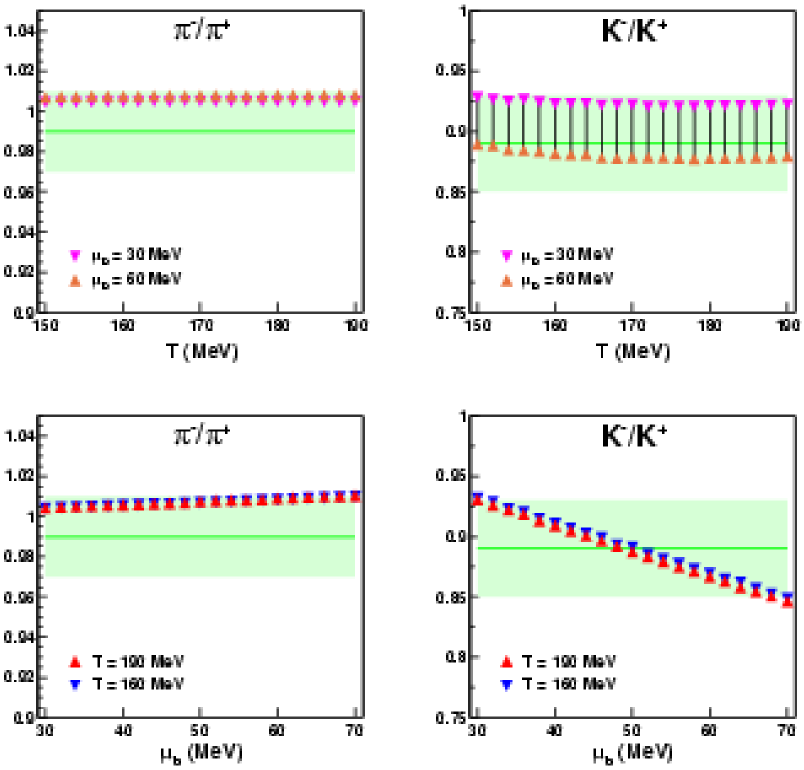

Figure 5.20: Thermal Analysis of Meson Ratios. Charged Kaon ratio is sensitive to the baryon chemical potential. Figures obtained from ref. [10].

temperature. From the best fit model parameters for the temperature and chemical potential, the model yields the following values for the ratios: $\frac{\pi^-}{\pi^+} = 1.007$, $\frac{K^-}{K^+} = 0.894$, and $\frac{\bar{P}}{P} = 0.63$. These values agree with the ratio values reported in this thesis. In the same paper, the systematic variation of the T_{ch} and μ_{ch} parameters with the $\sqrt{s_{NN}}$ is investigated, using data from the AGS, SPS and RHIC. It is found that the temperature and chemical potential vary in a smooth way from the AGS all the way to the RHIC center of mass energies, and allows an extrapolation to $\sqrt{s_{NN}} = 200$ GeV. At this energy, the system's temperature and chemical potential at freeze-out are expected to be $T_{ch} = 177 \ \pm\ 8\ MeV$ and $\mu_{ch} = 29\ \pm 6\ MeV$. This allows a prediction to be made for the particle ratios, $\frac{\pi^-}{\pi^+} = 1.004$, $\frac{K^-}{K^+} = 0.932$, and $\frac{\bar{P}}{P} = 0.752$.

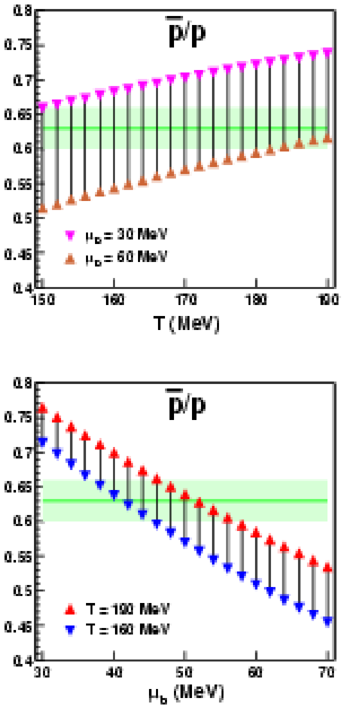

Figure 5.21: Thermal Analysis of Antiproton-to-Proton Ratio. Ratio is sensitive to baryon chemical potential and the system temperature at Chemical Freeze-out. Figures obtained from ref. [10]

Chapter 6

Conclusions

The ratios of the identified charged hadrons $\frac{\pi^-}{\pi^+}$, $\frac{K^-}{K^+}$ and $\frac{\bar{P}}{P}$ created in Au+Au collisions at $\sqrt{s_{NN}} = 130$ GeV have been studied, and their behavior with respect to transverse momentum investigated. All of the ratios presented in this work are consistent with a constant value, independent of the transverse momentum at which the ratio measurement was made.

The $\frac{\bar{p}}{P}$ ratio presented in this work indicates that the net-baryon yield at RHIC is much smaller than has been achieved in earlier heavy ion experiments at the SPS and AGS, and that pair production processes dominate over baryon number transport at this $\sqrt{s_{NN}}$. Comparisons of the Antiproton-to-Proton ratio presented in this work with the HIJING and HIJING/B models illustrates the need to better understand baryon production at mid-rapidity. Inclusion of the baryon junction mechanism to describe the baryon production at mid-rapidity results in a significantly better description of the data when integrated over transverse momentum. However, a comparison of the baryon junction prediction for the $\frac{\bar{p}}{p}$ ratio versus $p_\perp$ reveals significant discrepancies between the model calculation and the data and is an indication that the baryon junction mechanism does not describe well the underlying physics responsible for the baryon production at mid-rapidity.

The charged meson ratio $\frac{K^-}{K^+}$ along with the Antibaryon-to-Baryon ratio $\frac{\bar{P}}{P}$ are sensitive to the net baryon density which is associated with the baryochemical potential created in a heavy ion collision. Thermodynamical QCD predictions[101] for the charged particle ratios are consistent with the measured values for the ratios presented in this work, and give a measure of the system's temperature and baryochemical potential at chemical freeze-out, $T_{chem} = 174 \pm 7$ MeV and $\mu_B = 46 \pm 6$ MeV. The temperature at chemical freeze-out is similar to that seen in earlier heavy ion experiments at the SPS. However, the baryochemical potential measured in Au+Au collisions at $\sqrt{s_{NN}} = 130$ GeV is much smaller that the corresponding value measured at the SPS and is an indication that the net baryon density achieved at RHIC is much smaller than has been previously measured. The agreement between the measured ratios and those predicted by thermodynamical QCD is an indication that chemical equilibrium has been achieved in the course of the collision. The origin of this apparent chemical equilibrium remains in doubt however. In [101] it is thought that the hadronic processes thought responsible for driving the system towards equilibrium during the hadronic phase occur on time scales much longer than what is thought available during the hadronic phase. Thus, in [101] it is concluded that the chemical equilibrium measured in the collision can only have been achieved in the partonic phase and thus provides evidence for a deconfined state existing early in the system's evolution. However, in references [109, 110] it is speculated that the relative particle yields seen in heavy ion collisions are a direct result of the (as yet) unknown hadronization process, and as such are unrelated to any thermalization process. A thermodynamical analysis [102] of particle yields created in both nucleon-nucleon and elementary particle collisions yields temperatures and chemical potentials which follow the trend seen in heavy ion collisions. This is a somewhat surprising result considering these colliding systems are much smaller than the corresponding nuclear systems, and thus the particles created during a nucleon-nucleon collision are not expected to experience any significant rescattering after their formation. It is not yet possible to distinguish between the two different mechanisms for achieving this apparent equilibrium and it remains an open question as to what mechanism is responsible in heavy ion collisions.

Understanding the measured ratios in the context of previous measurements made in nucleon-nucleon collisions is useful as it provides a baseline comparison to measurements made in the absence of any nuclear effects, like the creation of a QGP. The

Antibaryon-to-Baryon ratio $\frac{\bar{p}}{p}$ (Figure 5.10) and the charged meson ratio $\frac{K^-}{K^+}$ (Figure 5.11) as presented in this work are seen to follow the trend followed by previous measurements made at lower values of $\sqrt{s_{NN}}$ by nucleon-nucleon as well as nuclear collisions. The transverse momentum dependence of the measured ratios presented in this thesis are consistent with a constant value. This can be compared to what is expected from nucleon-nucleon collisions, where the ratio is seen to drop at sufficiently high values of $p_\perp$. In [65], pQCD calculations predict this behavior which is understood to arise from quark-quark scattering dominating the collision dynamics at sufficiently high values of $p_\perp$. However, the same pQCD calculations show a strong $\sqrt{s}$ dependence for the various scattering terms (quark-quark, gluon-quark, and gluon-gluon) contributing to the calculated particle ratios. These pQCD calculations predict gluon-gluon scattering to dominate the collision for the center of mass energies achieved at the RHIC collider. This dominance of the partonic scattering by gluons is expected to extend from low values of $p_\perp$ up to $p_\perp$ values $\sim$6 GeV/c, at which point scattering involving quarks becomes important. Indeed, the charged particle ratios measured at ISR were seen to approximately scale with x_T. The ratios presented in this work are flat and based on the approximate x_T scaling are expected to remain flat up to rather high values of $p_\perp$. This is an indication that gluon scattering dominates the particle production out to high $p_\perp$, with a lower limit as high as 2.5 GeV/c.

Future Directions

The first year of RHIC data collected by the STAR experiment enabled measurements to be made of the charged particle ratios out to 2.5 GeV/c using the RICH detector in conjunction with the STAR TPC. Opportunities exist to extend these measurements out to a momentum of 5 GeV/c (for the Antiproton-to-Proton ratio) by analyzing the higher statistics data collected during the second year of RHIC running. While no definitive evidence exists, as of yet, for the much sought after quark-gluon plasma phase transition, extending the Antiproton-to-Proton ratio measurement out to 5 GeV/c will enable a stronger discrimination to be made between the various model predictions of the Antiproton-to-Proton ratio. However, measurements of the Antiproton-to-Proton ratio conducted at lower collision energies suggest deviations from the flat behavior of the Antiproton-to-Proton ratio at low momenta should be expected only at relatively high $p_{\perp}$ ($\sim$ 6 GeV/c at a center of mass energy of $\sqrt{s_{NN}} = 130$ GeV/c). Future experiments will necessarily have to account for this by extending particle identification capabilities beyond a transverse momentum of 5 GeV/c. RICH detectors of the type described in this thesis employed in future experiments will therefore have to be enhanced to provide the necessary particle identification beyond 5 GeV/c. This can be most readily accomplished by substituting a radiator material having an index of refraction which is lower than the current radiator's index of refraction of $\sim$ 1.3. However, this is not expected to be a simple task and will require significant work to accomplish this enhancement in the particle identification capabilities of the detector.

Bibliography

[1] B. Lasiuk. *NIM (in press)*, 2002.

[2] F. Piuz et al. *NIM*, A(433):178–189, 1999.

[3] Jon Gans. *Yale Note 32*, 2000.

[4] http://r.home.cern.ch/r/richrd26/www/hmpid.

[5] M.A. Lisa. *STAR note 0238*, 1996.

[6] Ullrich Lasiuk. *Star C++ Class Library: User Guide and Reference Manual*, 1999.

[7] Manuel Caldern de la Barca Snchez. *Charged Hadron Spectra in Au+Au Collisions at sqrt(sNN) = 130 GeV.* PhD thesis, Yale University, September 2001.

[8] Reya Glück and Vogt. Dynamical parton distributions revisited. *hep-ph/9806404*, 1998.

[9] Durham Database Group Durham University(UK). Parton distributions: Online plotting. http://cpt19.dur.ac.uk/hepdata/pdf3.html.

[10] D Magestro. Pres. at: 6th international conference on strange quarks in matter: A flavorspace odyssey, franfurt am main, germany. *hep-ph/0112178*, Sept. 25-29 2001.

[11] T.D. Lee. *Rev. Mod. Phys.*, 47(2):2291, 1975.

[12] Frithjof Karsch. *Nucl. Phys.*, A(698):199–208, 2002.

[13] J. Schaffner-Bielch M.H. Thoma K. Schertler, C. Greiner. *Nuclear Physics*, A(677):463–490, 2000.

[14] P.V. Landshoff K. Kajantie and J. Lindfors. *Phys. Rev. Lett.*, 59:2527, 1987.

[15] K. Kajantie K.J. Eskola and J. Lindfors. *Nucl. Phys.*, B(323):37, 1989.

[16] G. Calucci and D. Treleani. *Phys. Rev.*, D(41):3367, 1990.

[17] G. Calucci and D. Treleani. *Phys. Rev.*, D(44):2746, 1991.

[18] RHIC Project. Rhic design manual. *Technical Design Report, Brookhaven National Laboratory*, URL: http://www.agsrhichome.bnl.gov/NT-share/rhicdm/, 1994.

[19] J.W.Harris and B. Muller. *Ann.Rev.Nucl.Part.Sci*, (46):71–107, 1996.

[20] *Quark Matter proceedings*, 1996-2001.

[21] Commisioning of the relativistic heavy ion collider. *Proceedings of the 2001 Particle Accelerator Conference, Chicago*, 2001.

[22] C et al Adler. *NIM*, A(461):337–340, 2001.

[23] R.L. Brown et al. *Proc. IEEE 1997 Particle Accelerator Conference*, 3230, 1998.

[24] Howard Wieman. *STAR note* #14, 1991.

[25] Howard Wieman. *STAR note* #253, 1996.

[26] P. Nevski. Geant description of star experiment. http://www.star.bnl.gov/STAR/comp/simu/gstar/GEOM/btof/btomat.html.

[27] STAR-RICH collaboration. Proposal for a ring imaging cherenkov detector in star. *YRHI 98-022*.

[28] Séguinot et al. *NIM*, A(371):64–78, 1996.

[29] Breskin et al. *NIM*, A(371):116–136, 1996.

[30] P. Križan et al. *NIM*, A(371):151–154, 1996.

[31] Ratcliff. *NIM*, A(371):309–320, 1996.

[32] F. Piuz et al. *NIM*, A(371):96–115, 1996.

[33] Di Mauro et al. *NIM*, A(371):137–142, 1996.

[34] Di Mauro et al. *NIM no.1-3*, A(461), 2001.

[35] Di Mauro et al. *NIM*, A(371):275–284, 1996.

[36] Puiz et al. *ALICE/PUB-99-11*, 1999.

[37] Puiz et al. *ALICE/PUB-99-07*, 1999.

[38] Puiz et al. *ALICE/PUB-99-08*, 1999.

[39] Alkhazov. *NIM*, (89):155–165, 1970.

[40] Iwona M. Sakrejda Jeffery Mitchell. Tracking for the star tpc documentation and user's guide. *STAR note SN0190*, 1995.

[41] R. et. al. Bossingham. Star offline simulations and analysis software design. *STAR note 0281*, 1997.

[42] D. Cebra and S. Margetis. Technical report. *STAR note SN089, Main Vertex reconstruction in STAR (unpublished).*

[43] A. Drees and Z. Xu. Luminosity scans at rhic during the year 2000 run. *Technical Report No. C-A/AP/43, BNL, (unpublished)*, 2001.

[44] C; White-S N Baltz, A J; Chasman. *Nucl. Instrum. Methods Phys. Res., A*, 417, 1998.

[45] Lange et al. *NIM*, A(453):397–404, 2000.

[46] R. Brun et al. *http://root.cern.ch.*

[47] B.B. Back et Al. *Phys. Rev. Lett*, 87:102301, 2001.

[48] PHENIX collaboration. *nucl-ex/0112006; submitted to Phys. Rev.*

[49] PHENIX collaboration. *Phys. Rev. Lett.*, 86(16):3500–3505, 2001.

[50] Kaneta. Chemical fit at rhic. *Talk given at ThermFest*, 2001.

[51] STAR collaboration. Strange anti-particle to particle ratios at mid-rapidity in $\sqrt{s_{NN}} = 130$ gev au+au collisions. (to be published). 2002.

[52] Videbaek for the BRAHMS Collaboration. *Nuclear Physics*, A(698):29c–38c, 2002.

[53] C. Adler et al. STAR Collaboration. *Phys. Rev. Lett.*, (86):4778, 2001.

[54] D.E. Groom et al. (Particle Data Group). *Eur. Phys. J.*, C(15), 2000.

[55] I.G. Bearden et Al. *Phys. Rev. Lett*, (11):112305, 2001.

[56] Basile et al. *IL NUOVO CIMENTO*, 66A(2):129–163, 1981.

[57] Glenn Elliot Cooper. *Baryon Stopping and Hadronic Spectra in Pb-Pb Collisions at 158 GeV/nucleon.* PhD thesis, University of Californai, Berkeley, April 2000.

[58] Stephen Vance. PhD thesis, Columbia University.

[59] L. Camilleri. *Phys. Rep.*, 144(2):53–114, 1987.

[60] Alper et al. *To appear in the proceedings of 17th Winter Workshop on Nuclear Dynamics, Park City, Utah, 10-17 Mar 2001*, 2001.

[61] Alper et al. *Nucl. Phys.*, B(100):237–290, 1975.

[62] Alper et al. *Nucl. Phys.*, B(87):19–40, 1975.

[63] Antreasyan et al. *Phys. Rev. Lett.*, 38(3):112–114, 1977.

[64] Antreasyan et al. *Phys. Rev. Lett.*, 38(3):115–117, 1977.

[65] J.F. Owens and E. Reya. *Phys. Rev.*, D18(5):1501–1514, 1978.

[66] W.R. Chen and R.C. Hwa. *Phys. Rev.*, D(39):179, 1989.

[67] X.N. Wang. *Phys. Rev.*, D(43):104, 1991.

[68] X.N. Wang and Shi yuan Li. *pre-print*, nucl-th/0110075, 2001.

[69] Lenkeit et al. *Nucl. Phys. A*, 661:23–32, 1999.

[70] J.D. Bjorken. *Fermilab-Pub-82/59-THY (unpublished)*, 1982.

[71] M. Thoma M. Gyulassy, M. Plumer and X.N. Wang. *Nucl. Phys. A*, 538:37, 1992.

[72] M. Gyulassy M. Thoma. *Nucl. Phys. B*, 351:491–506, 1991.

[73] David A. Appel. *Phys. Rev. D*, 33(3):717, 1986.

[74] J.P. Blaizot and L. McLerran. *Phys. Rev. D*, 34(9):2739, 1986.

[75] P. Bagnaia et al. *Phys. Lett. B*, 144:283, 1984.

[76] M. Greco. *Z. Phys. C*, 26:567, 1985.

[77] Manfred Rammerstorfer and Ulrich Heinz. *Phys. Rev. D*, 41(1):306, 1990.

[78] J.K. Gunion and G. Bertsch. *Phys. Rev. D*, 25:746, 1982.

[79] M. Gyulassy and M. Plumer. *Phys. Lett. B*, 243(4):432–438, 1990.

[80] I. Vitev M. Gyulassy, P. Levai. *Nucl. Phys. A*, 661:637, 1999.

[81] I. Vitev M. Gyulassy, P. Levai. *Nucl. Phys. B*, 571:197, 1999.

[82] I. Vitev M. Gyulassy, P. Levai. *Phys. Rev. Lett.*, 85:5535, 2000.

[83] P. Levai M. Gyulassy. *Phys. Lett B*, 442:1, 1998.

[84] P. Levai M. Gyulassy and I. Vitev. *Nucl. Phys. B*, 594:594, 2001.

[85] A.H. Mueller R. Baier, Yu.L. Dokshitzer and D. Schiff. *Nucl. Phys. B*, 483:291, 1997.

[86] A.H. Mueller R. Baier, Yu.L. Dokshitzer and D. Schiff. *Nucl. Phys. B*, 531:403, 1998.

[87] A.H. Mueller S. Peigne R. Baier, Yu.L. Dokshitzer and D. Schiff. *Nucl. Phys. B*, 478:577, 1996.

[88] A.H. Mueller S. Peigne R. Baier, Yu.L. Dokshitzer and D. Schiff. *Nucl. Phys. B*, 484:265, 1997.

[89] Ivan Vitev and M. Gyulassy. *pre-print*, nucl-th/0104066, 2001.

[90] X.N. Wang. *Phys. Rev. C*, 58(4):2321, 1998.

[91] X.N. Wang. *Phys. Rev. Lett.*, 81(13):2655, 1998.

[92] X.N. Wang and M. Gyulassy. *Phys. Rev. D*, 44:3501, 1991.

[93] X.N. Wang and M. Gyulassy. *Phys. Rev. Lett*, 68(10):1480, 1992.

[94] M. Gyulassy X.N. Wang and M. Plumer. *Phys. Rev. D*, 51(7):3436, 1998.

[95] A.M. Snigirev I.P. Lokhtin. *Phys. Lett. B*, 440:163.

[96] S. Peigné R. Baier, Yu.L. Dokshitzer and D. Schiff. *Physics Letters*, B(345):277.

[97] Xin-Wang Wang and Zheng Huang. *Phys. Rev. C*, 55(6):3047.

[98] Miklos Gyulassy and Peter Levai. *Phys. Lett. B*, (442):1–6, 1998.

[99] G.Papp G.Fai G.G.Barnafoldi I.Vitev Y.Zhang P.Levai, M.Gyulassy. *Nucl. Phys.*, A(698):631–634, 2002.

[100] Vogt Gluck, Reya. *Z. Phys. C*, (67):433, 1995.

[101] Redlich Stachel Braun-Munzinger, Magestro. *hep-ph/0105229*, 2001.

[102] F. Becattini. *Zeitscrift Für Physik*, C(69):485–492, 1996.

[103] C. Dover P. Koch. *Phys. Rev. C*, (40):145, 1989.

[104] Owens Duke. *Phys. Rev. D*, (30):49, 1984.

[105] M.Gyulassy. private communication. 2002.

[106] Braun-Munzinger et al. *Phys. Lett. B*, (465):15, 1999.

[107] Becattini et al. *Phys. Rev. C*, (64):024901, 2001.

[108] Kabana and Minkowski. *New J. Phys.*, (3):4, 2001.

[109] R. Stock. *Physics Letters*, B(456):277–282, 1999.

[110] U. Heinz. *Nuclear Physics*, A(661):140c–149c, 1999.